AN INVESTIGATION OF NANODOSIMETRIC PARAMETERS FOR REALISTIC GEOMETRIES AND A NOVEL STUDY OF THE TRACK STRUCTURE PENUMBRA REGION

Sonwabile Ngcezu

A thesis submitted to the Faculty of Science, University of the Witwatersrand, Johannesburg, in fulfilment of the requirements for the degree of Doctor of Philosophy

Johannesburg, 2021

DECLARATION STATEMENT

I Sonwabile Ngcezu declare that this thesis is my own, unaided work. It is being submitted for the degree of Doctor of Philosophy at the University of the Witwatersrand, Johannesburg. It has not been submitted before for any degree or examination in any other University.

_____

(Signature of candidate)

19th day of April 2021 in Pretoria

DEDICATION

Unkosikazi, Thembi Ngcezu
Umonde, nokuqonda, nenkxaso ondiphe yona, ayinakuthelekiswa nanto.

Mama, Vuyelwa Ngcezu
Usisikhuthazo nentsika ebomini bam

Abantwana bam, Inathi Asikelwelwe Zimkhitha Malaika (Pun), Sibabalwe Tabita Azania, and nabaseza
Ndiyanithanda, kwanga imisebenzi yezandla zam ingayinkuthazo nomzekelo ebomini benu

kuTata owasishiyayo
Jwarha, Izandla zakho ziphila kwezi zam.

Abantakwethu
Ningumthombo wovuyo, kunye nokuphumla

PRESENTATIONS ARISING FROM THIS STUDY

Below is a list of presentations arising from this work.

1. Sonwabile Arthur Ngcezu, Hans Rabus, Marion Bug, and Debbie van der Merwe. Electric field effects on the ionization cluster size distribution (ICSD) using the GEANT4 Monte Carlo toolkit. 28th IUPAP Conference on Computational Physics, 11 July 2016.
2. Sonwabile Arthur Ngcezu, Hans Rabus, Marion Bug, and Debbie van der Merwe. Nanodosimetric characterization of protons in the Bragg peak region. NEUDOS-13, Krakow, 14-19 May 2017.
3. Sonwabile Arthur Ngcezu, Hans Rabus, Marion Bug, and Debbie van der Merwe. Enhancement of the biological effectiveness in the Bragg peak: a nanodosimetric perspective. ICARO-2, International Atomic Energy Agency, Austria Vienna, 20-24 June 2017.
4. Sonwabile Arthur Ngcezu, Hans Rabus, Marion Bug, and Debbie van der Merwe. Investigating nanodosimetric parameters in and around charged particles. South African Association of physicist in Medicine and Biology. South Africa, Durban, 25-27 September 2017.
5. Sonwabile Arthur Ngcezu, Hans Rabus, Marion Bug, and Debbie van der Merwe. Investigating nanodosimetric parameters in and around charged particles. 17th International symposium on microdosimetry, Italy, Venice 5-10 November 2017.
6. Sonwabile Arthur Ngcezu, Hans Rabus, Heidi Nettelbeck. Nanodosimetric analysis of proton tracks in a spread-out Bragg peak. IDOS 2019, International Atomic Energy Agency, Austria Vienna, 18-21 June 2019

PUBLICATIONS ARISING FROM THIS STUDY

Below is a list of publications arising from work done in the current study. Journal articles by the candidate during the course of the degree programme

1. Ngcezu, S. A., Rabus, H., Bug, M. & Merwe, D., 2017. Investigating nanodosimetric parameters in and around charged particle tracks. Physica Medica, 9, Volume 41, Supplement 1, p. S7
2. Hans Rabus, Gerhard Hilgers, Sonwabile Arthur Ngcezu, Marion Bug, Considerations on the target size in a wall-less nanodosimeter, *Radiation Protection Dosimetry*, Volume 183, Issue 1-2, May 2019, Pages 182–186.
3. Rabus, H., Ngcezu, S. A., Braunroth, T. & Nettelbeck, H., 2020. "Broadscale" nanodosimetry: Nanodosimetric track structure quantities increase at the distal edge of spread-out proton Bragg peaks. Radiation Physics and Chemistry, 1, Volume 166, p. 108515.
4. Braunroth, T., Nettelbeck, H., Ngcezu, S.A. and Rabus, H., 2020. Three-dimensional nanodosimetric characterization of proton track structure. *Radiation Physics and Chemistry*, Volume 176, p.109066.
5. Ngcezu, S. A., Rabus, H., Nanodosimetric track analysis in a spread-Out Bragg Peak. Standards, Applications and Quality Assurance in Medical Radiation Dosimetry (IDOS), Book of Extended Synopses, International Atomic Energy Agency, Vienna, IAEA-CN-273, 256-257 (2019).

Publication 2 contains materials and methods that form Section 3.3 of this thesis and part of the results shown and discussed in Section 4.5.

Publication 3 contains materials and methods that form Section 3.1 of this thesis and part of the results shown and discussed in Section 4.2.

Publication 4 contains materials and methods that form Section 3.2 of this thesis and part of the results that are shown and discussed in Section 4.3.

ABSTRACT

Relative Biological Effectiveness (RBE) used in radiotherapy can be derived from the study of nanodosimetric parameters of particle track structure (TS). In nanodosimetry, the ionization component of charged particle TS is characterized by the measurement or calculation of the frequency distribution of ionizations in target volumes that are used to simulate nanometric sites in liquid water. In the current study, Monte Carlo simulation tools and software analysis techniques are employed in the mapping of nanodosimetric parameters radially from and along proton tracks.

Two approaches were used to study the radial dependence of nanodosimetric quantities around protons tracks. A heuristic approach was ultimately used to evaluate changes along the track pathlength, and secondly, a more accurate approach was used to provide a detailed analysis of both the core and penumbra regions. For the first approach, a nanodosimetric TS analysis attempt is presented to address the issue of RBE variation in a Spread-Out Bragg Peak (SOBP) of protons. The Geant4-DNA simulation package is used for the simulation and capture of the ionization component of protons of 100 MeV initial energy and their secondary electrons propagating in water. The frequency distribution of ionization clusters formed in target volumes corresponding to a 10 base-pairs segment of Deoxyribonucleic Acid (DNA) was obtained as a function of the radial distance between target and proton trajectory for a set of positions along the proton path. The radial dependence of nanodosimetric parameters was analyzed using a heuristic model function to obtain an Effective Track Cross-Section (ETCS) derived from the integration of the model as a function of the proton's residual range. The results were convolved with weighted range distributions suggested in the literature for the construction of the SOBP. In the second approach, a more detailed investigation into the nanodosimetric properties of the track structure of protons in water at energies relevant for proton radiotherapy follows from the heuristic study above. The ionization component of the tracks is still simulated using Geant4-DNA for proton start energies between 1 MeV and 100 MeV. From the simulation results, the frequency distribution of ionization clusters formed in nanometric target volumes was obtained dependent on the impact parameter of the proton trajectory

with respect to the target centre. In the track core, targets of cylindrical shape and a size comparable to a short segment of DNA were used for scoring ionization cluster size distributions. For the penumbra region, three different options for defining the cylinder shell segments were investigated, with each cylinder shell segment volume the same as the cylinder target volume. The radial distributions were numerically integrated to obtain the effective track cross-sections with respect to different nanodosimetric parameters. Graphically displaying the radial dependence in a similar way as microdosimetric distributions allowed elucidating the contribution of different radial distances to the overall radial integral of the quantities under consideration. Furthermore, it was tested how well the radial dependence of the nanodosimetric parameters could be fitted with a model function derived in literature for the radial energy deposition in proton tracks.

The calculated ionization cluster size distribution from charged particle radiation tracks depend heavily on the size, geometry, and material of the target volume. The geometry of the target, specifically its orientation relative to the direction of the primary track, is investigated in this study. Simulations performed in the first approach are used to investigate the dependence of nanodosimetric parameters on target orientation.

A related investigation involved the ion counter nanodosimeter at the Physikalisch Technische Bundesanstalt (PTB), where both the electrical field and the extraction aperture define the size and shape of the sensitive volume. In this study, a procedure to determine a cylindrical effective measurement target that is based on the second moments of the detection efficiency map is presented. The efficiency map is represented by an analytical model used in the investigation of the dependence of the simulated site size on the nanodosimeter's operating parameters.

The ETCS derived from the heuristic model shows an increase in the distal end region of the SOBP in qualitative agreement with radiobiological observations of enhanced cell damage in this region. The results demonstrate that nanodosimetric track characteristics may be used for qualitatively predicting the variation of the probability for induction of lethal lesions in cells.

In the second approach, it was found that the model function from literature allows describing only the radial dependence of the total frequency of nanometric targets where ionizations occur. The deviation from a $1/r^2$ dependence of the radial dependence of the frequency of targets receiving more than a minimum number of ionizations (exceeding one) includes a second peak centred around 10 nm radial distance from the proton trajectory. Calculated nanodosimetric parameters are found to have some dependence on the orientation of the target. With respect to the investigation for the derivation of the wall-less target in a nanodosimeter, the results show that within the limits of the simplifying assumptions, the model of an effective cylindrical target gives a reasonable approximation of the efficiency map.

ACKNOWLEDGEMENTS

A special appreciation to Professor Debbie van der Merwe for giving me a chance and for her unconditional support in this journey. This work has taken longer than anticipated, but from the first email I sent you requesting supervision to the last motivations we wrote to complete the work, you have been superb.

This work would never have been possible without the tireless support, transfer of knowledge and selfless help from Dr Hans Rabus, Dr Marion Bug, Dr Johannes Rahm, Dr Gerhard Hilgers, Dr Heidi Nettelbeck, Thomas Braunroth and including all the individuals who spent a lot of time assisting and mostly contributing to this work. Dr Rabus, the opportunity you gave me and the effort you put into this work are invaluable. I will never forget the times you have had to be rightfully tough with me, and your refreshing honesty throughout this study is something to emulate. Dr Bug, I often think about your contribution to this work and your assistance when I was just starting up in nanodosimetry. The discussions we've had on this subject, I never will forget.

I would be amiss not to mention my friends for their support and at times, guidance in my studies. Thulani Nyathi, the quality of time you spend with some friends, however briefly, can be of significant influence in a person's life. To all the friends who had shown interest through the years, I say thank you.

Finally, a special thanks to the National Metrology Institute of South Africa (NMISA) for sponsoring numerous visits to PTB during my study. The sponsorship of the visits by the PTB via the Technical Cooperation Project: "Upgrading of quality infrastructure in Africa" is much appreciated. Support from the PTB and the University of the Witwatersrand is gratefully acknowledged.

TABLE OF CONTENTS

NOMENCLATURE/LIST OF ABBREVIATIONS AND SYMBOLS

Area Integral of Specific Energy by Ionisations	**AISEI**
Bragg Peak	**BP**
Computed Tomography	**CT**
Conformal Radiotherapy	**CRT**
Continuous Slowing down Approximation	**CSDA**
Deoxyribonucleic Acid	**DNA**
Effective Track Cross-Section	**ETCS**
Intensity Modulated Radiotherapy	**IMRT**
International Atomic Energy Agency	**IAEA**
International Commission on Radiation Units and Measurements	**ICRU**
Ionisation Cluster Size	**ICS**
Ionisation Cluster Size Distribution	**ICSD**
Linear Energy Transfer	**LET**
Local Effect Model	**LEM**
Micro-Kinetic Model	**MKM**
National Metrology Institute of South Africa	**NMISA**
Normal Tissue Complication Probability	**NTCP**
Physikalisch Technische Bundesanstalt	**PTB**
Pristine Bragg Peak	**PBP**
Spread-Out Bragg Peak	**SOBP**
Relative Biological Effectiveness	**RBE**
Resonance Imaging	**MRI**
Region Of Interest	**ROI**
Track Structure	**TS**
Tumour Control Probability	**TCP**
Ultraviolet	**UV**

LIST OF TABLES

LIST OF FIGURES

CHAPTER 1: INTRODUCTION

The interaction of ionising radiation with animate biological matter, specifically, with the human cell nucleus results in genomic instabilities, DNA damage, mutation, and ultimately cell death (Nikjoo, Uehara and Emfietzoglou, 2012). As such, for animate matter, radiation can be used to eradicate cancerous cells. The killing of cancerous cells involves the physical action of radiation occurring through the deposition of energy to this medium via the ionisation and excitation of its atomic constituents. A spatial distribution of interaction points, called the radiation track, is left behind by these physical events. Radiation tracks come in many types - depending on the particle type and its energy – long and short interaction range, thin and broad lateral spread, and sparse or dense ionisation density. The irradiated medium's biological effects heavily depend on the type of track (e.g. the ionisation density of the tracks is a factor in determining the complexity of DNA damage). This work is concerned with the nanodosimetric characterization of proton tracks at therapeutic radiation qualities used in cancer treatment.

Modern cancer management employs invasive surgery, radiation therapy and chemotherapy as standards for treatment. Alternative modalities for cancer treatment are available but are not used frequently. Examples of these modalities include immunotherapy, targeted therapy, hormone therapy, stem cell transplant etc. (Abbas and Rehman, 2018). However, by and large, the three aforementioned fields of medicine are still the hallmark of modern cancer management (Boyle and Levin, 2008). However, at least for the foreseeable future, radiation therapy will remain an essential modality in cancer treatment because it is a non-invasive, cost-effective and indiscriminate killing force that can be focused and enhanced with pharmacological agents (Bernier, Hall and Giaccia, 2004; Baskar *et al.*, 2012).

Cancer incidence and deaths are projected to increase. For instance, global cancer deaths were about 7.6 million in 2008, and this number is expected to rise to a staggering 12.9 million by 2030 under the hypothesis of no increase in cancer incidence and cancer death rates (Boyle and Levin, 2008). Significant improvements in the efficacy of radiation therapy, in particular, were sometimes

associated with considerable progress in technology (Lee *et al.*, 2014; Chetty *et al.*, 2015; Beaton *et al.*, 2019; Mohan *et al.*, 2019; Fiorino *et al.*, 2020). To this end, through technological advancement, radiation therapy has been revolutionised by the introduction of Computed Tomography (CT, the early 1970s), Magnetic Resonance Imaging (MRI, late 1970s), Conformal Radiotherapy (CRT), IMRT (early 1980s) and the increasing use of hadron therapy (developed since 1946). These have led to conformal radiotherapy, shaped to the contours of the tumour with a high dose fall-off to preserve critical structures, which has significantly improved local control rates, even for patients with locally advanced tumours (Bernier, Hall and Giaccia, 2004). These advances in the practice of radiotherapy are not without intense controversy, especially when considering the legitimate field of evidence-based medicine/radiotherapy (Hoffmann, Bennett and Del Mar, 2013) in conjunction with the evaluation of the cost to benefit ratios which are not to be underestimated, more especially in low and middle-income countries (PTCOG, 2019).

Recent efforts in finding effective/optimum cancer treatments have seen the increased use of treatment with light to heavy nuclei called hadron therapy. Hadron therapy is an innovative radiotherapy modality based on nuclear particles (protons, neutrons, light/heavy ions, etc.) to treat tumours. In South Africa, hadron therapy treatments at the iThemba LABS started in 1988 for neutron therapy and 1993 for protons. Patients with numerous cancers diagnosis (e.g. salivary gland carcinoma, eye and obit tumours, arteriovenous malformation etc.) have been treated in this facility. There has been a dramatic increase in the use of nuclear projectiles, mainly in high-income countries, for the management of cancer in radiotherapy. From its inception in 1954 until 2018, 221.528 patients have been treated with hadron therapy (PTCOG, 2019). As of early 2014, the particle therapy co-operative group has reported that there is an exponential increase in hadron therapy centres, especially in high-income countries in the first world (PTCOG, 2019). The rise in hadron radiotherapy calls for intensified research into this field.

The primary motivation in using heavy charged particles in radiotherapy is their unique physical and biological properties. Hadron therapy offers unique physical

characteristics (ballistic accuracy) of energy deposition and biological phenomena (especially heavy ions) resulting from the high density of energy deposition (*Relative Biological Effectiveness in Ion Beam Therapy*, 2008). Contrasting the physical and biological characteristics of conventional photon and electron radiotherapy modalities to those of hadron therapies highlights a fundamental link between physics and radiobiology. A concerted effort against cancer by researchers around the world is focusing on groundbreaking developments in the interface area between physics and radiobiology. Accelerator facilities have been focusing on fundamental research in new delivery systems and dosimetry innovations. Thus, intense multidisciplinary research collaborations (e.g. medical physicists, radiation scientists, radiobiologists, clinicians, engineers, IT experts etc.) in the development of novel methods, numerical techniques and instruments will have a significant impact in redefining the landscape of cancer management. One such field of research, which is the general topic of this thesis, concerns the study of the physical characteristics of hadron radiation (and ultimately ionising radiation in general) and how they relate to the radiobiological phenomena induced in living tissue. This field of research is paramount to the extension of current knowledge in combating cancer with radiotherapy because the focus is not just the assessment of the physical dose but a thorough investigation of the related radiobiology.

With regards to the assessment of treatment plans, the radiotherapy community realises the need to move beyond physical dose distributions - assumed to correlate with the biological response - to optimisation based on estimates of the biological outcome itself. These biological endpoints are realised by using models that calculate the Tumour Control Probability (TCP) and the Normal Tissue Complication Probability (NTCP), which are used to evaluate and compare radiotherapy treatment plans (Nahum and Uzan, 2012). The biological models are an attempt to accurately quantify clinical outcomes by including several radiobiological factors that contribute to the effectiveness or non-effectiveness of radiation to treat cancer. These factors include absorbed dose, fractionation, dose rate, radiation quality and biological systems (*Relative Biological Effectiveness in Ion Beam Therapy*, 2008). Out of these factors, radiation quality is an object of intense research all over the world and is the subject of the current study. Unless

otherwise specified, reference to RBE as it pertains to the current work exclusively refers to those parameters related to radiation quality which is but one component in the general concept of RBE. Radiation quality is related to the type of particles and their energy spectrum. In the past few decades, researchers in the fields of radiation dosimetry and radiobiology extended the understanding of radiation quality to the study of stochastics of energy deposition distribution. It focused on the probabilistic non-uniformities in space and time of radiation interactions with tissue at micro- and ultimately nanometer length scales of DNA (Goodhead, 2006). The ultimate goal is to derive models that incorporate those biological characteristics of any track related to radiation quality to radiobiological models of NTCP and TCP used in the assessment of treatment plans.

The track structure was initially studied in the field of microdosimetry (Rossi, 1960; Rossi and Zaider, 1996; Cruz and Santa Cruz, 2016) for target sizes on the order of cellular dimensions (i.e. on the micrometre scale). The field of nanodosimetry is concerned with characterising the ionisation component of ionising particle track structure by considering the formation of ionisation clusters in nanometer-sized target volumes (Rabus, 2020). This track structure, i.e. which is the spatial and temporal pattern of interactions, is related to the biological effectiveness of ionising radiation. The quantity of interest is the single-event frequency distribution of the ionisation cluster size distribution (ICSD), i.e. the frequency distribution of the number of ionisations in specified target volumes (sites). Since the biologically relevant radiation-sensitive target is said to be short sections of the DNA molecule or larger units of DNA like the histone (Goodhead, 2006), nanodosimetry considers site sizes of the order of a few nanometers in liquid water, and the geometry of these sites is often chosen as cylindrical volumes (Grosswendt, 2004).

Numerous computational investigations of particle track structure have indicated that inelastic interactions in the DNA molecule and its surrounding play a key role in the initiation of radiation-induced damage (Cox *et al.*, 1977; Goodhead and Thacker, 1977; Goodhead *et al.*, 1977; Nikjoo and Goodhead, 1991; Brenner and Ward, 1992; Nikjoo *et al.*, 1999). The relevance of nanometric target sizes was derived from the pronounced maximum in the RBE that occurs for most biological

endpoints at a Linear Energy Transfer (LET) of 100 keV/μm (Goodhead, 1994), which corresponds to a mean free path for ionisation by charged particles (in water) of about 2 nm. This dimension coincides with the diameter of the double helix structure of the DNA molecule. The DNA molecule is, therefore, often considered the most critical target for biological radiation effects (Goodhead, 2006). Therefore, dosimetric studies at the DNA scale would provide invaluable insight into the action of ionising radiation to living tissue.

The potential of ionising radiation to produce clustered DNA damage stems from a detailed investigation of the physical track structure of the radiation. New dosimetric parameters for characterising the track structure of radiation have been derived. These parameters are calculated from the ICSD within a specified volume. Nanodosimetry conceptually allows a transparent separation of the physical processes (dependent on modality) from the biological ones (independent of the modality). This should allow for better comparisons and evaluations of clinical results using different particles, which, in turn, would result in optimised treatment planning through a better understanding and choice of radiation qualities (Palmans *et al.*, 2015).

Radiation beams of different radiation quality exhibit significant differences in the complexity of clustered damage and hence have different biological effectiveness. The relative biological effectiveness of light to heavy charged particles compared to photons and electrons depends on several other parameters, and it increases with depth in the patient because of the slowing down of the particles, which increases the ionisation density (thus, the higher probability of multiple ionisations in a single DNA molecule), hence a rise in RBE. A joint document by the International Atomic Energy Agency (IAEA) and International Commission on Radiation Units and Measurements (ICRU) entitled "Relative biological effectiveness in ion beam therapy" (Relative Biological Effectiveness in Ion Beam Therapy, 2008) has expressed concern about a diversity of methods being used in radiotherapy to derive RBE and biological weighting factors in general, which vary for different modalities and are applied "in an often inconsistent manner leading to confusion in interpretation and possible risk to patients". The collaborative group proposed,

therefore, that there should be a "universally agreed approach for the use of weighting factors … (to) … facilitate the exchange of information and improve collaboration between centres and within the radiotherapy community" (Relative Biological Effectiveness in Ion Beam Therapy, 2008). Modern DNA damage and repair measurement techniques provide insight into molecular damage induced by fast ions. These studies show that high LET radiations induce a high fraction of clustered DNA damage challenging to repair compared to low LET radiations. From the discourse, it is evident that for a biological object (micro/nanometric in size), "all the differences in the biological action of charged particle beams should then be attributed to the unique special energy deposition pattern of charged particles compared to photon irradiation, i.e. Track structure" (Relative Biological Effectiveness in Ion Beam Therapy, 2008).

Protons are used in cancer therapy for treatment scenarios where their radio-physical property of completely stopping in the irradiated cancer tissue is exploited to avoid dosage of distal critical organs (Newhauser and Zhang, 2015). The region of maximum energy deposition, which is referred to as the Bragg peak (BP), can also correspond to an increase in RBE (Relative Biological Effectiveness in Ion Beam Therapy, 2008). Protons are used for the treatment of specific types of cancers that are difficult to treat using surgery or conventional radiotherapy (e.g. treatment with photons and electrons). Proton therapy is advantageous over conventional radiotherapy in that the dose from protons is predominantly deposited over a short range that is well defined (Newhauser and Zhang, 2015). The ensuing spatial concentration of ionising interactions may also correspond to an increase in RBE (Relative Biological Effectiveness in Ion Beam Therapy, 2008). For protons, a constant RBE for tumour cell killing of 1.1 is used in most clinical treatment planning (Paganetti *et al.*, 2002; *Relative Biological Effectiveness in Ion Beam Therapy*, 2008; Paganetti, 2014), despite the increasing evidence for significantly larger RBE at the distal end of the BP (Matsumoto *et al.*, 2014; Anferov and Das, 2015; Tommasino and Durante, 2015; Giovannini *et al.*, 2016; Marshall *et al.*, 2016).

The basic concept of nanodosimetry as a tool for the experimental study of charged particle track structure dates back to 1975 (Pszona, 1975). Conceptional limitations encountered with extending microdosimetry to the nanometer regime (Amols, Wuu and Zaider, 1990) required a paradigm shift from measurement quantities related to imparted energy to ionisation clusters (Grosswendt *et al.*, 2004).

Discussed below is a summary of the research activities explored in this work, some of them published in peer-reviewed journals.

In the present work, a simulation approach was used to assess the variation of nanodosimetric quantities along and around the complete path of proton beams of energies up to 100 MeV. The aim of the present study is to explore track structure details at the nanometer level occurring within proton SOBPs, which could provide an explanation of such RBE enhancements at the distal end of the SOBP. In the first approach, the nanodosimetric characteristics considered were derived from the frequency distributions for ionisation cluster formation in nanometric sites (target volumes) as extracted from simulations of proton tracks. The variation of the frequency distributions with the distance between the site centres and the proton trajectory was determined and radially integrated to obtain probability-area products, which can be interpreted as an ETCS of the proton tracks with respect to nanodosimetric track structure parameters.

The approach presented above (Rabus *et al.*, 2020) is well suited to what one could call an "amorphous medium" approach. For an implementation of the approach for radiobiological modelling of radiation response, it will be necessary to consider the non-homogeneity of biological targets, where a minimum requirement would be to consider geometrical entities such as the cell nucleus or chromosome domains within it. For this purpose, the ETCSs will not be sufficient as they account for the radially integrated probabilities for a nanometric target receiving an ionisation cluster of a certain complexity in a plane perpendicular to the proton trajectory. Estimating the number of such targets with ionisation clusters inside a cell nucleus of a chromosome domain requires the knowledge of the detailed spatial variation of probabilities.

In the second approach, a more rigorous study of the radial dependence of nanodosimetric parameters done by the determination of the detailed spatial dependence of these probabilities from track structure simulation faces several challenges. The most important one is the fact that the density of ionisations in the penumbra of the track is characterised by increasing sparsity with increasing distance from the proton trajectory resulting in a small likelihood for scoring ionisation clusters in targets at fixed positions. In the first investigation above (Rabus *et al.*, 2020), a solution for this problem that ensured a complete scoring of all ionisations in an inner part of the track penumbra is presented. For the more detailed spatial dependence, the first approach (Rabus *et al.*, 2020) is refined in the second approach such that all ionisations in a certain track segment are accounted for. In addition, the information contained in the track simulation results is also more completely used by considering multiple azimuthal orientations of the targets in the inner penumbra and track core regions. (In this paper, we use the terms "track core" as a shorthand notation for radial distances of up to 5 nm from the track, "inner penumbra" for radial distances between 5 nm and 30 nm and "outer penumbra" for radial distances exceeding 30 nm.)

The trade-off for completely scoring all ionisations in the penumbra in a computationally very efficient way is that it requires the use of a target geometry that differs from the cylindrical targets commonly considered in nanodosimetry. (Complete segmentation of the penumbra by disjoint volumes could not be achieved by cylinders or spherical targets.) Even though it is expected that the influence of target size will be less significant far away from the particle trajectory, the question of equivalence of the scoring using the different targets needs to be addressed, particularly because the cylinder shell segments used are not fully convex. The requirement of identical volume to the cylindrical targets leaves different options for defining the shape of the cylinder shell segments.

Finally, detailed track simulations are always covering only a segment of the particle track where in the initial part of the volume used for recording interactions as well as in the region before its distal boundary interactions are missed that would be present in a real track. The missed interactions are due to the lack of charged

particle equilibrium as electrons produced upstream or backscattered electrons produced downstream of the considered volume are not considered in the simulations and, thus, cannot compensate for those produced inside that escape.

All these varied aspects are investigated in this study to provide a more complete assessment of nanodosimetric properties around proton tracks. This also includes details of a computationally efficient methodology for scoring nanodosimetric quantities in charged particle tracks. Furthermore, we also show a first attempt for modelling the details of the radial variation of the nanodosimetric track structure parameters (as a prerequisite for its use in radiobiological models) and particularly focus on the contribution of different radial distances to the total probability-area product.

Both nanodosimetric measurement instruments and Monte Carlo simulations are used to study ionisation cluster formation in nanometric targets of liquid water or other biological matter. The former is used to measure ICSDs in equivalent macroscopic volumes, occupied with dilute gas, simulating nanometric sites, based on a density scaling principle for the mean ionisation cluster size M1 (Grosswendt *et al.*, 2004).

Conte et al. (Conte *et al.*, 2017, 2018) recently demonstrated that the underlying assumption in nanodosimetry that ICSDs are unique functions of M1 is valid. The work is based on experiments conducted for several ion types and energies with three different nanodosimeters featuring different operating principles and conditions and simulating different site size (Bantsar *et al.*, 2018).

In this investigative work, measurement, simulations, and derivation of analytical models of the efficiency map are used as definition of the target of the nanodosimeter operated at PTB, which is unique in that it features a genuinely wall-less sensitive volume.

In Chapter 2 of this thesis, a literature review of selected dosimetric aspects of ionisation radiation from macrodosimetry, microdosimetry and its radiobiological implications, and the novel research world of nanodosimetry is covered. In section

2.1, general aspects of the scope of macrodosimetry and dosimetry in general, including its applications, are presented. The concept of dosimetry and its universal use in prescription and treatment evaluation in radiotherapy is discussed, as is the importance of accurately realising the prescribed absorbed dose in the treatment of cancer and how it relates to complication-free tumour control. The last part of this section covers macrodosimetric quantities, their definitions and use. Section 2.2 gives the history and application of microdosimetry in the current study, and the last part looks at a few microdosimetric parameters from imparted energy to specific energy and how it relates to absorbed dose. A detailed treatment of nanodosimetry is covered in sections 2.3, from its history through the current framework covering nanodosimetry principles and the current status in experimental and simulation work. In this section, a literature review of the developments in nanodosimetry of over the past two decades and a summary of the current work done by research groups in this field. Radiobiological general principles are covered in section 2.4. Section 2.5 looks at the history and current radiotherapy practice for all treatment modalities in use in a modern radiotherapy centre. The treatment using light and heavy ions in radiotherapy and all the general aspects are covered in section 2.6. An interesting section on the literature review of the use of a constant RBE variation for proton therapy in the clinic today is presented and arguments, for and against are presented. The last subsection also covers treatment planning aspects in hadron therapy.

Chapter 3 presents the materials and methods used in the study. The first section looks at the study of nanodosimetric parameters around the proton track using the heuristic approach for the radial dependence and techniques used to derive the pristine and spread-out Bragg Peak. The concept of Effective track cross-section is introduced and used to summarise the radial integrals of nanodosimetric parameters from fit parametric models. Section 3.2 gives the methods employed to extend the heuristic approach to a more detailed analysis of the core, inner and outer penumbra of a radiation track. The methods used in the studies on the variation of nanodosimetric parameters with cylinder orientation and the formalism of creating a truly wall-less target in an ion counting nanodosimeter are described in sections 3.3 and 3.4, respectively. The results and brief discussions of the investigation are

presented in Chapter 4. Chapter 5 presents the general discussion of the results and their implications. Conclusions and future work are given in Chapter 6. The Appendix (Chapter 8) section presents some of the technical aspects used in preparing and analysing simulated data. All literature references to this work are listed in Chapter 7.

CHAPTER 2: LITERATURE REVIEW

2.1 Radiation Dosimetry: A Modern Framework Of Macroscopic Dosimetry

2.1.1 Introduction

Radiation with the energy of the order of 4 eV – 25 eV is needed to cause an electron to escape an atom, resulting in the ionisation of the atom in question. This criterion does include electromagnetic radiation with wavelengths of up to 320 nm, which overlap the ultraviolet (UV) radiation band (~10 nm – 400 nm), up to very high energy ionising radiation sources. In radiation physics and dosimetry, the marginally ionising UV radiations are not considered as they are less capable of penetrating through matter (Andreo, et al., 2017). In the context of this work, the radiation physics and dosimetry framework presented is applicable to ionising radiation applications with energy ranges from 10 keV to 25 MeV for electrons and photons, neutrons up to 100 MeV, protons used in radiotherapy of energies up to 300 MeV, and heavier charged particle with a maximum energy per nucleon of about 400 MeV.

The interaction of ionising radiation with matter results in exciting or ionising the atoms and molecules of the target matter; in the process, secondary electrons might be produced that will, in turn, result in further ionisation or excitation of the medium. This happens until the primary or secondary radiation species' energy falls below some energy threshold (and the irradiated medium stops and absorbs them), below which no interaction occurs. The initial electronic transitions that produce chemically active species occur in very short times ($\leq 10^{-15}$ s) within sites traversed by the ionising particles. These represent the initial physical perturbations from which subsequent chemical and biological effects evolve. It is, therefore, appropriate to consider measurements of ionization and energy absorption as the basis for radiation dosimetry.

Radiation dosimetry is concerned with the methods to quantitatively determine the energy deposited by directly or indirectly ionising radiation in a medium while

passing through it. Radiation dosimetry plays a crucial role in radiotherapy, nuclear medicine, and radiation protection (Muhammed, 2017).

Radiation dosimetry deals with the quantitative determination, by measurement or/and calculation, of the energy absorbed after ionising radiation interacts with matter. Both charged (e.g. electrons, heavy charged particles) and uncharged (e.g. γ-rays, x-rays, and neutrons) particles used in radiotherapy today are considered to fall within the current framework. A broad treatment of radiation dosimetry deals with the determination, by measurement or calculation, of dose or dose rate from the interaction of radiation with matter, including radiologically relevant quantities such as exposure, kerma, fluence, dose equivalent, the energy imparted, specific heat energy, track structure and so on. A strict treatment of radiation dosimetry deals mainly with the absorbed dose or dose rate (Attix, 2008). In this work, we will use a broad definition that encompasses all calculation and measurement of energy imparted in tissue and its relations to the physical, chemical, and/or biological effects that result from such interaction.

Fundamentally, ionising radiation deposits energy via very many individual stochastic interactions with atoms of the target matter at nanometric scales. Depending on the application, modern dosimetric formalisms consider energy deposition at multiple scale ranges, from the nano-scale to the macro scale, as in Fig. 1 Radiation dosimetry scales and historical progress in the measurement of radiation at different length scales. The current work is concerned with dosimetry at the nano-scale, at the level of the DNA molecule. Dosimetry at the nano-scale is central to cell killing since damage to segments of the DNA behaves as a function of radiation quality (track structure). Extractyed from (Grosswendt, 2013).

Fig. 2. Of particular interest in the present work is the nano-scale, wherein the dosimetry framework has been developing for about two decades ago. The implication of the individual ranges does present unique dosimetric insights for both dosimetric measurements and calculations and presents limitations for the quantity used in the assessment and characterisation of the energy transfer, absorption, and

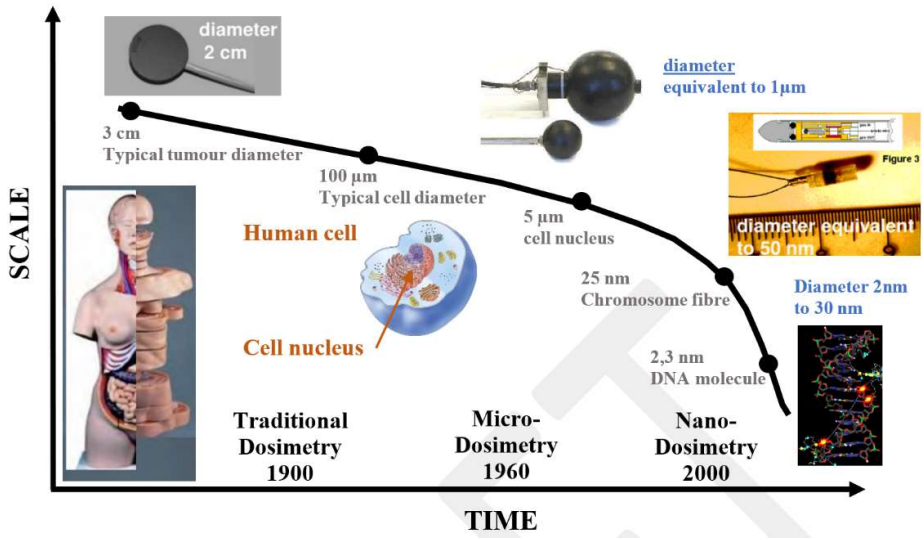

Fig. 1 Radiation dosimetry scales and historical progress in the measurement of radiation at different length scales. The current work is concerned with dosimetry at the nano-scale, at the level of the DNA molecule. Dosimetry at the nano-scale is central to cell killing since damage to segments of the DNA behaves as a function of radiation quality (track structure). Extractyed from (Grosswendt, 2013).

scatter. The field of dosimetry had developed over the years, starting with the formalism of traditional dosimetry systems at the macroscopic dimensions, developed from the beginning of the 1900s when Wilhelm Roentgen discovered x-rays in 1895.

The interaction of radiation with animate matter is a double-edged sword that causes harm but can be used to cure disease and eradicate cancerous cells (Nikjoo, Uehara and Emfietzoglou, 2012). When radiation interacts with biological matter, targeting the human cell nucleus causing genomic instability, DNA damage, mutation, and even cell death. When radiation interacts with matter and deposits energy via ionisation and excitations, a history, called the track structure, is left behind. Depending on the energy and type of the radiation, varied types of tracks

are observed - long and short, thin and flat, sparse and dense – which all depends on whether the radiation in question is a photon, electron, proton, neutron etc. Fig. 4 shows an example of tracks of different directly ionizing charged particles with the same speed in liquid water. The tracks were derived from Geant4-DNA simulations. The different tracks exhibit different ionisation densities. Analysis of the ionisation density of helium (Fig. 4 (c)) shows that a DNA molecule overlayed with this track will produce more clustered damage than for the first two cases (Fig. 4 (a) & (b)). So, both electron and proton tracks do not always produce ionisation in the overlaid DNA molecule, and they result in the same yield of ionisation densities, which indicates that they have identical radiobiological effectiveness.

In this chapter, we will survey current knowledge in radiation dosimetry across all scales and in notable applications such as radiotherapy, radiation protection and radiobiology. A concise presentation of the formalisms and quantities used in energy transfer to the target material and water in particular.

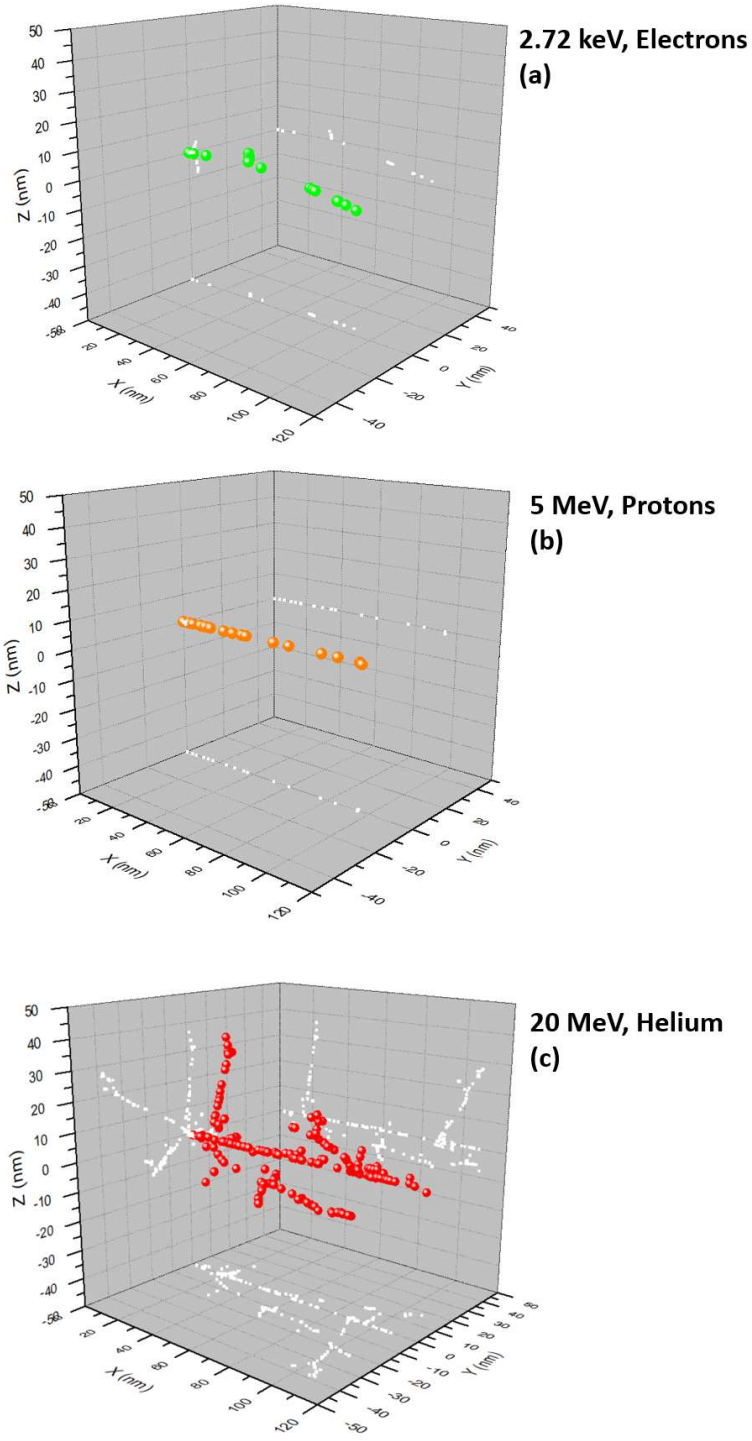

Fig. 3 Charged particle radiation tracks simulated in Geant4-DNA show different ionisation densities, from low (a) to high (c). Diagram (a) is the ionisation density of electrons of 2.72 keV, (b) proton track of energy 5 MeV, and (c) of 20 MeV helium particles. The white squares mark the XY, ZX, and ZY projections of the ionisation points.

2.1.2 **Dosimetry in macroscopic volumes: Macrodosimetry**

2.1.2.1 **Introduction**

Radiation dosimetry is central to the field of medical physics and is concerned with the measurement of the quantity and quality of ionising radiation. It plays a pivotal role in medical physics from the birth of radiation science since the discovery of X-rays at the end of the 19th century. It was initially developed through research efforts in radiation physics and its application in medicine, and it is currently the most important field in radiation physics (Podgorsak, 2016).

The maxim "*Primum non-nocere"* (first, do no harm) has been the central guiding principle for treatment objectives in radiotherapy, i.e., annihilate the tumour while minimizing damage to the critical structures (healthy tissue). This is achieved by delivering maximum radiation energy to the tumorous cells while keeping the absorbed energy (see absorbed dose definition in section 2.1.2.2) to healthy cells as low as possible. To this end, a therapeutic index (ratio) has been defined to quantify the degree by which complication-free control is achieved (Hall, 1985; Tabakov, Franco and Sprawls, 2012; Barrett, Ann; Morris, Stephen; Dobbs, Jane; Roques, 2009; Goitein, 2007; Podgorsak, 2005; Beyzadeoglu, Ozyigit and Ebruli, 2010).

The therapeutic index (ratio), often used as a measure of the efficacy of treatment (Tabakov, Franco and Sprawls, 2012), defines how the TCP relates to the NTCP for different doses (Beyzadeoglu, Ozyigit and Ebruli, 2010). TCP and NTCP curves have a sigmoid relation with absorbed dose, as shown in Fig. 6.

The therapeutic ratio, at times, refers to the ratio of the TCP and NTCP (Podgorsak, 2005), but generally, it is used in a qualitative sense (Goitein, 2007). The therapeutic ratio is dependent on many factors, including the dose rate, the LET of the irradiation in question, and the presence of radiosensitizers or radioprotectors, the planned dose distribution and the accuracy with which treatment is delivered (Podgorsak, 2005).

It is evident from Fig. 6 that there is an intimate relationship between physical dose and clinical treatment outcomes. If the clinician's treatment intent is to be realised, accuracy in dose measurement and calculation must be achieved; otherwise, there is a high price to pay in terms of TCP and NTCP. In radiotherapy, the accuracy with which dosimetry is performed has direct consequences on treatment outcomes. Failure of tumour control or unacceptable typical tissue damage can be a consequence of errors in dosimetry. Both in clinical trial and practice, the assumption is that observed clinical response or outcomes are caused by the delivery of a particular dose. It is expected that dose measurements in radiotherapy should be better than 7% accurate and preferably better than 5% accurate (Sibtain, Morgan and MacDougall, 2012).

In other medical specialities like diagnostic and nuclear medicine imaging, the accuracy of dose to the patient is not as stringent as it is in radiotherapy. However, the radiation dose in these applications should be known to better than ±10% (Podgorsak, 2016). A balance between image quality and the minimization of ionising radiation's deleterious effects requires dose measurement and calculation to this accuracy. This requirement in dose accuracy must typically be fulfilled with respect to doses determined for radiation protection and health physics purposes.

Herein is the guiding principle in the development of macrodosimetry, which is concerned with the measurement and calculation of the physical dose. In this section, we present the Macrodosimetric framework in the context of modern radiotherapy.

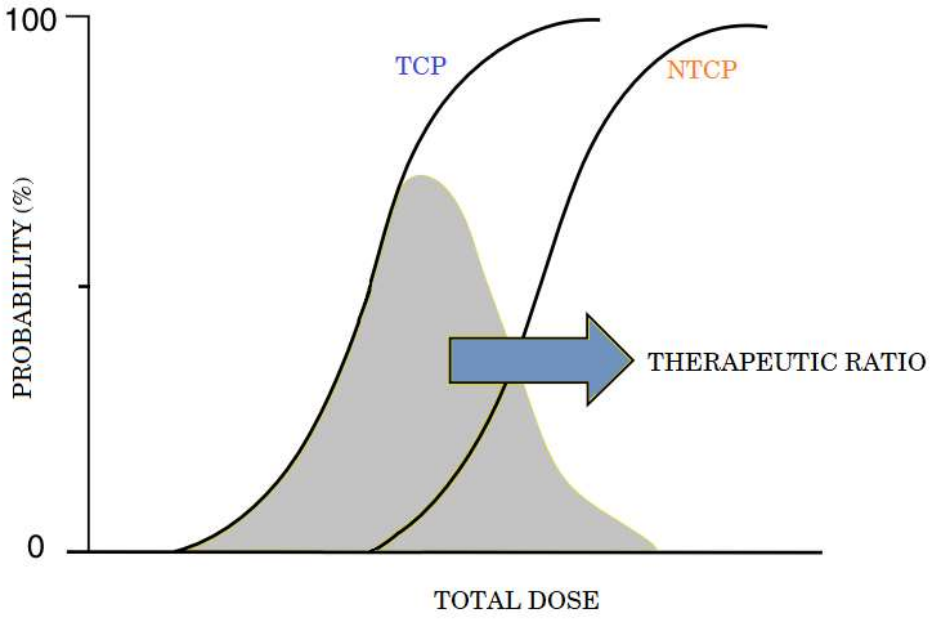

Fig. 5 The principle of the therapeutic ratio. Dependence of the TCP, NTCP and therapeutic ratio on the total dose. The importance of accuracy in the determination of absorbed dose is evident and crucial in radiotherapy. Extracted from (Beyzadeoglu, Ozyigit and Ebruli, 2010)

2.1.2.2 **Macrodosimetric quantities**

The primary physical quantity required in macrodosimetry is the absorbed dose; however, several other physically relevant quantities, characteristic of the radiation source or the radiation beam, may also be of interest. A few of these are radiation source activity, beam fluence, air-kerma in air, and effective dose in an animate medium such as the human body (Podgorsak, 2016). In this section, we will cover some of these quantities that will be useful in the development of Macrodosimetric formalism and principles. Some of these, like absorbed dose, are important in contrasting its applications and limits with quantities developed in nanodosimetry, especially in the context of biological effects of radiation.

Kerma

In the interaction of uncharged particles and matter, the kinetic energy of charged particles released by uncharged particles is ascribed to the quantity kerma. This energy does not include, by definition, the binding energy to overcome, such as to

eject electrons out of their atomic shells. An equivalent quantity called cema is also defined for charged particles. Cema is the energy lost by charged particles (e.g., electrons, protons, alpha particles) in interactions with atomic electrons (in this definition, the binding energies are included). These two quantities, under conditions of charged-particle equilibrium, serve as an approximation to the absorbed dose.

The ICRU (Thomas, 2012) defines the quantity kerma, K, as the quotient of dE_{tr} by dm. In his definition dE_{tr} is the mean sum of the initial kinetic energies of all the charged particles liberated in a mass, dm, of a material by the uncharged particles incident on dm. The unit for this quantity is J kg_{-1} with a unique name gray (Gy).

$$K = \frac{E_{tr}}{dm} \tag{1}$$

Absorbed dose

Absorbed dose, D, is a non-stochastic quantity defined as the quotient of $d\bar{\varepsilon}$ by dm (Seltzer *et al.*, 2011; Faiz M. Khan, 2014; Lindborg and Waker, 2017), where $d\bar{\varepsilon}$ id the average energy imparted by ionising radiation to matter of mass dm. The unit of absorbed dose is Jkg^{-1} and the special name for the unit of absorbed dose is gray (Gy).

$$D = \frac{d\bar{\varepsilon}}{dm} \tag{2}$$

In macrodosimetry, absorbed dose, for practical purposes, is considered a point quantity. Still, it is to be recognised that the physical process does not allow the deferential mass unit dm to approach zero in the mathematical sense. Absorbed dose is related to more fundamental stochastic quantities studied in microdosimetry section 2.2.1.2, including energy deposit ε_i, energy imparted ε, and specific energy z (Podgorsak, 2005).

Absorbed dose has been defined to describe the amount of radiation for all types of ionising radiation, charged and uncharged, for all materials and any energy range (Faiz M. Khan, 2014).

Fluence

The fluence, Φ, of a radiation field is defined as the quotient of dN by dA, where dN is the number of particles incident on a sphere of cross-sectional area dA. The area, dA, is the area perpendicular to the direction of each particle.

The unit for fluence is m^{-2}

$$\Phi = \frac{dN}{dA} \tag{3}$$

- The energy fluence, Ψ, is the quotient of dR by dA. Where dR is the radiant energy incident on a sphere of cross-sectional area dA (Thomas, 2012).

$$\Psi = \frac{dR}{dA} \tag{4}$$

The unit of energy fluence is J m^{-2}. The two quantities above are applicable in the situation were radiation interactions are independent of the direction of the incoming particles.

Linear energy transfer/Stopping power

The quantity LET was defined over half a century ago and was the primary subject of experimental microdosimetry (Lindborg and Waker, 2017). LET was at the time recognised as the suitable quantity to quantify and characterise 'ionisation density' or 'radiation quality', which at the time could provide physical means to explain why different types of radiation cause varied biological impacts.

By definition, the LET, alternatively the restricted linear electronic stopping power, L_Δ, for a particular material and charged particles of a given type and energy are defined as the quotient of dE_Δ divided by dl (Seltzer *et al.*, 2011; Lindborg and Waker, 2017). Where dE_Δ is the average energy lost by a charged particle due to electronic interactions in traversing a distance dl. The mean energy loss excludes the sum of kinetic energies for all electrons released with energy more than Δ.

$$L_\Delta = \frac{dE_\Delta}{dl} \tag{5}$$

The unit of LET is J m^{-1}. Alternatively, keV μm^{-1} is used.

2.2 **Dosimetry In Microscopic Volumes: Microdosimetry**

2.2.1.1 **Introduction**

In the middle of the 20th century, H. H. Rossi and colleagues laid the foundational principles of a new field called microdosimetry (Rossi and Rosenzweig, 1955; Rossi, 1959; Rossi, Biavati and Gross, 1961). The fundamental idea was in developing a framework that considers the stochastic nature of radiation interactions and use it to better understand the relation between the physics and the resulting biological observation, especially in fields such as radiation therapy and radiation protection. The microdosimetric approach contrasts with the classical study of non-stochastic quantities and their inability to predict unique biological outcomes after exposure to radiation. So, the aims of microbiology were and still are to come up with a concise understanding and formalism to predict biological outcomes at cellular levels from physical observation of radiation fields. Formally defined, microdosimetry is a systematic study and quantification of the spatial, temporal, and energy-spectral distributions of energy imparted in cellular and subcellular biological structures and the relation of these distributions to biological effects (Attix, 2008).

Only the main stochastic quantities used in microdosimetry will be presented in this section, and a transparent relation to the corresponding average quantities will also be discussed. It is important to note that the stochastic quantities based on track structure analyses are not meant to replace the well-developed average quantities but are to complement them, especially in presenting information about the probability for the deposited energy to reach a certain volume within a specified volume when an ionising particle interacts with the volume (Lindborg and Waker, 2017).

2.2.1.2 **Microdosimetric quantities**

In microdosimetry, energy deposited in a single interaction is the most fundamental stochastic quantity from which is defined both the energy imparted and the specific energy.

$$\varepsilon_i = \varepsilon_{in} - \varepsilon_{out} + Q \tag{6}$$

The energy deposited, ε_i, in a single interaction, i, and ε_{in}, is the energy of the incident particle (excluding rest energy), ε_{out}, is the sum of all energies of all charged and uncharged ionising particles after the interaction, and finally, Q is the change in the rest energy of a nucleus, if applicable.

Both the imparted and specific energy quantities are relevant to the amount of deposited energy in a defined finite volume. The imparted energy, ε, to matter of a given volume (V) is given by

$$\varepsilon = \sum_i \varepsilon_i \tag{7}$$

Where the summation is done overall energy depositions, see Fig. 8.

The specific energy, z, is then defined by the energy deposited per unit mass, m, expressed in the unit Gray (1 Gy = 1 J/kg).

$$z = \frac{\varepsilon}{m} \tag{8}$$

Specific energy is a stochastic quantity with a variance that increases with decreasing target size. The mean of this quantity is related to the macroscopic quantity absorbed dose (D), by the relation:

$$D = \lim_{m \to 0} \bar{z} \tag{9}$$

Where, $\bar{z}$, is the mean specific energy.

Another essential quantity in microdosimetry related to the imparted energy is the so-called lineal energy, y, defined as the imparted energy ε in the volume, divided by the mean chord length $\bar{l}$ of this volume:

$$y = \frac{\varepsilon}{\bar{l}} \tag{10}$$

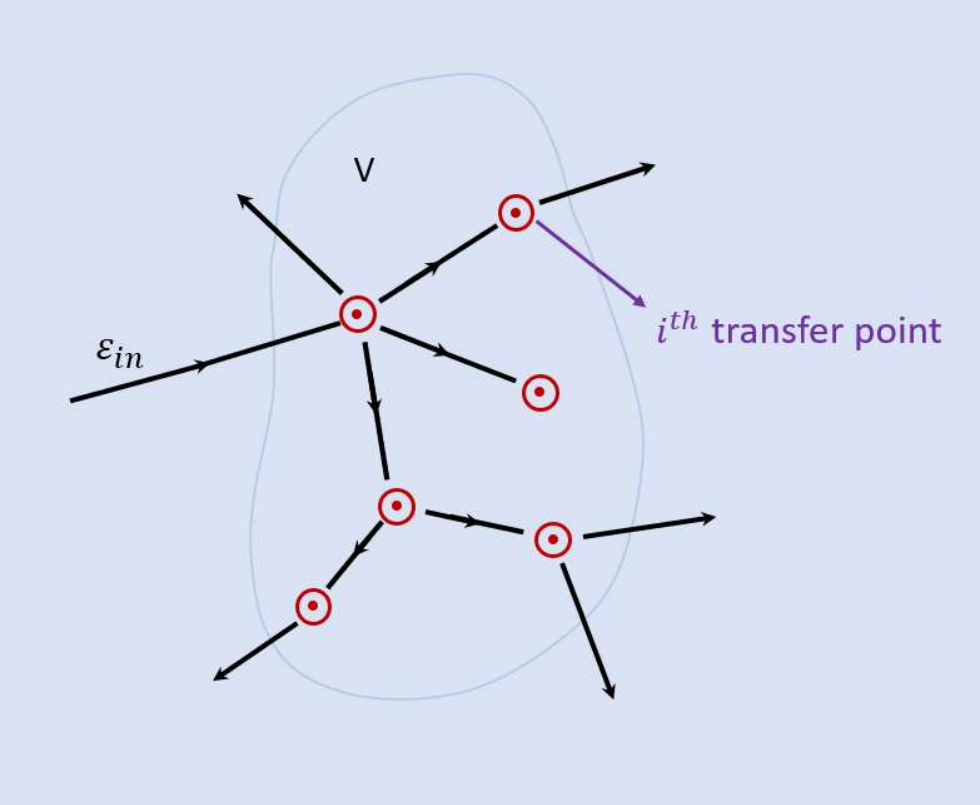

Fig. 7 An ionising particle particle with kinetic energy ε_{in} interacting in the volume V initiates a series of correlated interactions in it. (Kase, Bjarngard and Attix, 1985).

Lineal energy is a stochastic quantity expressed in units of keV/µm. It is related to the macroscopic quantity linear energy transfer (LET).

2.3 **Dosimetry In Nanoscopic Volumes: Nanodosimetry**

Microdosimetry originally studied track structure (Rossi, 1960; Rossi and Zaider, 1996; Cruz and Santa Cruz, 2016) with target sizes in the order of cellular

dimensions. Goodhead discovered a pronounced maximum in RBE at 100 keV/µm (Goodhead, 1994) which corresponds to an average distance between two subsequent interactions in the order of the diameter of the DNA molecule.

Computational investigations on particle track structure indicate that inelastic interactions in the DNA molecule and its surrounding play a key role in the initiation of radiation-induced damage (Cox *et al.*, 1977; Goodhead *et al.*, 1977; Nikjoo and Goodhead, 1991; Brenner and Ward, 1992; Nikjoo *et al.*, 1999). Therefore, the DNA molecule is often considered the most critical target for biological radiation effects (Goodhead, 2006).

2.3.1 **History and microdosimetry roots**

The conceptual basis for nanodosimetry is founded on the need to fundamentally describe radiation beams by defining parameters that will uniquely characterise and provide a complete description of radiation quality and how it relates to both the radiations physical characteristic and, very importantly, the radiobiological implications when interacting with animate matter. To achieve this description, nanodosimetry characterises the ionization component of ionising particle structure by considering the formation of ionization clusters in nanometer-sized target volumes (Rabus, 2020). Radiation track structure was first defined and studied in the field of microdosimetry (Rossi, 1960; Rossi and Zaider, 1996; Cruz and Santa Cruz, 2016) for target sizes on the order of cellular dimensions (i.e. on the micrometre scale) and has been defined as the microscopic pattern of energy transfer points when ionising radiation interacts with matter.

The work of Goodhead revealed a pronounced maximum in the RBE of radiation for most biological endpoints at a LET of 100 keV/µm (Goodhead, 1994). This LET value corresponds to a mean free path of 2 nm for ionisations in water because of their interaction with charged particles. It is noteworthy that this dimension coincides with the diameter of the double helix structure of the DNA (deoxyribose nucleic acid) molecule.

The extension of microdosimetry concepts and theory to the nanometre regime encountered insurmountable limitation (Amols, et al., 1990). Thus, a paradigm shift

from measurement quantities related to imparted energy to ionization clusters (Grosswendt, 2004) was followed and forms the basis of nanodosimetry. The work by Pszona in 1975 (Pszona, 1975) laid the basic concepts and foundation of nanodosimetry as a tool for the experimental study of charged particle track structure.

2.3.2 **Nanodosimetric framework: formalism and quantities**

2.3.2.1 **Introduction**

As stated previously, section 2.1.2, the concept of absorbed dose is only applicable in macroscopic volumes and is used extensively in prescription regimes in radiotherapy units that are used to realise desired clinical endpoints. However, in microscopic volumes of molecular DNA, a new dosimetric framework based on a detailed particle track description is necessary. A move from absorbed dose to microscopic quantities is necessary because 1) the mean energy lost (represented by the LET) of a passing trajectory is not a sufficient quantity to represent DNA damage, the actual energy deposited or the number of interactions in the target are the significant quantities to be considered (International Atomic Energy Agency, 2007). Secondary electronic equilibrium is crucial in the determination of absorbed dose, but in high energy particle tracks, this condition is not fulfilled. The residual range of secondary electrons produced is much larger than the microscopic DNA targets' dimensions, which complicates the determination absorbed dose. The meaning of absorbed dose as a continuous macroscopic quantity breaks down when the target size becomes too small 2) Energy deposited in the target volume (microscopic in this case) should be determined accurately. For macroscopic volumes, the *W*-value, which is the mean energy required to produce an ion pair, provides a reasonable indication of absorbed energy since the number of ionisations in these volumes is large. In microscopic volumes, however, this *W*-value is not applicable. Energy deposited in microscopic volumes is best described by specific probability density distributions (International Atomic Energy Agency, 2007).

The work by Goodhead, including other investigators (Cox *et al.*, 1977; Goodhead and Thacker, 1977; Brenner and Ward, 1992; Nikjoo *et al.*, 1999) explored the

influence of inelastic interactions occurring at the site or in the vicinity of DNA on radiation-induced damage. The work by Brenner and Ward (Brenner and Ward, 1992) demonstrated that a correlation exists between clusters of multiple ionisations in nanometric sites of DNA (2-3 nm) with yields of double-strand breaks. After a few decades, the field of nanodosimetry has been developed and aims to establish a concept of radiation quality based on measurable properties of the ionisation component of the particle track structure (Nettelbeck and Rabus, 2011; Rabus and Nettelbeck, 2011).

The state of the art of the nanodosimetry framework is separated in two approaches: First, the experimental approach of nanodosimetry is based on the idea that the spatial distribution of ionisation events resulting from the interaction of ionising radiation with matter can be linearly scaled with the density (Hilgers, 2010). The implication is that macroscopic volumes of low-pressure gas can be used as surrogates for microscopic condensed matter of water volumes that simulate nanometric biological targets such as the DNA. Secondly, the simulation approach used for investigations in the field of nanodosimetry that employs track structure (TS) Monte Carlo simulation used to study the radiation interaction with matter. This tool is used for the calculation of the energy deposited in biological structures of nanometric dimensions. This is in contrast to condensed history codes, which are used in the simulation of average energy loss of primary particle for a specified track length. Track structure codes simulate interactions event by event until the particle loses all its energy or reaches a pre-set low energy limit.

2.3.2.2 **Nanodosimetry: Quantities**

The concept of absorbed dose is not applicable to nanometric volumes at the level of the DNA. Therefore, a new formalism defined in the field of nanodosimetry is based on the track structure of the ionising particles and their statistical characteristics.

It was apparent to investigators (Pszona, 1975) that knowledge of the number of ionizations in nanometric volumes created by an ionising particle traversing tissue is of particular importance in relating DNA strand breaks to ionisations created by

charged particles. Building from the concepts developed by Pszona and other investigators, the idea of cluster size was developed and has become central to nanodosimetry. A cluster, in this context, defined as the spatially correlated group of ionizations created by a primary particle (including its secondary electrons). Several investigators have worked to develop the fundamental concepts in nanodosimetry based on track structure. Below is a summary of the basic formalism aimed at introducing concepts and quantities.

Consider a cylindrical volume of diameter *D*, filled with water, shown in Fig. 10, immersed in a water medium, both simulating 1) short segment of DNA (10 base pairs) and 2) surrounding medium around the DNA, respectively. A single primary particle of radiation quality Q (defined by particle type and energy) traversing the volume at a distance d from the cylinder's main axis. The impact parameter d varies from $d = 0$ to relevant radial distances where $d > 0$. In this case, the number of ionisations produced within this volume is referred to as the ionisation cluster size υ.

To characterise the radiation quality Q, $P(\upsilon|Q)$, the statistical distribution of probabilities that υ ionisations occur within the target volume is used in nanodosimetry (Grosswendt, 2004). The cluster size is a result of the superposition of the ionization component of the particle track structure and the simulated geometric characteristics of the target volume. The probability $P(\upsilon|Q)$, therefore, describes the stochastic nature of the conjunction of track structure and the target volume. Consequently, in experimental nanodosimetry, this probability distribution and its moments, $M_\xi(\upsilon|Q)$, depend on the quality of the primary particle, defined by the particle type and its energy, and the material characteristics, defined by the density of the gas used in the interaction volume, the shape and size of the target volume, and on the distance d.

$$M_\xi(Q|d) = \sum_{\upsilon=0}^{\infty} \upsilon^\xi P_\nu(Q|d), \; with \sum_{\upsilon=0}^{\infty} P_\nu(Q|d) = 1 \qquad (11)$$

Both the first moment $M_1(Q|d)$ which stands for mean cluster size, and the second moment $M_2(Q|d)$, describing the fluctuation or cluster-size formation, defined by,

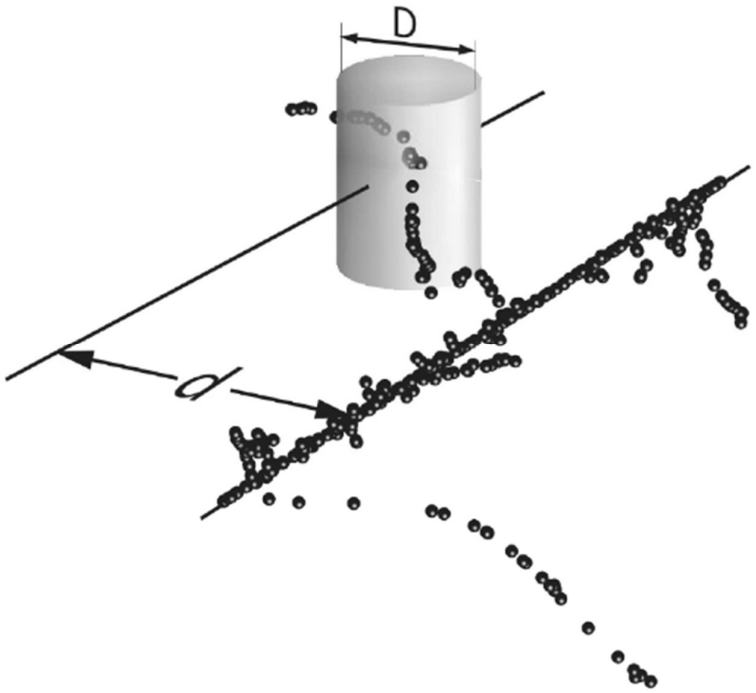

Fig. 9 A schematic representation of ionization cluster size formation by a primary particle passing a specified cylindrical water volume of diameter *D* at a distance *d* from the cylinder's main axis. (Grosswendt, 2004)

$M_2(Q|d) - M_1(Q|d)^2$, expressed as the variance.

An important quantity in nanodosimetry used to relate the probability of initial DNA damage, like strand breaks, and nanodosimetric quantities derived from the track structure is the cumulative frequency of the probability distribution $P_\nu(Q|d)$ in nanometric cylindrical volumes.

The complementary cumulative probability, $F_k(Q|d)$ of cluster size $\nu \geq k$, is defined as follows.

$$F_k(Q|d) = \sum_{\nu=k}^{\infty} P_\nu(Q|d), where\ k = 1, 2, 3, 4 \ldots \qquad (12)$$

To date, the conceptual development of nanodosimetry has followed two main approaches to correlate nanodosimetric quantities to initial DNA damage:

2.3.2.3 **The Grosswendt approach.**

The fundamental principle in this approach is that the radiation quality of the track in question is directly proportional to physical dosimetric quantities based on track structure. In his approach, Grosswendt made two hypotheses (Grosswendt, 2004):

- The probability to create at least 1 ionisation, $F_1(Q|d)$, in the volume representing the DNA or surrounding water molecules is expected to be directly proportional to the probability to create a sing strand break (SSB).
- Similarly, the probability of creating at least two ionisations, $F_2(Q|d)$, in the same DNA volume and its surrounding water molecules is expected to be directly proportional to the probability of creating a double-strand break (DSB).

Characterization of a particle track structure at the nanometric scale uses the concept of the frequency distribution of cluster size. Statistical parameter (like the first and second moments of this distribution as discussed above), derived from this distribution are used in practice as surrogates to represent the track structure. The proportionality of the cumulative distribution $F_2(Q|d)$ suggested by Grosswendt's approach has some support, but some literature suggests that this proportionality, between F_2 and the probability of double-strand break creation, might only be valid for low-LET radiation qualities (Nettelbeck and Rabus, 2011; Rabus and Nettelbeck, 2011; Lazarakis *et al.*, 2012).

2.3.2.4 **The approach proposed by Schulte and Garty.**

In this approach (Garty *et al.*, 2006, 2010; Schulte *et al.*, 2008), the use of combinatorial analysis to calculate the conditional probabilities that a cluster size of υ will result in a strand break of a cluster size of n_{SB} in the same DNA segment. Similarly, the probability that a single strand break cluster-size of n_{SB} results in a DSB is also determined. A free parameter representing the probability that

ionisation is converted into a strand break is determined from biological experiments of plasmid DNA assays (Leloup *et al.*, 2005).

2.3.3 **Experimental Nanodosimetry**

Water is ubiquitous in biological tissue and is therefore often used as a substitute (model) of biological tissue. As alluded to above, measurements in nanoscopic volumes of condensed matter are not practical and are emulated using interaction volumes filled with low-pressure gas, in which electron-ion gas pairs are generated by the interaction of radiation with the gas molecules. The resulting ions or electrons from a volume with scaled dimension equivalent to condensed matter in nanoscopic dimensions are counted and considered representative of condensed matter. Currently, three nanodosimeters based on this approach are in use. One of these devices is based on the counting of electrons and two on counting single ions. These instruments are primarily used to sample the track structure by measuring the ICSD of charged particles. Below are a brief description and the measurement principles of these devices.

2.3.3.1 **Detection of Ions**

Ion counting detectors count ions instead of electrons. Because of their massive size, relative to electrons, ions have a lower initial kinetic energy and reduced diffusion, and therefore simulation of smaller sensitive volumes relative to devices counting electrons is possible. Detection of ions, however, is challenging and requires high vacuum conditions.

The Ion Counter Nanodosimeter

The ion counter (Garty *et al.*, 2002), is used to detect positive ions produced in a gas target volume of dimensions simulating a short segment of DNA with a diameter of 2-3 nm. The ion counter, Fig. 12, was initially developed with the capability to measures the ICSDs for a central passage of the primary ion in nitrogen and propane gas (other gases can be used). Further developments of this instrument have made it possible to not just measure the central passage of primary ions, but

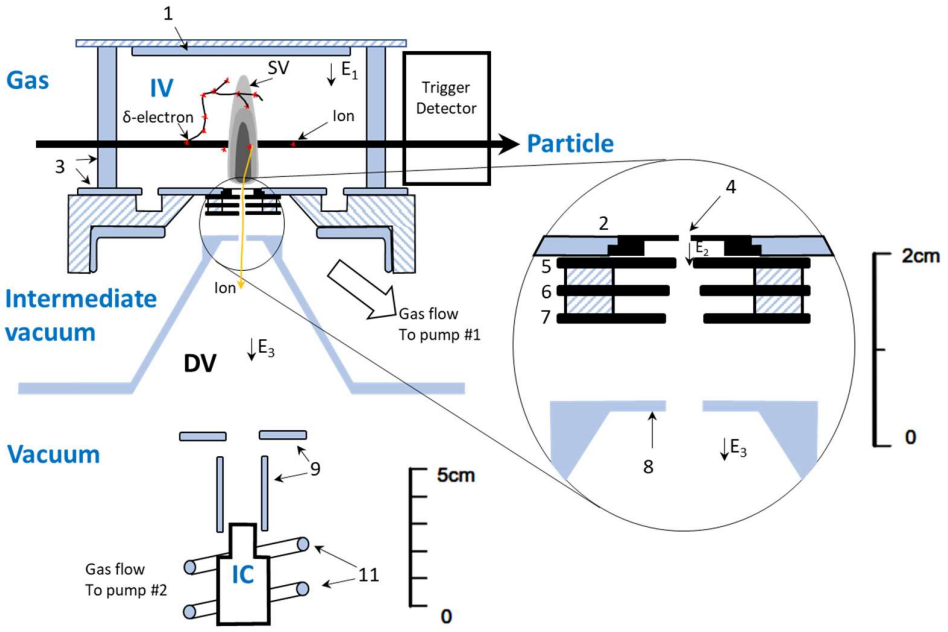

Fig. 11 A diagram of the ion counting nanodosimeter. The ion extraction field E1 inside the ionisation volume (IV) is determined by the anode (1), cathode (2) and field-shaping electrodes. (Garty *et al.*, 2002)

the measurement of the penumbra is also made possible (Hilgers *et al.*, 2015; Hilgers, Bug and Rabus, 2017).

Primary charged particles passing through the ionisation volume create ions. Ions that overlap with the sensitive volume (SV) are extracted using the electric field in the IV via the small aperture (4) into the intermediate vacuum space (Garty *et al.*, 2002). A system of electrodes A_1-A_4 (5-8) is used to focus these ions on the detection volume (DV) for counting. The DV accelerates the ions (to amplify the signal) and focuses them using electrode (9) into the ion counter (IC) for pulse generation. To protect the ion counter from discharges, the ion counter has a helical coil (11) installed. Note that the diagram is not to scale. The SV and δ-electrons are schematic representations to showcase features of an ion counter.

The Jet Counter nanodosimeter

The Jet Counter was developed by the group of S. Pszona (Pszona, Kula and Marjanska, 2000)) in 1994. A unique feature of this instrument is that positive ions are counted from a pulse of nitrogen gas so adjusted that the number of molecules' density can vary to simulate corresponding biological target linear sizes of about 2 nm to 20 nm. The device measures ICSDs that sample the central passage of the primary particle through the target.

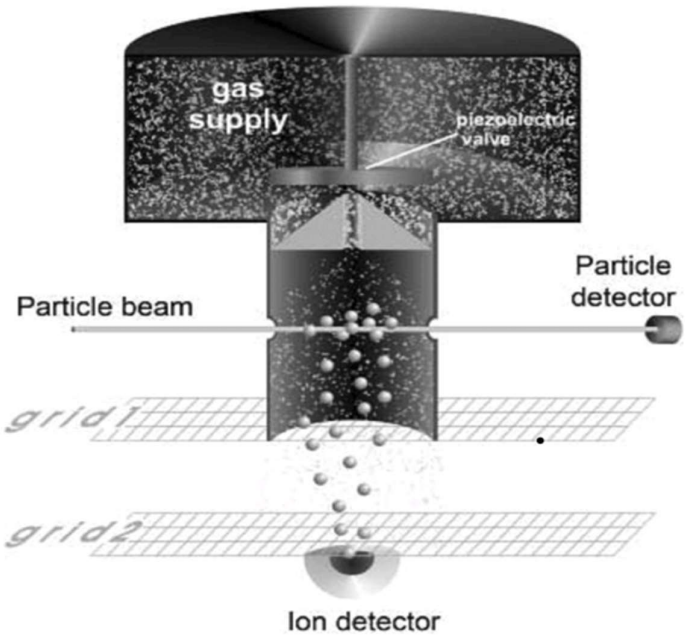

Fig. 13 A schematic depiction of a Jet counter used in the measurement of ionization cluster-size distributions for both alpha particle and low energy electrons as primary particles. Time of arrival techniques are used to count ions produced in the interaction chamber. Different trigger techniques are used for alpha and electron particles. For electrons, the time of arrival is measured from the period in which primary electrons are introduced into the interaction chamber by the electron gun. As for alpha particles, the time-of-flight is triggered by the signal of a silicon detector. (Pszona, Kula and Marjanska, 2000)

The measurement principle, as shown in Fig. 14, is that a pulse expansion of a gas (e.g. nitrogen) in an interaction chamber would lead to a pulsed jet of gas molecules. Primary particles interact with gas volume to produce ions which are extracted into

a vacuum and detected by an ion counter as a function of arrival time. The arrival time is referenced from a trigger signalled by the primary-particle detector.

2.3.3.2 **Detection of electrons**

The StarTrack counter nanodosimeter

Based on the counting of electrons, the StarTrack nanodosimeter was developed at the Laboratori Nazionali di Legnaro in Italy (De Nardo *et al.*, 2002), working with the Weizmann Institute of Science in Israel (Breskin *et al.*, 1995).

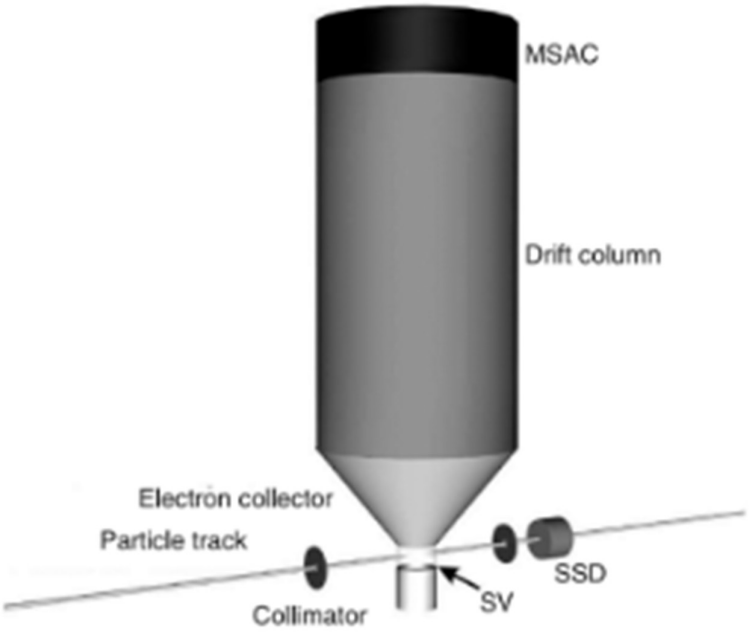

Fig. 15 A schematic representation showing electron counting StarTrack nanodosimeter (not to scale). The diagram shows the counter set-up where a particle track creates ionisation in the sensitive volume (SV) of the cylindrical shape of both diameter and height equal to 3.7 mm. Electrons created in this volume are then transferred into a 17 cm-long drift column. The multiple-step avalanche chamber (MSAC), multiplies the electrons by a factor of 10^7. The solid-state detector (SSD) triggers the electron signal acquisition. (De Nardo et al., 2002)

The StarTrack counter nanodosimeter is used to measure the probability distribution of ionisation cluster-size formation and the radial distribution of ionizations within the track in nanometric volumes. Fig. 16 presents a schematic representation of the StarTrack nanodosimeter apparatus.

2.3.4 **Monte Carlo simulations**

Monte Carlo codes are used to calculate the complex transport phenomenon of radiation as accurately as possible. This is done by simulation techniques, using a computer experiment, where pseudorandom numbers are generated repeatedly. If the probability law for the elementary processes relevant to the interaction processes is known, the physical processes are then generated on the computer as if they actually occur, and the investigation of the resulting behaviour studied (Nikjoo, Uehara and Emfietzoglou, 2012). Data summarising the interactions of photons, electrons, and ions with matter are known together with quantitative data like cross-section, energy transfers, energy spectra, and angular distributions for most interactions. Monte Carlo codes, employing numerical techniques, use these data to solve the radiation transport problem.

There are two groups of Monte Carlo radiation transport: First, the so-called condensed history simulations. These are primarily concerned with the transport problem of macroscopic dimensions (macroscopic target size). Condensed history codes combine many single interactions into one single step to provide fast and practical calculation times while providing adequate accuracy. Stopping power data are used to determine the energy loss of particles in a medium. For the transport of generated electrons, multiple scattering theories are applied. Examples of condensed history codes are given by Nikjoo and colleagues (Nikjoo *et al.*, 2006). Secondly, in microscopic and nanoscopic dimensions – relevant to the context of the current study - of cells and DNA, respectively, Monte Carlo radiation transport is only possible through track structure simulation codes. The section below discusses the definition and characteristics of track structure simulation codes.

2.3.4.1 **Track structure Monte Carlo Simulations**

Track structure simulation codes have been in development since the 1960s and are particularly used in transporting particles interaction by interaction and provide a detailed spatial distribution of interaction points describing particle tracks (Nikjoo *et al.*, 2006). Track structure codes can provide the distribution of coordinates of all interactions of charged particles in 3D space and the time frames that interactions occur, either physical, chemical, or biological. Due to the stochastic nature of radiation interactions, interaction cross sections are extensively used since they provide probability information on the interactions of particles with the medium. The capability to resolve the transportation of individual interactions comes at a cost; such simulations are time-consuming and thus are limited to microscopic spatial dimensions.

Track structure codes are generally classified into three distinct groups based on the timescale after the initial interaction of the particles with the medium. First, several codes focus on the physical track structure occurring from the time of the first interaction at 10^{-15}s to 10^{-13} s (Paretzke *et al.*, 1991). Examples are GEANT4_DNA (Incerti, Ivanchenko, *et al.*, 2010) or PTra (Grosswendt, 2002). Physical track structure codes provide 3D information like the distribution of physical events (ionization, excitation, and elastic scatterings). Secondly, the chemical stage happens within the 10^{-13} to 10^{-12} after the first interaction, where the transport of chemical productions formed during and after the physical phase happens. Examples of track structure codes are PARTRAC (Friedland *et al.*, 1999) and KURBUC (Uehara and Nikjoo, 2006). Since 2016, the chemical stage has also been included in the Geant4_DNA toolkit. Finally, for periods $>10^{-12}$, due to both physical and chemical events stated above, biological processes, such as DNA damages and repair, would be the result. Examples of codes simulating such biological processes are PARTRAC (Friedland *et al.*, 1999; Friedland and Kundrát, 2013) and the TOPAS-n-Bio toolkit based on the Geant4_DNA extension to Geant4 (Schuemann *et al.*, 2019).

2.3.5 **Geant4-DNA Monte Carlo Code**

Geant4 is a Monte Carlo toolkit that is written in the object-orientated language of C++ and is available as an open-source from the GEANT4 website (*GEANT4 Collaboration Website*, 2020). Its application ranges from High energy physics (for which it was developed) to low energy packages that have numerous applications, including both the medical and radiation protection fields (Santin *et al.*, 2003; Rodrigues *et al.*, 2004; Schulte *et al.*, 2005; Allison *et al.*, 2006). The toolkit is capable of simulating a variety of particles and energies. Particles that can be simulated within the framework of the GEANT4 based application include leptons, photons, hadronic subatomic particles, and ions with an energy range from as low as 250 eV extending into the TeV range.

For micro- and nanodosimetry applications, the low threshold energy for electron transport is useful, and further improvements in the low energy transport through the GEANT4-DNA project (Incerti, Ivanchenko, *et al.*, 2010; Bernal *et al.*, 2015; Incerti *et al.*, 2018).

Step by step simulations of the physical interactions of particles down to very low energies (~10 eV) in liquid water and DNA constituents are performed using a variety of physics models. Physics model development is an active field of research in theoretical radiation physics. It is currently not possible to fully validate the developed models in liquid water due to the lack of experimental data. The software's current model includes capabilities to simulate the Physico-chemical and chemical stages of water radiolysis in the irradiated medium for up to 1 µs after irradiation (Incerti *et al.*, 2018). The "Geant4-DNA" Monte Carlo toolkit, as a track structure simulation code, provides a detailed treatment of all interactions using single-scattering models, which offer an appropriate spatial resolution for small biological targets.

The user can choose from a variety of physics models offered by Geant4-DNA. The models simulate the physical interactions of electrons in liquid. Interactions in the Geant4-DNA package are grouped into three categories: 1) Elastic interactions (i.e., elastic scattering), 2) Inelastic interactions (electronic excitation and ionisation),

and 3) inelastic subexcitation interactions (vibrational excitation and molecular attachment that apply to electrons with low energy not capable of electronic excitation or ionisation).

The current version of Geant4-DNA offers a selection of three recommended physics constructors for the simulation of discrete particle interaction in liquid water. A constructor is a simulation module in Geant4 that collects all required lists of particles, physics processes, and associated models required by a Geant4-DNA simulation. The three constructors in the Geant 4-DNA toolkit are named "G4EmDNAPhysics_option2", "G4EmDNAPhysics_option4", and "G4EmDNAPhysics_option6". These constructors employ different models for the simulation of electron interactions. Electron capture and electron loss interactions are simulated using analytical parametrisations based on experimental data in the vapour phase. All three constructors handle the interaction of protons, neutral hydrogen, alpha particles and their other charged states, heavier ions (Li-7, Be-9, B-11, C-12, N-14, O-16, Si-28 and Fe-56), in an identical way. In summary, nuclear scattering is modelled using classical mechanics. Velocity scaling of electron excitation cross-sections (also used for both hydrogen and alpha particles and their charged states) is used for protons to simulate electron excitation for low energy (<500 keV). For energies above 500 keV, proton ionisation is based on the Born and Bethe theories and the dielectric formalisms. A summary of each Geant4-DNA physics construction and the models employed are provided in Table 5 Ratio of the results obtained for cylindrical targets and cylinder shell segments both with the same volume) for the specified proton start energies Ep and the first four cumulative ICS frequencies using option 1 (see section 3.2.3) for defining the cylinder shell segments. The values are the ratios for the largest radial distance where both scoring approaches were applied. The last row shows the mean over the five energies and the associated sample standard deviation (given in brackets as multiple of the last significant digit).

Ep / MeV	F1	F2	F3	F4

1	1.18	1.18	1.19	1.21
3	1.08	1.08	1.09	1.11
10	1.11	1.12	1.11	1.12
30	1.12	1.14	1.13	1.14
100	1.15	1.18	1.19	1.25
mean	1.12(4)	1.14(4)	1.14(5)	1.17(6)

Table 6. All simulations in this work were done using the "G4EmDNAPhysics_option2" constructor. The use of other constructors is reserved for future work in order to compare comparing the results acquired in this study.

Table 2 Content of the three reference Geant4-DNA physics constructors for TS simulations for TS simulation of electrons in liquid water available in the Geant4 10.4 release. Indicated also is the tracking cut below which the tracking of electrons is stopped, and their remaining kinetic energy is locally deposited (*).

Process	Geant4-DNA physics constructors electron models		
	G4EmDNAPhysics_option2	G4EmDNAPhysics_option4	G4EmDNAPhysics_option6
Ionisation (inelastic)	Emfietzoglou dielectric model (11 eV-1 MeV)	Emfietzoglou-Kyriakou dielectric model (10 eV-10 keV)	Relativistic binary encounter Bethe model from CPA 100 Code (11 eV-256 keV)
Electronic excitation (inelastic)	Emfietzoglou dielectric model (9 eV-1 MeV)	Emfietzoglou-Kyriakou dielectric model (8 eV-10 keV)	Dielectric Model from CPA100 Code (11 eV-256 keV)
Elastic scattering (elastic)	Partial wave model (7.4 eV-1 MeV)	Uehara screened Rutherford Model (9 eV-10 keV)	Independent Atom Method model From CPA100 code (11 eV-256 keV)
Vibrational excitation (inelastic subexcitation)	Sabche data (2 eV-100 eV)	n/a	n/a
Attachment (inelastic subexcitation)	Melton data (4 eV-13 eV)	n/a	n/a
Auger electron emission	From the EADL database and the Geant4 atomic relaxation interface		
Default tracking cut(*)	7.4 eV	10 eV	11 eV

Table 3 Content of the three reference Geant4-DNA physics constructors for TS simulations for TS simulation of electrons in liquid water available in the Geant4 10.4 release. Indicated also is the tracking cut below which the tracking of electrons is stopped, and their remaining kinetic energy is locally deposited (*).

2.3.6 **Development of nanodosimetry**

Experimental methods that allow track structure details to be measured in gas counters that simulate target sizes of nanodosimetric dimensions (Bantsar *et al.*, 2018) were developed at the beginning of this century. These methods resulted in the development of the three nanodosimeters that are in use today for the study of track structure (section 2.3.3).

2.3.6.1 **The European BioQuaRT project.**

An intercomparison performed as part of the European project, BioQuaRT (Rabus *et al.*, 2014; Palmans *et al.*, 2015), between these three European nanodosimeters produced the seminal discovery of the universal relation among the statistical parameters of the frequency distributions of ionization cluster sizes in different nanometric target volumes (Conte *et al.*, 2017). The work of Grosswendt (Grosswendt, 2005) suggested this direct relation between nanodosimetric quantities and radiobiological effectiveness, and it is currently assumed to be the basis of the so-called track-event theory (Besserer and Schneider, 2015a, 2015b). There have been doubts raised about the simple one-to-one correlation between ionisation cluster frequencies and the resulting biological consequences (Nettelbeck and Rabus, 2011; Rabus and Nettelbeck, 2011; Bug *et al.*, 2014) because of the stochastics involved in the relation between ionisations and DNA lesions (Garty *et al.*, 2006, 2010). The BioQuaRT project has, as one of its motivations, looked at clarifying this issue through a comprehensive investigation of the internal consistency of nanodosimetry, as well as links between nanodosimetry and microdosimetry and their relation to biological endpoints. Parallel research, both within the BioQuaRT project and independent studies worked on the so-called multi-scale approaches encompassing both micro- and nanodosimetry (Palmans *et al.*, 2015; Villegas *et al.*, 2016; Cunha *et al.*, 2017; Friedrich *et al.*, 2018). Furthermore, the application of nanodosimetric track parameters in treatment planning has also been explored (Casiraghi and Schulte, 2015; F. Alexander *et al.*, 2015; Frauke Alexander *et al.*, 2015).

2.3.6.2 **Current developments in experimental nanodosimetry.**

Ongoing work in experimental nanodosimetry is currently being done in the development of condensed-phase nanodosimetric detectors (Heimbach *et al.*, 2017), the measurement of correlations of track structure parameters for several nanometric targets in spatial proximity (Pietrzak, Pszona and Bantsar, 2018), (Hilgers and Rabus, 2020) as well as novel approaches to extend microdosimetric measurements into the nanometer regime (Bortot *et al.*, 2017). Research is underway in computational simulation studies to extend nanodosimetry to clinical situations, e.g. in consideration of multi-target situations (Selva, Conte and Colautti, 2018).

An overarching challenge that remains is the establishment of uncertainty budgets for nanodosimetric track structure parameters obtained by measurement (Rabus *et al.*, 2019) or simulation (Villagrasa *et al.*, 2019).

2.3.7 **The basic applications of nanodosimetry**

Projected applications of nanodosimetry are varied and expected to influence several fields. Nanodosimetric studies can be used in the determination of radiation quality and how it affects dose distribution within patients during radiotherapy and thus could be incorporated into treatment planning systems that include biological objective functions. For instance, applications in radiation protection include the effect of radiation on radiation devices and the protection of astronauts in complicated radiation fields found in space (Garty, 2004; Wroe, 2007).

2.4 **Radiobiology**

2.4.1 **Introduction**

About half of cancer patients with cancer receive radiotherapy at some point during their treatment (Tobias, 1996; Jacob *et al.*, 2005; Barton *et al.*, 2014; Delaney and Barton, 2015). Extensive use of radiotherapy is on the rise due to the ageing population in China, Europe, and North America and increased diagnosis of cancers in low- to middle-income countries (Salminen, Izewska and Andreo, 2005; Smith

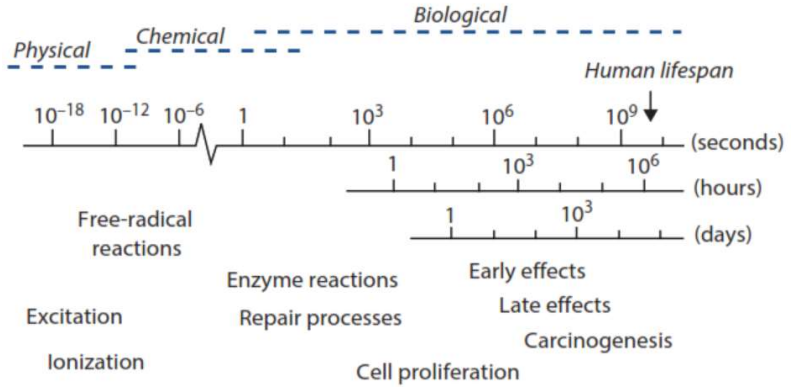

Fig. 17 Timescale of the effects after irradiation of biological systems. (Joiner and Kogel, 2018).

et al., 2010; Pan *et al.*, 2016). The long history of surgery continues to yield good results as the primary mode of treatment for many tumour types in the range of early non-metastatic malignancies. For the long-term control of many tumours, including head and neck, lung, cervix, bladder, prostate and skin, radiotherapy is an excellent alternative to surgery as it achieves a reasonable probability of tumour control accompanied with acceptable cosmetic results. Also, radiation plays a vital role in the management of palliative cancer patients (Joiner and Kogel, 2018). Large numbers of patients receive chemotherapy during their treatment, and both useful symptom relief and disease arrest are observed.

Much current research is focused on the improvement of radiotherapy and chemotherapy. Realistic estimate to improve cancer cure rates by, say, 2% would mostly be achieved by increasing the results of radiotherapy alone from say 15% to 17% than by doubling the results achieved by chemotherapy alone. To improve radiotherapy outcomes, one might raise the standards of radiation dose prescription and delivery to those currently used in best radiotherapy centres, improving radiation dose distributions (high conformal radiotherapy with photons, or by the use of proton or carbon-ion beams), using image guidance during delivery, and by exploiting radiobiological initiatives (Joiner and Kogel, 2018).

The connection between physics and biology is evident as in the now increasing use of proton and heavy-ion beams in radiotherapy. One of the primary motivations for the use of these treatment modalities is their high radiobiological effectiveness

compared to conventional treatments with photons and electrons. Therefore, a detailed understanding of heavy-charged particles' biological properties is necessary to effectively use these now-famous radiations.

2.4.2 **The role of radiation biology in radiotherapy**

Physical, chemical, and biological processes follow in succession immediately after the irradiation of any biological system. These resulting processes are enormously different in timescales from the initial interaction, see Fig. 18. During the physical process, primarily, charged particles interact with atoms in the tissue. A high-speed electron takes about 10^{-18} seconds to traverse a DNA molecule and about 10^{-14} seconds for a mammalian cell. In its path, it interacts primarily with orbital electrons by ejecting them from their molecules and raising others to higher energy levels within their atoms (excitation). Ejected electrons may, if having sufficient energy, in turn, go on to cause a cascade of further electrons.

For a 1 Gy absorbed dose delivered in tissue, there are over 10^5 ionisations within every cell's volume with a diameter of 10 μm (Joiner and Kogel, 2018). Rapid chemical reactions follow readily after the physical stage to mark the chemical phase, which is characterised by the reaction of the damaged atoms and molecules with other cellular components - the result of the chemical reactions yields ‘free radicals’ within the irradiated volume. Free radical reactions are complete within approximately one milli-second of radiation exposure. The final phase, the biological phase, begins with an enzymatic reaction that acts on the residual damage, where the vast majority of lesions in DNA are successfully repaired. Some lesions fail to repair and ultimately lead to cell death.

Improvements in the management of cancer using radiotherapy over the last few decades have resulted mainly from improvements in technology, especially dose delivery techniques aided by new imaging tools (Lee *et al.*, 2014; Chetty *et al.*, 2015; Beaton *et al.*, 2019; Mohan *et al.*, 2019; Fiorino *et al.*, 2020). However, there is a shortage of published work directly linking advances in these technologies and clinical outcomes. Amongst these technical improvements, the introduction of intensity modulation and various functional imaging modalities such as functional

magnetic resonance imaging and PET/CT. These advances have led to novel concepts like 'biological target volume', 'dose painting', and 'theranostic imaging'. These developments will continue to improve tumour control rates and reduce tissue morbidity.

Parallel to these developments, strides in radiobiology that help in understanding cancer biology, and radiation response, in particular, are crucial to achieving significant improvements in radiotherapy.

2.4.3 **DNA damage by ionising radiation**

The principal damaging effect of ionising radiation arises from its ability to eject electrons from (ionise) molecules within cells. The majority of biological damage in tissue is caused by the secondary electrons, with sufficient energy, after their ejection from the atoms that go on to cause further ionisation in molecules they collide with, progressively slowing down as they go. As the electrons slow down and lose more energy, clusters of ionisation are created (Goodhead, 2006). Fig. 18 shows the pattern and density of ionisations and their spatial dimension in relation to the DNA molecule.

The DNA molecule in the figure is represented by a double helix molecule containing two strands linked by hydrogen bonds. Each strand is a linear chain composed of 4 bases adenine (A), cytosine (C), guanine (G) and thymine (T) connected by sugar molecules and by a phosphate group. The molecule has complementary bases on opposite strands, resulting in base pairs A-T, and C-G, and their order is the genetic coding unique to determine regulatory elements and protein amino acid sequence. Clustered ionisations about the DNA molecule are unique to ionising radiation, which makes it hard for the damage to be repaired. Clustered damage to the DNA has a high potential of causing permanent damage to the DNA that can be serious and often lethal.

Numerous scientific studies have long shown that the DNA molecule is the principal target for radiation-induced cell killing (Munro, 1970). Biological systems responding to assault of the DNA molecule and have developed well-evolved and

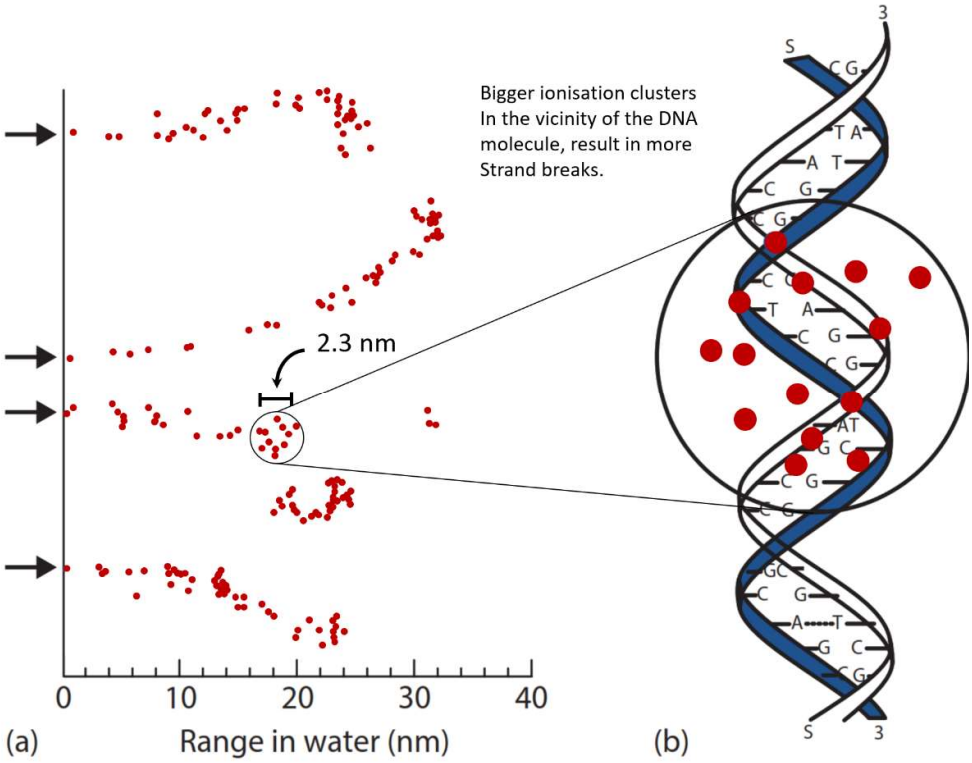

Fig. 19 (a) Computer simulated tracks of 1 keV electrons. Observe the scale relative to the 2.3 nm diameter of the DNA molecule. (b) Showcases the concept of local multiply damage due to a cluster of ionisations in a DNA. Figure adapted from (Joiner and Kogel, 2018).

specialised repair systems that detect and repair damage to bases, single-strand breaks (SSB), double-strand breaks (DSB) and cross-links. Ionising radiation produces all these lesions and more. The repair mechanism present in biological systems is suited to repair all types of damage, the success of which depends on the type of lesion and complexity. Of all DNA lesions caused by ionising radiation, DSB is considered the most lethal as they are the most difficult to repair. DSB can cause chromosome and chromatid damage if misrepaired or not repaired. A discussion of the repair mechanisms of any damage is beyond the scope of this work

and will not be covered. For a summary of repair mechanisms, see the reference (Joiner and Kogel, 2018). In the current context, the clustered damage intensity determines the severity of the resultant lesion, which is proportional to the difficulties in repair and cell death's high potential.

2.4.4 **Quantification of cell kill**

To quantify cell killing after irradiation of biological tissue to a known dose of ionising radiation, cell survival curves are employed. They are plots of the survival fraction of cell colonies irradiated with known doses to the colonies of cells without irradiation given by Eq. 13 below.

$$Surviving\ fraction = \frac{PE_{treated}}{PE_{control}} \qquad (13)$$

The so-called linear-quadratic (LQ) model is used to represent the resulting survival curves. To date, the simple LQ formula gives a better description of radiation response in dose regions considered in radiotherapy. Numerous methods have been proposed to predict tissue response to radiation dose, but the LQ models have been widely used in radiation biology.

2.4.5 **Relative Biological Effectiveness (RBE)**

X-rays and γ-rays used in radiotherapy are uncharged electromagnetic radiations with individual photons (‘packets’ of energy) energetic enough to ionise molecules in tissue that they penetrate. As discussed before, this results in the biological effects seen in radiotherapy. In general, photon radiation has roughly the same biological effect per unit dose, there is, however, small dependence on the energy with lower energies, but for practical considerations, conventional radiation with photons has the same biological effect per unit dose. Biological effects due to high energy photons is a result of ionisations by energetic electrons set in motion by photon interactions. Therefore, treatment with energetic electron beams has the same biological effectiveness to high-energy photon beams. An alternative to conventional treatment with photons (x- and γ-rays) and electrons, ‘particle therapy’ is currently on the rise. Particle therapy uses protons, neutrons, α-particles,

fully stripped carbon ions or even heavier ions. Particle therapy is characterised by a higher biological effect per unit dose compared with conventional therapy. It is also significant to note that charged particle therapy has significantly different depth dose profiles compared to uncharged particles (i.e. neutrons) or conventional electromagnetic radiation, which provides for different dose distributions for charged particles.

At the scale of the cell nucleus, γ-rays rays deposit most of the energy in single isolated ionisations or excitations; because of sparse ionisation intensity, most of the damage is efficiently repaired compared to the damage caused by few tracks of α-particles (Goodhead, 1988). The density of ionisation from any radiation is characterised by the quantity LET, defined in section 2.1.2.2.

Defined below in Eq. 14 is the quantity relative biological effectiveness (RBE) used to quantify the biological effectiveness of the radiation in question.

$$RBE = \frac{Dose\ of\ reference\ radiation}{Dose\ of\ test\ radiation} \qquad (14)$$

The reference low-LET radiation is commonly 250 kVp X-rays or Co-60 γ-rays. The dependence of the RBE on LET presents a curve that rises to a maximum at a LET of about 100 keV μm^{-1}, then falls for higher values of LET due to overkill.

2.5 **Contemporary Radiotherapy**

2.5.1 **Introduction and history**

X-ray radiation was used immediately after discovery in 1895 by Roentgen, both for diagnostic and therapeutic purposes (Scharf and Wieszczycka, 2001). The development of X-ray tubes essentially led to kilovoltage X-rays dominating radiotherapy for the first half of the 20th century and was classified into 3 broad categories as superficial therapy (10-150 kV), deep therapy or orthovoltage therapy (200-300 kV). Because of the skin limiting effects of low energy x-ray beams used in the formative years of radiotherapy, attempts were also made to search for sources of more penetrating radiation with attention focused on gamma-emitting

radionuclides. Radium sources were used, but their wider use and acceptance was limited by the cost and their availability. The era of megavoltage beams was assured by the development and use of cobalt sources in 1950. This resulted in the depth-dose curve that exhibits skin-sparing properties compared to low energy radiation in the kV and lower ranges. The skin-sparing properties of megavoltage beams overcame the problem of the dose-limiting structure being the patient's skin. Dose escalation protocols to deep-seated tumours were now possible without exceeding the tolerance of the skin. Several generators that use high energy photons have been developed and used for the treatment of cancer using both electrons and photons for the treatment of superficial and deep-seated tumours. Treatment of cancer using megavoltage energies, enabled by Linear accelerator technologies, has led to the success of radiotherapy as one of the primary modalities in cancer management in the last three decades.

Technological advances in computers have led to parallel advances in imaging techniques that have had a tremendous effect on the development of radiotherapy. Examples of imaging technology that have revolutionised radiotherapy and have evolved from the planar 2D x-ray images and have led to the high tech, and individualised modality that it is today, including computed tomography (CT) scans, magnetic resonance imaging (MRI) with and without spectroscopy, Ultrasound imaging, positron emission tomography (PET) scans, and electronic portal imaging, which has developed to advance in-room patient positioning verification modalities like kV- and MV- cone-beam computed tomography (CBCT). These imaging technologies have led to improvements in our ability to identify macroscopic or microscopic disease. Most of these techniques have been developed and used in the context of photon and electron radiotherapy techniques used to manage most cancer patients receiving radiotherapy.

2.5.2 **Conventional radiotherapy tools**

In 2-dimensional planning, one to four-photon beams are utilised and simple parallel opposed and simple lateral arrangements planned to give an optimum dose coverage to the treated area. From this straightforward beam arrangement, exact

conformity guided by soft tissue was impractical and was made possible by the advent of CT imaging which also made it possible to plan axial anatomy and complex tissue contours such as the hourglass shape of the check and shoulders. While limited, 3D planning allows accurate dose calculations for irregular shapes. The advent of intensity-modulated radiotherapy (IMRT) has dramatically changed the radiotherapy landscape and has allowed greater control of dose distributions for the target by controlling the intensity of radiation within any one beam. Advanced treatment planning with inverse planning capabilities has made it possible to reproduce complicated plans that have a steep gradient to maximise the dose to the target while, at the same time, minimising the dose to normal tissue. Identification of microscopic disease and appropriate immobilisation of the patient during IMRT has been some of the challenges facing modern radiotherapy. 4D treatment and imaging techniques have been developed over the past two decades to about for both voluntary movements of patient tumours and visceral motion such as respiration and digestion.

For the conventional linear accelerator with both photons and electrons: The depth dose characteristics of electrons show a maximum range, in centimetres, of almost half the initial energy of the beam, expressed in MeV. Because of this, electron beams are suited for the treatment of superficial or semi-deep tumours. In contrast, photon beams develop a build-up effect (about 3.5 cm for 18MV beam) and characterised by the absorption of exponential type. These characteristic result in the skin-sparing effect and make these beams suitable for deep-seated tumours.

Despite the success of electron Linacs, radiation-resistant tumours present a challenge to photon or electron irradiation because of their non-responsiveness to these modalities (Scharf and Wieszczycka, 2001). Secondly, because of the unavoidable associated dose to neighbouring healthy tissue in photon treatments, the required tumoricidal dose cannot be given to tumours. In response to these challenges, hadronic radiotherapy has been developed and uses particles such as neutrons, protons, pions, helium, or heavier ions for the treatment of radioresistant tumours, including those that are located near critical body structures (Scharf and Wieszczycka, 2001). The current work studies the properties of proton tracks

exclusively by looking at radiobiological effects of these particles when interacting with animate matter.

2.6 Treatment With Sparsely Ionising Radiation And Heavy Charged Particles

2.6.1 Introduction and History

Particle accelerator technology was first reported in the literature in 1936 when Lawrence developed the first cyclotron in Berkeley. Accelerated protons and heavier ions were first proposed for use in radiotherapy for human patients in 1949 by Robert Wilson (Wilson, 1946; Delaney, Thomas and Kooy, 2007). From 1954 through December 2018, at least 221.528 patients have been treated with particle therapy worldwide (*Particle Therapy Co-Operative Group*, 2019). Paediatric and ocular melanomas and, in general, radiation-resistant tumours stand to gain from the optimum use of particle therapy modalities. About 1% of all cancer patients treated with radiotherapy worldwide receive particle therapy (Rath and Sahoo, 2016). There is currently significant interest in Hadron therapy; Fig. 22 below shows the patient statistics published by the Particle Therapy Co-Operative Group.

The recorded number of patients treated with He, Pions and other ions (except for Carbon ions and protons) are reported as constant since 1992 (1994 for Pions) since these therapies have been discontinued or have not been on the rise. Of significant

interest is the number of proton and carbon-ion patients that have been on the rise since 2007.

Protons are said to give relatively low doses in healthy tissue outside of treated

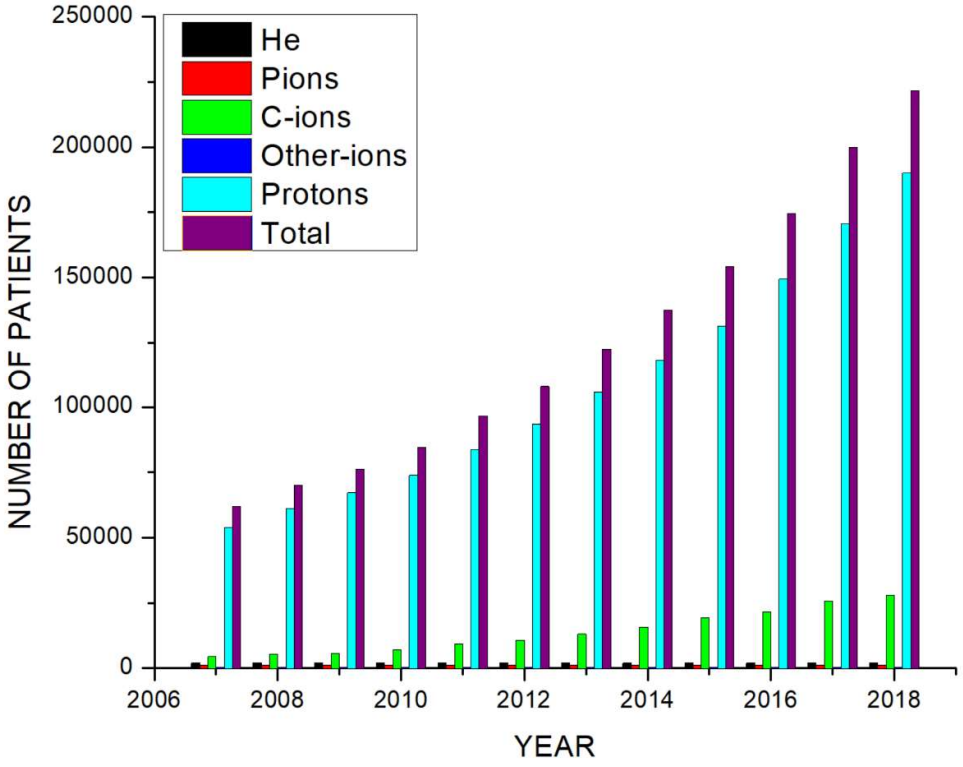

Fig. 21 Patients treated with hadron therapy worldwide. The first use of hadron modalities in patient treatment started in 1954 (*Particle Therapy Co-Operative Group*, 2019).

volume when compared to treatments using photons. Additionally, the dose for protons can be made much more uniform throughout the treatment volume, including the edges (Koehler and Preston, 1972; Rath and Sahoo, 2016). Koehler also showed that the use of protons and heavy charged particles makes possible substantially improved control of the geometric distribution of treatment radiation than for treatments with photons and electrons, which suggest better clinical control for certain types of malignant tumours and reduced complications rates.

2.6.2 **Physical properties of particle radiation**

The depth dose properties of protons are different from those exhibited by photons because they are massive and charged and therefore have minimal scattering when penetrating the tissue and deliver the highest dose near the end of their range, which is known as the BP after which the is a steep fall of dose in a short distance. As early as 1974, it was pointed out that based on the physical factors such as higher LET, the particle of choice for radiotherapy are protons and helium ions, see figure

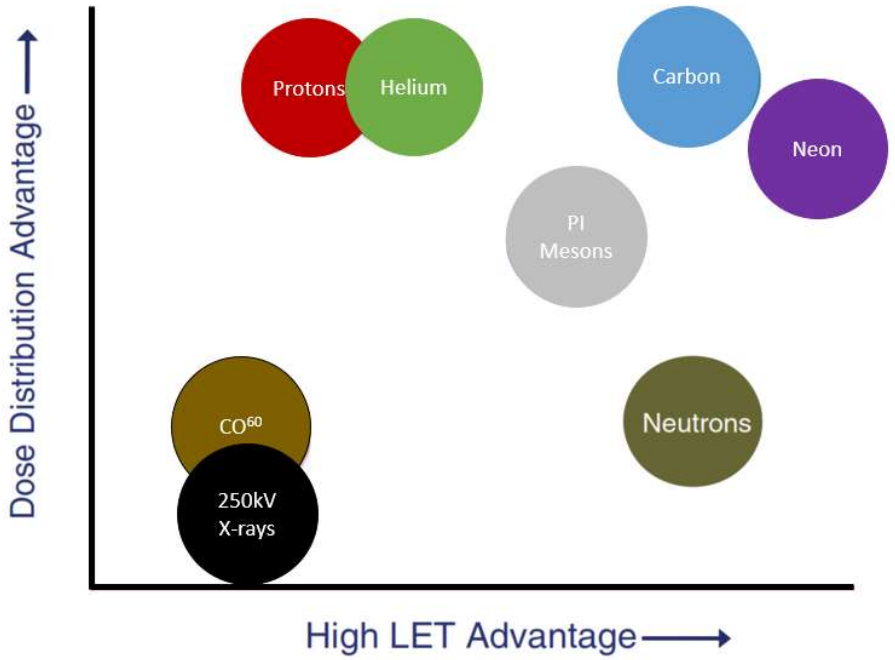

Fig. 23 Dr Raju's demonstration the relative advantage of particles in 1974 that represent the relative merits of high LET particles. Protons have a low LET advantage but have desirable ballistic properties (Raju, 1974).

below (Raju, 1974).

The motivation to explore and use charged particles was motivated by unique physical characteristics. In particular, is the dose vs depth graph of a proton beam showing the characteristic nearly flat curve to about the terminal 1cm of the proton range but increases sharply to give a distinct localised high-dose region referred to as the BP. The depth dose curve of protons is because these charged particles have

minimal scattering when penetrating matter and because of the protons degraded energy, give the highest dose at the end of their range. This physical attribute of proton depth dose distribution is used in clinical applications by designing distributions of proton energies that would result in varying depths of the BPs so that there could be a flat high dose region covering the extent of the tumour. This resultant flat high-dose region is referred to as the spread-out Bragg peak (SOBP) and is graphically shown in Fig. 26.

Advantages of protons beams over photons are evident in this picture, i.e., a significantly lower dose is delivered to tissue beyond the distal edge of the SOBP peak (mainly by a secondary radiation field of neutrons) and lesser dose proximal to the target. The implication of these properties results in a mean dose delivered to normal tissue, which means the tolerance to the patient can be increased, which would allow for dose escalation in the target, improving the complication-free tumour control probability. Proton beams can utilise many beams, which can be planar and non-coplanar, static or dynamic, conventional or intensity modulate as photon therapy.

The effects of protons are not markedly different from those of high-voltage X-rays if equal radiation doses are compared. A review of proton therapy's physical, technical, radiological, and clinical status shows that protons have dose distributions and range that give unique features that can be leveraged for therapeutic gains. The integral dose in photon treatments is generally about 2-5 times that found for proton treatment (Archambeau *et al.*, 1974; Paganetti *et al.*, 2019).

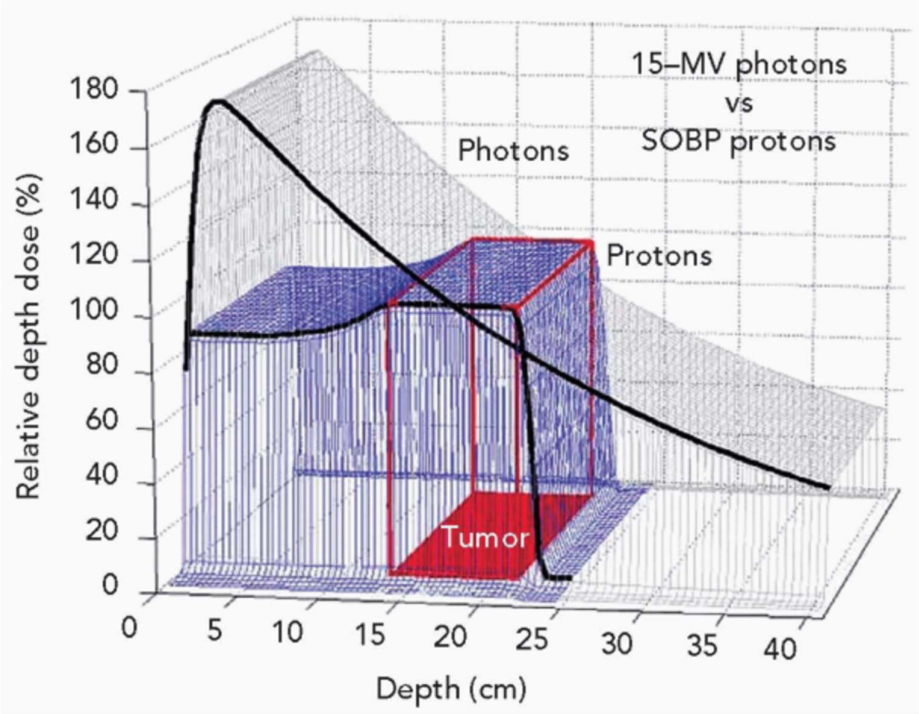

Fig. 25 Aspread-out Bragg peak of 23 cm range and 12 cm modulation with a sing field of 15 MV photons (Delaney, Thomas and Kooy, 2007).

2.6.3 **The rationale for charged particle therapy**

The rationale for particle therapy is due to both the physical depth dose properties and biological effectiveness of particulate (non-electron) radiation. Heavy charged particles exhibit the so-called Bragg Peak, where relatively large doses are deposited at a specific depth (depending on the energy of the radiation) and very small doses beyond the depth of the BP. Heavier ions have their interactions with the media in a low-dose fragmentation tail of lower atomic number particles distal to the end of the range of the primary particles.

The primary rationale for using heavier charged particles for radiotherapy is their biological effectiveness. Based on an average of multiple experiments, in proton therapy, a relative biological effectiveness (RBE) of 1.1 has been used in the clinic (for all cancers and healthy tissue). The LET for heavier ions is much higher than for protons which means that these particles produce more complex DNA double-

strand breaks, and therefore, result in even higher RBE. in addition, they have a lower oxygen-enhancement ratio (OER). Both these features (high RBE and low OER), especially around the BP, give these modalities a radiobiological advantage that is geared to lethal cell killing, especially for resistant tumours.

As discussed previously, the LET increases as particles slow down until all their energy is used up; in that case, they come to a sudden stop. The resulting depth dose curve is shown in section 2.6.4, Fig. 28.

2.6.4 **Relative biological effectiveness of protons**

Protons and heavy charged particles are biologically more effective than photons and electrons (Paganetti, 2012). The prescription of dose in the clinic is adjusted from the physical dose used in conventional radiotherapy to a dose level that takes into account the relative biological effectiveness of charged particles. Because of our limited knowledge of the biological effects of charged particles, there is inherent uncertainty in the determination and hence clinical application of the RBE, and this would have unwanted consequences on clinical outcome. Amongst other factors (dose per fraction, total dose, oxygenation etc.) (Robertson *et al.*, 1975; Paganetti *et al.*, 2002; Britten *et al.*, 2013; Girdhani, Sachs and Hlatky, 2013), the RBE of protons is a function of the depth of penetration (implicit on LET). Despite the dependence of RBE on these parameters, especially with depth, current clinical practice has adopted a constant RBE value of 1.1 in all situations (Delaney, Thomas and Kooy, 2007; DeLuca, Wambersie and Whitmore, 2007). The use of an RBE of 1.1 in the clinic may lead to an increased risk of injury to the surrounding normal tissue where the RBE higher than 1.1 or to recurrence in the tumour in an instance where the RBE less than 1.1.

A few arguments have been put forward to support the continued use of the RBE of 1.1, amongst which is the claim that the increased RBE is biologically inconsequential since it happens in a region of a very rapid fall-off in dose (Rath and Sahoo, 2016). The value 1.1 is based on animal experiments performed in the early days of proton therapy (Dalrymple, Lindsay, Ghidoni, *et al.*, 1966; Dalrymple, Lindsay, Hall, *et al.*, 1966). An obvious benefit in using a single RBE for protons

that the application of dose conversion is straightforward (which is advantageous in clinical trials). It has long been argued that the use of this constant value is not unreasonable because no clinical data show unexpected side effects (Paganetti, 2012).

Counter arguments to the use of a constant RBE in techniques like intensity-modulated Proton Therapy (IMPT) is that the dose distributions contributed by individual beams are highly heterogeneous. The implication is that the biologically effective dose delivered may be substantially different from the dose based on RBE of 1.1. In addition, the inherent flexibility of IMPT offers the capability to capitalise on variable RBE through the incorporation of such information into the treatment planning process.

As previously mentioned, in clinical practice, proton beams are generally applied such that a SOBP with a flat dose profile is formed, where up to now, a constant RBE of 1.1 has been used for tumour cell killing (Paganetti *et al.*, 2002; *Relative Biological Effectiveness in Ion Beam Therapy*, 2008; Paganetti, 2014). Recent studies, however, have reported increased RBEs for protons at the end of their range (the distal end of the BP), which is significantly larger than 1.1 (Chaudhary *et al.*, 2014; Matsumoto *et al.*, 2014; Anferov and Das, 2015; Tommasino and Durante, 2015; Tung, 2015; Giovannini *et al.*, 2016; Jones, 2016, 2017; Grün *et al.*, 2017; Howard *et al.*, 2017; Willers *et al.*, 2018; Ilicic, Combs and Schmid, 2018; Newpower *et al.*, 2019).

A review of numerous experimental biological data (Lühr, von Neubeck, Krause, *et al.*, 2018; Lühr, von Neubeck, Pawelke, *et al.*, 2018) found that proton RBE for cell survival averaged over all cell lines varies from 1.1, which is only confirmed at the centre and distal edge of the SOBP, and this RBE value rose to as much as 1.15 and to 1.35, respectively, wherein the distal fall-off region it was reported to be 1.7 and in some cases (in conventional fractionation) even 4-6.

Studies based on in vitro experiments using human cell cultures reported LET-related increase in RBE, depending on the position in the SOBP, with the largest values reported at the distal fall-off (Chaudhary *et al.*, 2014; Paganetti, 2014; Lühr, von Neubeck, Krause, *et al.*, 2018). Interestingly, another group (Słonina *et al.*, 2014) have found RBE values of 1.1 using similar experimental settings. An in vitro study by (Chaudhary *et al.*, 2014) observed an underestimation of the biologically effective dose delivered to the SOBP for normal human fibroblasts and radiation-resistant glioma cells, which was as much as 18.3% and 17.9%, respectively. In another study by (Matsumoto *et al.*, 2014), RBE values 1.56 times higher at the distal edge than at the centre of the SOBP were reported. An extension of the SOBP

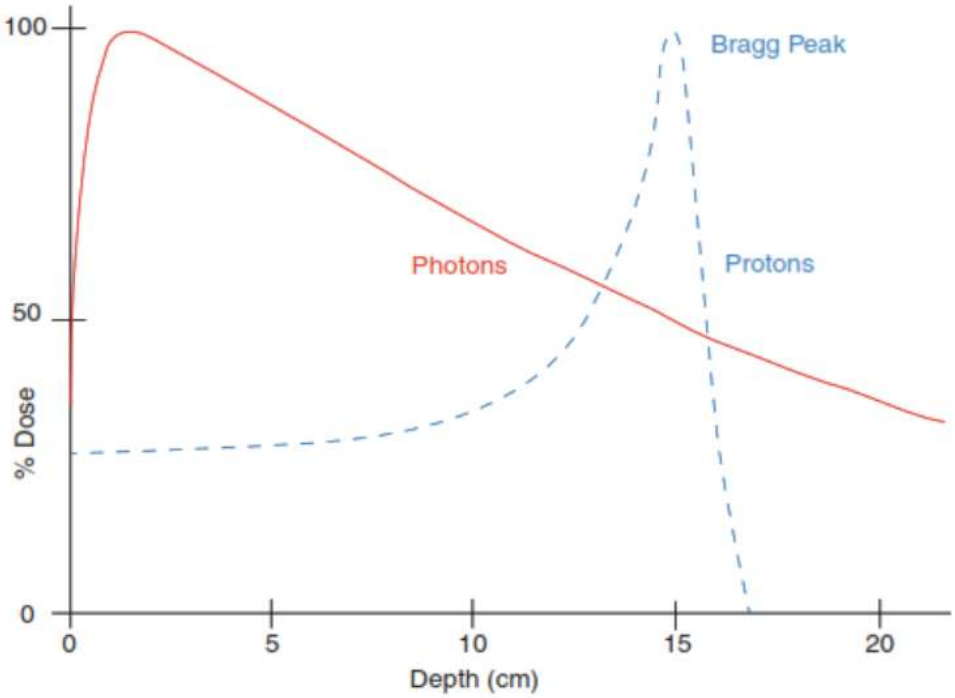

Fig. 27 A typical depth dose characteristics of protons and photons in water.

range of up to 4.1 mm for the iso-effective dose result was also observed.

2.6.5 **Accurate determination of RBE**

Current clinical results indicate that the RBE in proton therapy is not constant and varies from the 1.1 value used in the clinic today. Indications are the RBE may be

of the order of 1.0 at the entrance and higher than 1.3 at the BP and points beyond (Rath and Sahoo, 2016). In-vivo and in-vitro studies are currently being undertaken to accurately map the RBE as a function of the various parameters.

2.6.6 **Physical characteristics of heavy charged particles**

In particle therapy, both for protons and heavy charge particles, the energy of the therapy beam is used to determine the range needed. The Bethe formula (derived by Hans Bethe in 1930), Eq. (15), which is the energy lost per pathlength (dE/dx), or collision stopping power, describes the loss of energy of charged particles primarily due to inelastic collisions with target electrons. The expression in Eq. (15) describes the mass collision stopping power as a function of the velocity for relativistic heavy charged particles.

$$\frac{S_{coll}}{\rho} = K.z^2.\frac{Z}{A}.\frac{1}{\beta}.\left[\frac{1}{2}ln\left\{\frac{2m_e c^2.\beta^2.W_{max}}{I^2.(1-\beta^2)}\right\} - \beta^2 + corr\right] \quad (15)$$

Where $K = 0.307075\ MeV\ cm^2 g^{-1}$, z is the charge of the projectile ion, Z/A is the average ratio of the atomic number divided by the atomic mass of the medium, W_{max} is the maximum energy that the ion can transfer to an electron in a single collision, I is the mean excitation energy of the medium, and *corr* represents all corrections (density effects, shell, Barkas and Bloch corrections) which are significant to consider at both very high and low energies. Eq. (15) explains the depth dose of heavy charged particles characterised by the BP.

In addition to the coulombic interactions of projectile protons with atoms, non-elastic nuclear reactions and Bremsstrahlung (negligible at therapeutic energies) do occur, albeit less frequently. In the nuclear reaction, the proton enters the nucleus; the nucleus then emits a proton, deuteron, triton, or heavier ion or one or more neutrons. The main influence of proton nuclear reactions is a slight decrease in absorbed dose due to the removal of primary protons, compensated to a large extent

by the liberation of secondary protons and other ions (including neutrons), that contribute to the absorbed dose in the medium (Newhauser and Zhang, 2015).

In a high-energy proton treatment beam, secondary protons produce as much as 10% of the absorbed dose and have a small but non-negligible contribution on the spatial dose distribution in a patient (Medin and Andreo, 1997; Paganetti *et al.*, 2002). Recoil protons by elastic collisions with the hydrogen atom gradually become dominant behind the Bragg peak's distal fall-off region (Matsuzaki *et al.*, 2010).

Also, to be considered is that the interaction of therapeutic proton beams with the patient results in secondary neutrons' production scattered in the lateral directions. These neutrons also generate low-energy protons that contribute to the absorbed dose (Matsuzaki *et al.*, 2010).

2.6.7 **Range of the depth -dose curve**

The range of a particle is dependent on its initial energy. Fig. 30 below showcases the median (or nominal) range from the PSTAR database plotted against the initial energy for monoenergetic particles.

Assuming the continuous slowing down approximation (CSDA), the range can be calculated by integrating Eq. (15) over the energy of the particle:

$$R_{csda} = \int_{E_0}^{0} \frac{1}{S_{col}} . dE \qquad (16)$$

When the particle reaches the BP, there is a spread in energy that has developed because, in each of the inelastic collisions with bound atomic electrons along their track, the particle transfers different amounts of energy at each interaction from the start position. The particles that transfer a larger (smaller) amount of energy during the inelastic collisions will have the shortest (longest) range. This effect causes the energy-loss straggling, and it is the reason for the smearing out of the BP (BP) (Ma and Lomax, 2013).

The energy-loss straggling effect above results in a gaussian distribution, s(x), of ranges about an average residual range given by Eq. (17) below.

$$s(x) = \frac{1}{\sqrt{2\pi\sigma_x}} e^{-(x-R)^2/2\sigma_x^2} \tag{17}$$

The standard deviation, σ_x, is almost proportional to the r(residual) range R.

2.6.8 **LET dependence of RBE**

RBE is a complex quantity because it depends on the LET, dose, particle type, energy, tissue type, and biological endpoints. In this work, we are particularly concerned with the variation of RBE with beam quality, which is sometimes characterised by LET.

The average spacing between energy ionisation events along the track is of the order of hundreds of nanometers for low LET, but the average spacing between ionisation events is less than a nanometer for high LET radiations (100 keV/µm). Interaction between ionisation events in one track event results in a higher probability of irreparable damage even from that track, called clustered damage. Increasing the LET, therefore, increases the effectiveness until saturation. After saturation, the RBE decreases as the LET continues to increase because effectiveness stays the same while the dose increases with higher LET. The decrease in RBE with increasing LET (> 100 keV/µm) is called the overkill effect, see Fig. 32 below. It is important to note that for different ions, the RBE as a function of LET is different, the position of the maximum appearing at higher LET values for particles with a

higher charge (Belli *et al.*, 1992, 1998; Jenner *et al.*, 1992). Given the fact that LET is a macroscopic quantity at a cellular level, the LET concept is only a crude approximation of beam quality because the track structure and micro- and even nano-dosimetric effects are thought to play a role.

As is evident from Eq. (15), the difference between a proton and heavy ions in the depth dose characteristic is primarily due to the z^2term: the lower charge of protons leads to lower energy loss per pathlength compared to a high charge value of heavy

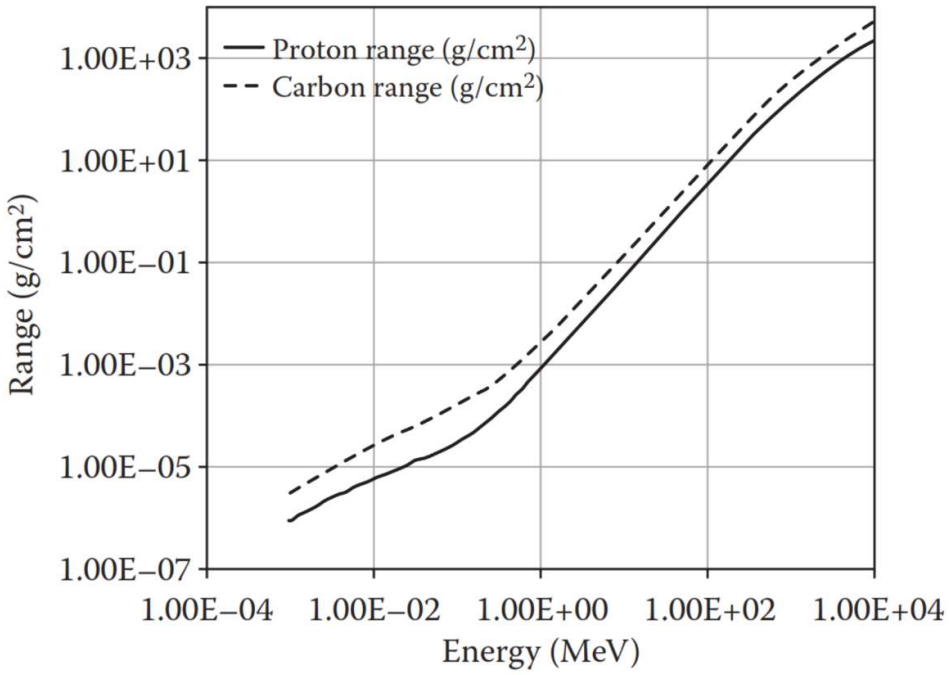

Fig. 29 Residual range in water for proton and carbon particles. (Ma and Lomax, 2013)

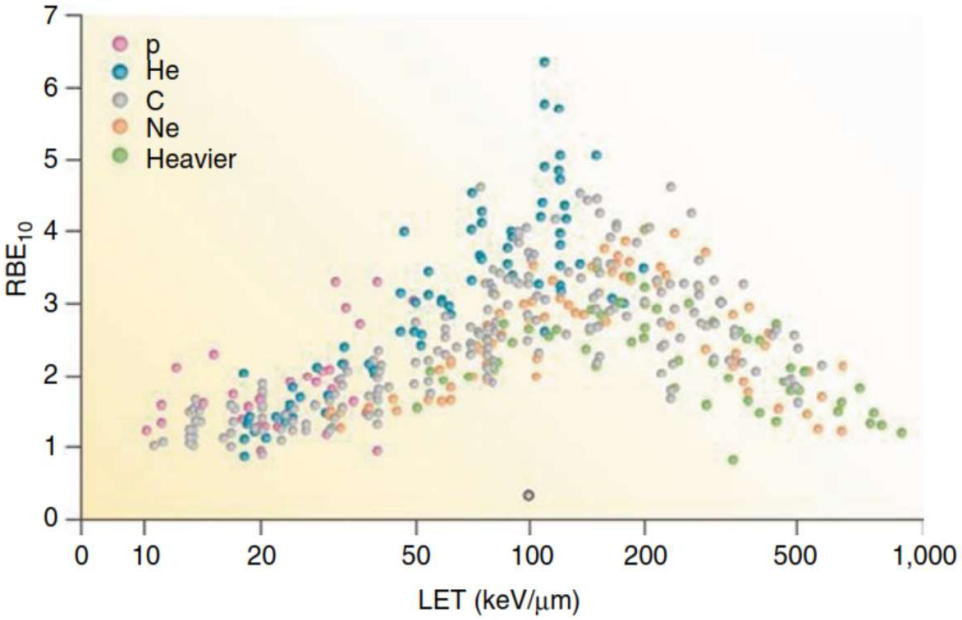

Fig. 31 Compilation of RBE_{10} data for various ions. Data from (Sørensen, Overgaard and Bassler, 2011). Image reproduced from (Loeffler and Durante, 2013).

particles like carbon ions (in this example, the factor is 1:36). This is true only if electromagnetic interactions considered. When considering hadron therapy, especially heavy ions (e.g. Carbon ions), nuclear interactions are critical in the determination of absorbed dose in and out of the field. Other factors like dose dependence (due to fractionation), oxygen enhancement etc. or not discussed in this work.

2.6.9 **Treatment planning for heavy and light ions**

The delivery of the prescribed dose to the target volume with precision and accuracy is possible in modern radiotherapy because of the current state of the art delivery systems that have evolved through technological advancement in science and technology. However, maintaining this level of accuracy and precision across the board using all types of radiation, a thorough understanding and characterisation of the biology that determines the endpoints and results of treatments is needed.

Treatment planning for both heavy and light ions, from a physical perspective, is very similar. The 3D description (modelling) of dose distributions from monoenergetic beams in a water medium use pencil beam models (Krämer and Scholz, 2000; Jäkel *et al.*, 2001). Published depth dose curves are generally

measured or calculated by Monte Carlo calculations. A superposition of Gaussians, used for lateral dose distributions, shows widths that vary with depth. Empirical treatment is employed in the describing of the primary beam width, where multiple scattering and nuclear fragmentation are considered.

As outlined in previous sections, in proton therapy, a fixed value of the RBE is used, while this is not a valid approach for heavy ions. Historically, as long as passive delivery techniques are available, a depth-dependent RBE has been used in Berkeley and Chiba, Japan. This is in contrast to the fixed depth modulation of treatment fields for passive techniques (Rath and Sahoo, 2016).

In the treatment planning of heavy charged particles, two main models are currently in use to take into account the variation of the RBE with depth, including other dependencies: The local effect models (LEM) and the micro-kinetic model (MKM). The LEM model makes the first assumptions that the difference between photons and ions are mainly due to the dose distribution on the microscopic scale (expressed as LET). Therefore, an input parameter to the LEM model (Scholz and Kraft, 1994, 1996; Elsasser and Scholz, 2006; Elsässer and Scholz, 2007) is the detailed modelling of the track structure of ions. Using known damage for photons and transferring this radiobiological experience to ions is the second assumption employed by the LEM model.

The implication is that the LEM model can describe the dependencies of the RBE for ions for different cell types and endpoints because these are known for photons. In this model, α and β values that describe certain cell types and endpoints that are used as inputs. Finally, the composition of the particle spectrum is used for direct integration into a Monte Carlo System. The MKM was introduced for the beam scanning system at HIMAC (Sato *et al.*, 2011) and is based on microdosimetric parameters of ions and in its implementation links microdosimetric parameters to macroscopic parameters like energy and LET in Monte Carlo simulations.

There is still much scope in the development of treatment planning for ion beams that can allow for further optimisation of ion beam therapy. The implementation of RBE in treatment planning systems requires that we appreciate the relationship

between LET, dose, and biological endpoints. The determination of RBE values has long been limited by the significant uncertainties in methods employed in its determination (Paganetti, 2012).

CHAPTER 3: METHODS AND MATERIALS

In this section, the main aspects of the materials and methods employed to conduct the investigations are presented. In some instances, a detailed description is given to provide a transparent description of the locally used methods in both the simulation and analysis processes.

Two approaches were followed in the investigation to map out the radial dependence of nanodosimetric parameters from the proton tracks. In the first approach, the so-called "amorphous approach" was employed and provided reasonable preliminary results for the radial dependence, summarised by the so-called effective track cross-section. Derived models of the calculated effective cross-section along the path length are then used to evaluate the variation of nanodosimetric parameters along the track pathlength. A modified version of the method adopted from the literature (Bortfeld and Schlegel, 1996) for the creation of the spread-out BP is presented. In the second approach, we present a more rigorous analysis of the radial dependence by employing efficient computer methods in the collection of ionisation clusters in the penumbra region to handle the problem of a reduced number of ionisations at large radial distances. The radial limit is also extended to account for ionisation clusters occurring at radial distances larger than 100 nm.

The method to evaluate the dependence of nanodosimetric parameters on the target orientation is given. A scoring method that takes into account clusters from all azimuth angles for the radial distances considered is presented for both the core and penumbra regions.

Modelling of a wall-less target representation of the ion collection efficiency in an ion counter nanodosimeter is presented. This is a novel formalism that provides a transparent dependence of the dosimetric parameters on the gas parameters and the electric field in the ion counter chamber.

3.1 **Variation Of Nanodosimetric Parameters In Proton Tracks – Heuristic Approach**

A detailed investigation of the material and methods used to evaluate the variation of nanodosimetric parameters around a proton track is presented in this section, and part of the work presented in this section has been published in the paper entitled '"*Broadscale" nanodosimetry: Nanodosimetric track structure quantities increase at distal edge of spread-out proton Bragg peaks*' (Rabus *et al.*, 2020).

3.1.1 **Simulation setup**

Simulations of proton tracks in liquid water were performed using the GEANT4-DNA toolkit, which can track step-by-step interactions of particles down to the eV scale (Incerti, Baldacchino, *et al.*, 2010; Incerti, Ivanchenko, *et al.*, 2010; Bernal *et al.*, 2015; Incerti *et al.*, 2018). Version 10.4 patch 01 and 02 of the code were used in combination with the Geant4 physics processes and models for the low energy transport of particles in liquid water. A G4EmDNAPhysics_option2 physics constructor, which uses a set of discrete models for electron transport in liquid water, was also used. Interactions of protons for both electron excitation and ionisation at high energies (>500 eV) were based on the Born and Bethe theories and the dielectric formalism for liquid water. Semiempirical approaches and methods based on the velocity scaling of electron excitation cross-sections were used at low energies (< 500 eV). The protons were started along the *x*-axis at the origin of the coordinate system with a given initial energy.

Three different types of simulations were performed where the results were saved in ROOT (Brun and Rademakers, 1997) data trees. The three simulations were adopted to simulate the proton beam with enough event histories for a statistically sound analysis to address the current evaluation's different aspects. The first simulation is set up to evaluate both the energy and range straggling of the 100 MeV proton beams. A second result from the straggling data is the derivation of the most probable position for different proton energies along a track with a start energy of 100 MeV. The second analysis provides a more rigorous investigation at the end of

the 100 MeV track, and this is meant to map out a more accurate representation of the Bragg peak and fall off regions. The final simulation setup to analyse nanodosimetric parameters at every chosen energy point along the proton track with a start energy of 100 MeV.

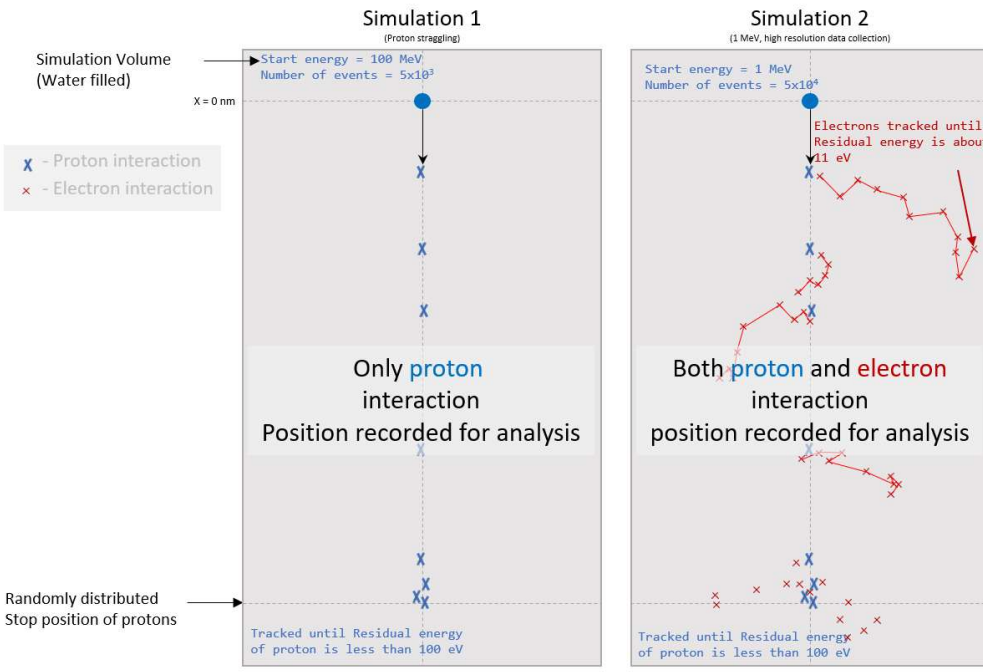

Fig. 33 Graphical representative of the simulation setup showing the projection of a 3D simulation in the (x, y) plane and its parameters for the first two simulations. In the first simulation, only proton track are followed and recorded to calculate proton straggling. In simulation 2, a finer analysis of the track at the energy of 1 MeV is shown. Because of the high ionisation density at the end of a proton track, 1 MeV was choosen to do a more detailed analysis. Fig. 36 shows simulation 3 setup and its parameters.

In the first type, electron transport was disabled, and only the interactions of the proton were tracked. $5x10^3$ protons were propagated in liquid water with start energy equal to the maximum possible value of 100 MeV and tracked until their residual energy was below 100 eV. For each interaction, both the position of the energy transfer point and the proton energy before the interaction were recorded.

In the second type of simulation, $5x10^4$ tracks of protons propagating in water with an initial energy of 1 MeV were simulated until full slow down while tracking both proton and secondary electron interactions. The proton was followed until its energy fell below the threshold of 100 eV, while secondary electrons were tracked until their energy dropped below the ionisation threshold of water (about 11 eV). The position coordinates of all energy depositions resulting from ionising interactions by either the primary particle or any secondary electrons were recorded if they occurred in slabs of 10 nm thickness placed in 500 nm intervals along the proton trajectory.

Fig. 36 depicts the third simulation type. Protons were started in water with initial energies of 2, 3, 4, 5, 10, 15, 20, 25, 30, 35, 40, 50, 60, 70, 80, 90 and 99 MeV, where their tracks were followed over a range of 650 nm and positions as well as energy transfers for each interaction of the proton and any secondary electrons were recorded. In order to obtain reasonable statistics, $5x10^4$ individual tracks were simulated for each energy.

3.1.2 **Track data analysis**

Analysis of the simulation results was performed by post-processing the simulation output files using ad-hoc developed scripts under ROOT (Brun and Rademakers, 1997) and MATLAB (MathWorks, 2019). For analysis of the proton track segments obtained with the second and third kinds of simulation, the frequencies of the number of ionisations were scored in nanometric targets positioned around the proton trajectory. In this study, we consider targets that are either cylindrical in shape with a diameter D of 2.3 nm and a height h of 3.4 nm or that have the shape of cylindrical shell segments of equal volume to the aforementioned cylinders. The use of the latter target shapes is for computational ease (see Section 3.1.1). The cylindrical target shape and size have been used in earlier work to represent a DNA segment of 10 base pairs (Grosswendt, 2005; Garty *et al.*, 2006, 2010; Frauke Alexander *et al.*, 2015).

For the tracks of protons with 1 MeV initial energy, the scoring volumes were placed in planes perpendicular to the proton trajectory at intervals of 500 nm, commencing at 500 nm from the origin of the proton track and concluding at the end of its range.

For the higher energetic protons, the ionisation density was determined in parallel slabs of 10 nm thickness (limiting planes oriented perpendicular to the proton trajectory) at distances between 0 nm and 650 nm from the starting point of the proton, as shown in Fig. 36. Effects from missing electrons produced upstream or downstream of the considered track segment appeared to be absent between 200 nm and 400 nm upstream of the proton's starting point. This is shown by the preliminary qualitative analysis from the scored ionisation densities in the depicted slab, see Fig. 38. Therefore, three scoring planes were put at distances of 200 nm, 300 nm and 400 nm from the starting point. The results from these three planes were then averaged to improve statistics.

Two different scoring geometries were applied for assessing ionisation clusters. In the first scoring geometry, which was used to obtain detailed information within the track core and the inner penumbra regions, cylindrical targets of 2.3 nm diameter and 3.4 nm height were placed in a linear array perpendicular to the proton trajectory. The target cylinders' central axis was oriented perpendicular to both the direction of proton propagation and the line of the shortest distance between the cylinder centre and proton trajectory (see Fig. 40). The radial distances of the target cylinders from the proton trajectory were between 0 nm and 5 nm at 0.2 nm

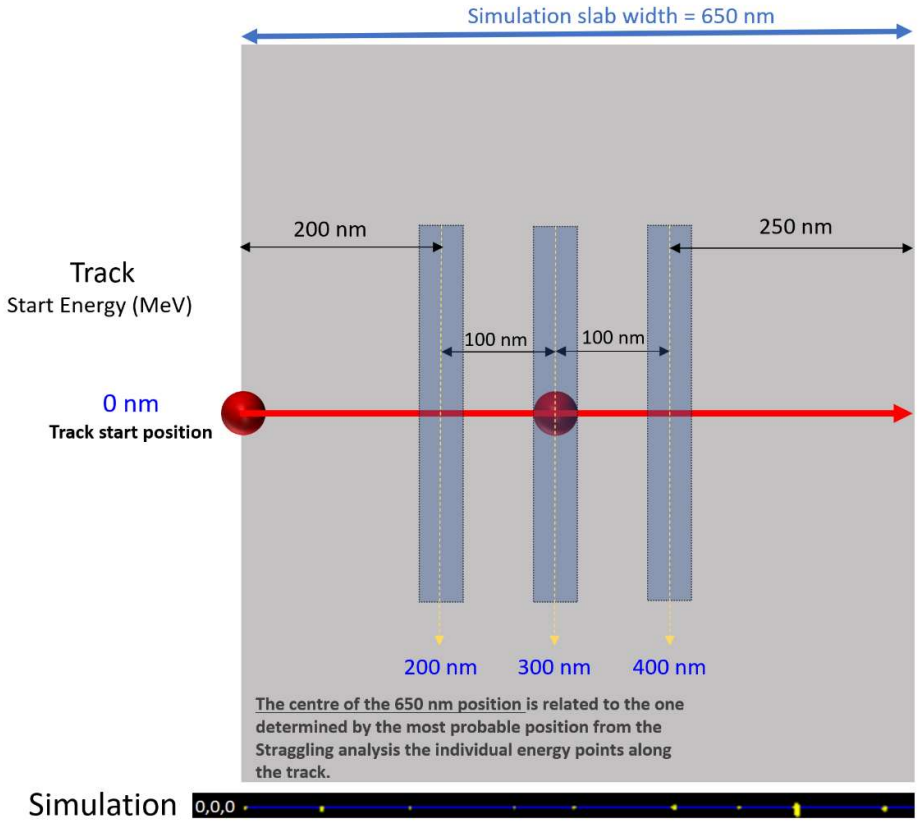

Fig. 35 Illustration of the analysis volume showing the starting position for the simulation at each energy and the three scoring volumes at 200 nm, 300 nm, and 400 nm from the start of the scoring volume. The width of the slab is 650 nm, and the calculation of clusters is done at least 200 nm of the edge of the slab upstream and downstream (250 nm).

intervals. The second scoring geometry was a more CPU time-efficient method used for scoring with better statistics in the outer penumbra region.

A slab centred at the scoring plane position was segmented into a central cylinder and segments of concentric cylindrical shells (whose long axis was orientated along the x-axis) of equal volume (see Fig. 40). The height h_a of these substitute volumes (i.e. slab thickness) was 2.3 nm, which was equal to the diameter of the cylindrical targets used in the first scoring approach. The radii of the inner cylinder and the

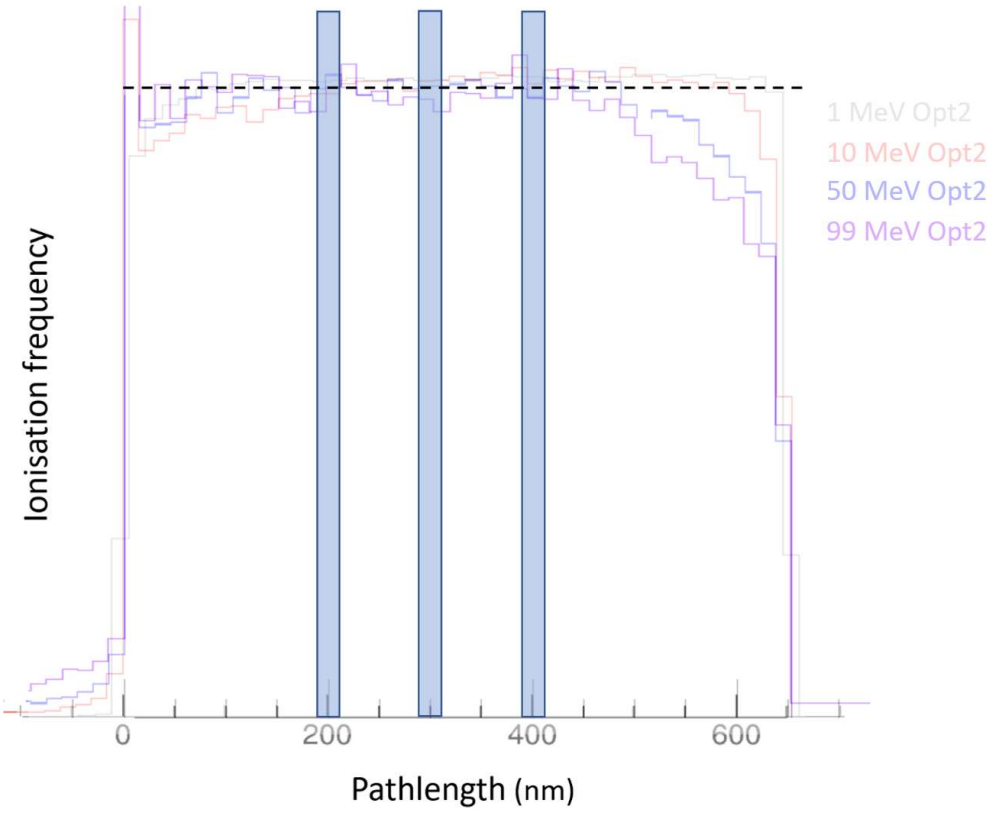

Fig. 37 Geant4-DNA simulation results showing the frequency of ionisations in the analysis slab. The loss of ionisation due to missing electrons from upstream and downstream justifies the selection of scoring slabs is in the 200 nm middle part of the 650 slab.

cylindrical shells were chosen such that each of the 'voxels' had equal volume to the target cylinders in the first approach. To this end, the central cylinder had a radius

r_a of 1.4 nm, and the cylindrical shell segments were given by the following conditions for radial distance r and azimuth angle φ for the k-th segment in the n-th shell:

$$(2n-1)r_a \leq r \leq (2n+1)r_a \quad n = 1,2,\dots,n_{max} \qquad (18)$$

$$(k-1)\frac{\pi}{4n} \leq \varphi \leq k\frac{\pi}{4n} \qquad k = 1,2,\dots,8n \qquad (19)$$

The number of cylindrical shells scored was $n_{max} = 48$, which corresponded to a maximum radial distance of the target from the proton trajectory of 134.4 nm.

The output data files from the track simulations were processed using MATLAB (MathWorks, 2019). The number of ionisations, as well as the energy deposited by ionising interactions within each target volume, was scored track-by-track. For each target, the absolute frequencies of the ionisation cluster size (ICS) were divided by the number of tracks to obtain estimates of the probability distribution $P_\nu(r,x|0,E_0)$for respective x, r and E_0 parameters. The deposited energy in the targets was divided by the target mass to obtain the specific energy contribution due to ionising interactions (z_i). It should be noted that the specific energy z (whose mean value is the absorbed dose) also contains the fraction of the imparted radiation energy that is converted into heat. For the second type of scoring geometry (see Fig. 40), the results for the different targets within a cylinder shell were averaged. From the ICS probability distributions, the mean ionisation cluster size M_1 was calculated together with the complementary cumulative probabilities F_k for a minimum number of k ionisations in a target between 1 and 4.

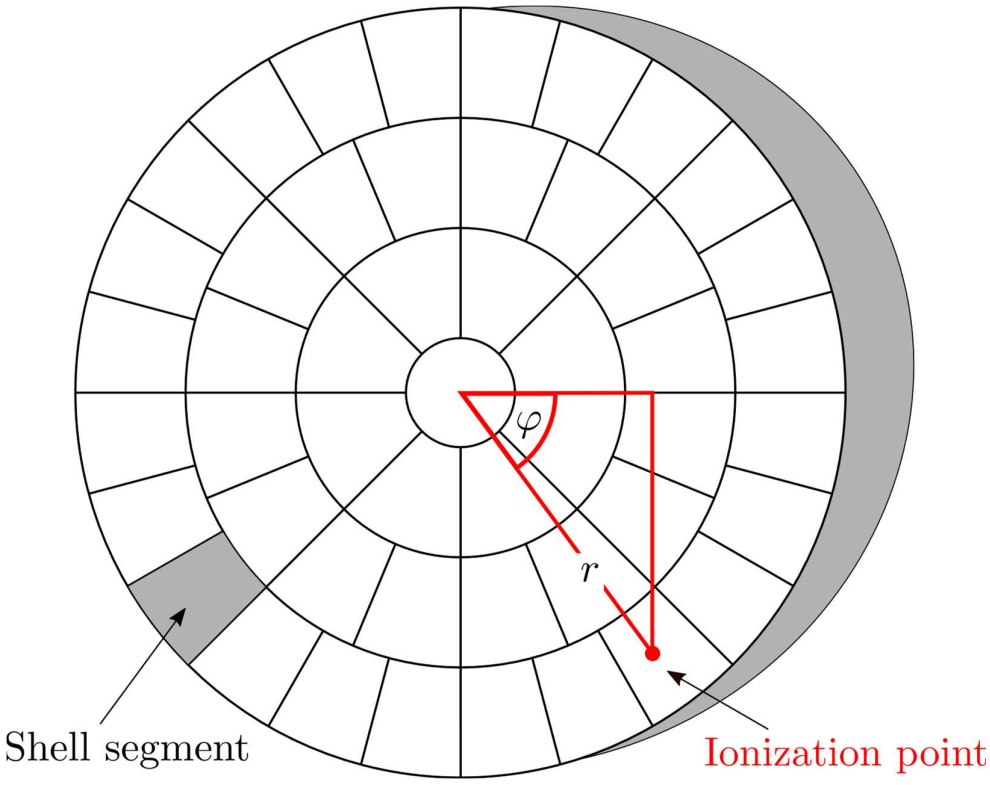

Fig. 39 Illustration of the segmentation of a plane-parallel slab used for scoring with better statistics in the outer penumbra region. All cylinder shell segments have the same volume as the central cylinder.

3.1.3 **Modelling the radial dependence of simulation results**

In a first preliminary analysis of the results from the track simulations, the dependence of the nanodosimetric parameters on the radial distance from the proton trajectory was further analysed by fitting the following data-driven parametric model:

$$y(r, z_j|0, E_i) = \begin{cases} a_y\sqrt{1-t^2} + b_{0,y}t^2 & r \le r_0 \\ b_{1,y}\mathrm{e}^{c_{1,y}(1-t)} & r_0 \le r \le r_1 \\ \mathrm{b}_{2,y}\mathrm{t}^{-\mathrm{c}_{2,y}} & r_1 \le r \le r_2 \end{cases} \qquad (20)$$

Here y denotes any of the scored quantities, that is M_1, F_1, F_2, F_3, F_4 and deposited energy. z_j is the distance from the origin of the plane perpendicular to the proton trajectory in which the centre of each target volume was located for tracks with an

initial energy E_i. The variable $t = r/r_0$ is the radial coordinate normalised to the radius r_0 = 1.15 nm of the target cylinder.

The model parameters depend on both the proton energy and the position along the proton track. However, the respective indices i and j have been omitted for better legibility.

Parameter r_1 in Eq. (20) as set equal to 5 nm (i.e. to the range used in the first scoring geometry). Parameter r_2 was chosen to be 100 nm based on a more rapid fall-off in the data observed at larger radial distances for simulations of protons with 1 MeV initial energy. The rationale for the approach used in Eq. (20) is that the functional shape of $F_k(r)$ should be different depending on whether or not the primary particle traverses the target cylinder. If the proton traverses the target, the ionisations produced in the target are either due to interactions of the proton or secondary electrons.

The mean number of ionisations due to proton interactions should be proportional to the chord length of the proton trajectory within the target cylinder, which is given by the first term in the first line Eq. (20) when the parameter r_0 is the cylinder radius. A quadratic component was added heuristically to consider the contribution of ionisations by electrons. Parameters a_y and $b_{0,y}$ are the function values on the proton trajectory and at the transition point r_0, respectively.

If the proton track passes the target cylinder without intersecting it, all ionisations are due to secondary electrons, and an approximate $1/r^2$ dependence would be expected. This was not confirmed by the data obtained with the first scoring geometry for the region up to 5 nm.

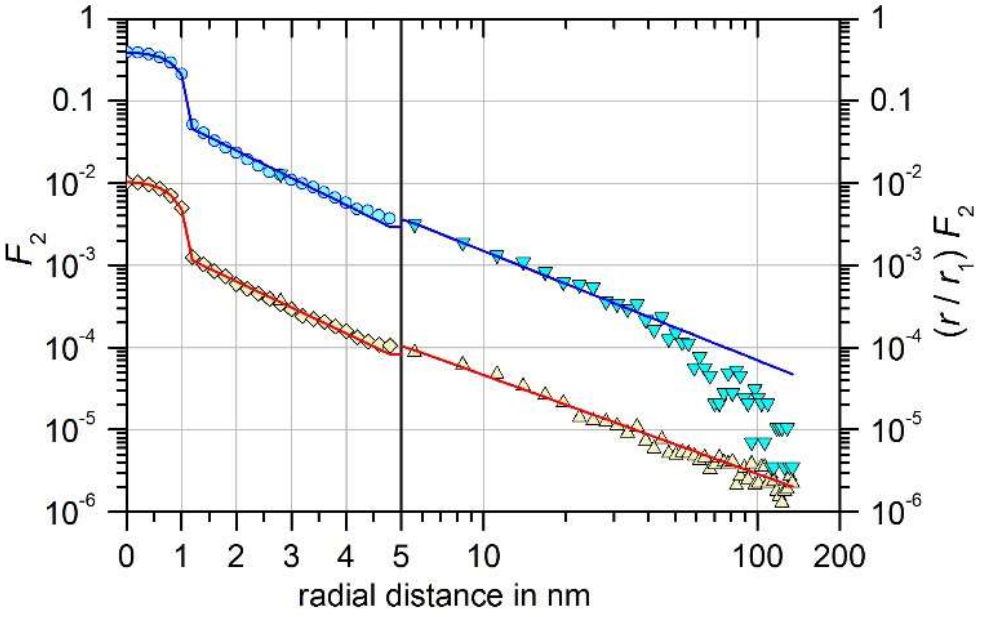

Fig. 41 Probability $F2$ for obtaining inside a nanometric target an ionization cluster of two or more. $F2$ values are shown as a function of the radial distance r from the trajectory of a 50 MeV (red diamonds and upward triangles) and 1 MeV (blue circles and downward triangles) proton in water. The proton tracks were scored with either cylindrical target volumes of 1.15 nm radius and 3.4 nm height (circles, diamonds) or with cylinder shell segments, as illustrated in Fig. 40 (triangles). The lines are the fit curves, according to Eq. (20). On the right-hand side of the figure (i.e. starting from the thick vertical line), the x-axis is logarithmic, and the y values have been multiplied with the ratio of r to r_1 = 5 nm to preserve the slope of the fit

Thus, from the observed dependence on the radial distance (Fig. 42), the exponential approach in the second line of Eq. (20) was used to fit the data. For continuity of the model curve, $b_{0,y}$ and $b_{1,k}$ should be equal. For numerical stability of the fitting routines, however, this constraint was not enforced. Nevertheless, the determined fit values generally agreed within a few percent.

In the outer penumbra, the exponential curve was a poor representation of the data, and consequently, a better fit was determined using the power law given in the third line of Eq. (20) for $r_1 < r < r_2$, as shown in Fig. 42.

3.1.4 **Effective track cross-section (ETCS)**

The radial integrals of the scored quantities (z_i and nanodosimetric parameters) are given by

$$Y_{i,j} = 2\pi \int_0^{r_2} y(r, x_j|0, E_i) r dr \tag{21}$$

For the nanodosimetric parameters, the resulting quantities will be labelled by an asterisk throughout the rest of the thesis (e.g. F_k*). They have the dimension of an area and could be termed 'probability area product'. However, they may also be interpreted as an effective cross-section of the proton track with respect to inducing an ICS with minimum size k in a nanometric target (located in a plane perpendicular to the beam at the respective position x_j along the proton path). For quantity z_i, the resulting integral quantity has the dimension of a dose area product or dose per fluence ratio and is referred to as the area integral of specific energy by ionisations (AISEI) and is denoted by z_i*.

From the model curves given in Eq. (20), the integrals in Eq. (21) are analytically obtained as

$$\begin{aligned} Y_{i,j} = 2\pi \Bigg[& \frac{a_y}{3} + \frac{b_{0,y}}{4} + \frac{1}{c_{1,y}} \left(1 - t_1 e^{c_{1,y}(1-t_1)}\right) \\ & + \frac{1}{{c_{1,y}}^2} \left(1 - e^{c_{1,y}(1-t_1)}\right) \\ & + \frac{{t_2}^{(2-c_{2,y})} - {t_1}^{(2-c_{2,y})}}{2 - c_{2,y}} \Bigg] \end{aligned} \tag{22}$$

where $t_1 = r_1/r_0$ and $t_2 = r_2/r_0$.

3.1.5 **Construction of pristine and spread-out Bragg peaks**

In the case of the simulations for range straggling (first simulation described in Section 3.1.1), the output data were analysed such that the distribution of proton positions was determined for each initial proton energy used in the simulations of

type two and three (described in Section 3.1.1). For each of these energies, and for each simulated proton, the following values were read from the simulation output files: the last position where the proton's energy exceeded the respective energy values (the energy points chosen as described in Section 3.1.1), and the first position where it was below this value. Based on the energies of the proton at these two points, the position where the proton energy would have (in the CSDA applied to this short path segment) the considered energy value was then determined by linear interpolation. From the positions determined for the different tracks for a chosen value of energy, the mean and standard deviation were calculated, and the aforementioned set of position values was binned into 25 equidistant intervals (position bins) between the respective minimum and maximum value. The resulting histogram was then normalised to both the number of proton tracks and the interval width such as to obtain a relative frequency density with an integral value of unity. For each proton energy, the histogram data obtained for the range straggling was fitted with a Gaussian curve, where the mean values from the fits agreed with the mean values obtained directly from the data set to well within the position bin size.

The mean values of the position distributions determined for each proton energy were taken as x-values and the effective beam cross-sections of the different nanodosimetric parameters (F_1* through to F_4*) as well as the AISEI as y values of 'raw' data sets that were used in the following steps described below for constructing the pristine and spread-out Bragg peaks. These data sets also included the additional x positions (in 500 nm steps) where ICS frequencies were sampled from the 1 MeV proton track simulations and the respective y values.

The next step involved analysing the dependence of the y values as a function of the residual range R for the five raw data sets. The residual ranges were calculated as the differences of the mean position for the lowest proton energy (100 eV) and the x values for the other energies considered.

For data points at residual ranges exceeding 5 µm, the data were fitted using a power law

$$y = a\,(R/R_0)^b \tag{23}$$

where a and b are fit parameters and R_0 was chosen as 1 mm.

Practically, the data fitting was done by taking the logarithms of R and y and performing a linear regression with equal weights of all data points. Alternatively, a fit with a polynomial of second order was also investigated, which corresponds to a functional dependence given by:

$$y = a\,(R/R_0)^{b+c\log(R/R_0)} \tag{24}$$

Where log is the natural logarithm and c is a third fit parameter.

Best fit functions were used to interpolate the data sets at x positions between 0 mm and the mean position of 1 MeV protons when calculating the pristine Bragg peaks (PBPs) by numerical convolution with the range straggling distribution. The latter was taken to be a Gaussian distribution found from the range straggling analysis for proton energies up to 35 MeV (cf. section 4.2.2). For numerical convenience, the PBPs were calculated at positions offset from the mean range of 1 MeV protons by integer multiples of 50 µm. The 'raw' data for x values beyond the mean residual range of 1 MeV protons (about 76.3 mm) were included such that the integral, mean and second to fourth central moments of their distribution were calculated and used as weights in a Taylor expansion of the Gaussian (truncated after the fourth-order) to obtain the respective extra contribution to the PBPs.

Finally, SOBPs were constructed following a method described in the literature (Bortfeld and Schlegel, 1996; Jette, David; Chen, 2011), but in a slightly modified version that makes the mathematical notation simpler at the expense of a slight reduction by $1/n$ of the range where the dose profile is flat, where n is the number of PBPs superimposed.

The shifts in the range are then given by

$$\Delta R_k = -\left(k - \frac{1}{2}\right)\frac{W}{n} \tag{25}$$

and the weights of the respective shifted PBPs by

$$w_k = \left(\frac{k}{n}\right)^{1-\frac{1}{p}} - \left(\frac{k-1}{n}\right)^{1-\frac{1}{p}} \tag{26}$$

In Eqs. (25) and (26), W is the width of the SOBP, n is the number of PBPs used, ΔR_k is the shift of the k-th PBP, w_k is the weight associated with this peak and k varies between 1 and n. Parameter p is related to the exponent of the power-law between particle range and energy. Following the approach of (Jette, David; Chen, 2011), we also used parameter p as adjustable such as to create a flat profile for the SOBP of the AISEI. The same value of p was also applied for the nanodosimetric effective beam cross-sections.

3.2 **Detailed Analysis of the Radial Dependence**

In the previous section (3.1), the investigation was done to investigate if nanodosimetric characteristics of the proton track structure qualitatively show a similar variation as radiobiological data of RBE in proton SOBPs. In the current section, a detailed study of radial dependence is done. This work has been published in one of the papers produced from this research (Braunroth *et al.*, 2020).

3.2.1 **Nanodosimetry**

In order to provide parameters characterising the ionisation component of charged particle track structure, nanodosimetry considers the statistical distribution of probabilities P_ν that ionisation clusters of size ν are produced in nanometric target volumes (Rabus, 2020). The ICS is the number of ionisations produced within such a nanometric target by a single charged particle track. As the probabilities for single ionisation and no ionisation are also considered, the normalisation condition given in Eq. (27) applies.

$$\sum_{\nu=0}^{\infty} P_\nu(r, z|E_0) = 1 \tag{27}$$

The probabilities P_ν depend on the target's properties (e.g. geometry and material composition), its radial distance r from the primary track and its position z along the primary particle trajectory (see Fig. 44), and on the primary particle's type and its energy E_0 at a position $z = 0$ along its trajectory. The radial distance r corresponds to the impact parameter of the primary particle trajectory with respect to the target.

The particle track structure can equally be characterised by the moments M_n of the distribution of probabilities P_ν defined in Eq. (28).

$$M_n = \sum_{\nu=0}^{\infty} \nu^n \, P_\nu \tag{28}$$

or by the complementary cumulative distribution of probabilities F_k that at least k ionisations are produced in the target which are related to the probabilities P_ν according to Eq. (29).

$$F_k(r, z|E_0) = \sum_{\nu=k}^{\infty} P_\nu(r, z|E_0) \tag{29}$$

Investigations by Conte et al. (Conte *et al.*, 2017, 2018) indicate that the probabilities F_k are unique functions of the first moment of the probability distribution, i.e. the mean ionisation cluster size M_1. It should be noted that M_1 and the probabilities F_k are related according to Eq. (30).

$$M_1 = \sum_{k=1}^{\infty} F_k \tag{30}$$

Conte et al. further showed that the functional relationships F_k (M_1) mimic the dependence of radiobiological cross-sections for inducing certain endpoints in cell experiments conducted with ion beams (Conte *et al.*, 2017, 2018).

For readers familiar with the concepts of nanodosimetry, it should be clarified that this present work was guided by the paradigm shift in nanodosimetry that was first proposed by Selva et al. (Selva, Conte and Colautti, 2018). The quantities P_ν are

elements of the probability distribution for a stochastic quantity that is the result of the overlay of track structure and target. In conventional nanodosimetry, P_v is the

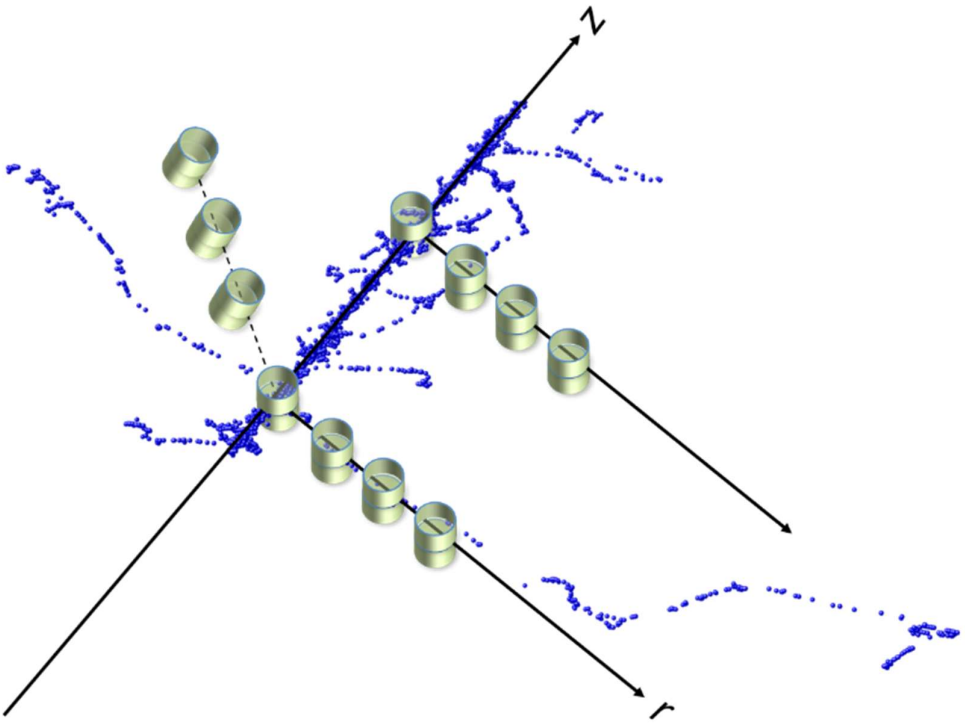

Fig. 43 Illustration of the scoring of ionization clusters produced by a particle track in target cylinders located at different radial distances r from and different positions z along the primary particle trajectory. The symbols indicate the positions of ionizing interactions by the primary particle or its secondary electrons.

probability for finding an ionisation cluster size v in a specific target. However, it can also be interpreted as the probability of finding a target that receives v ionisations.

This latter point of view seems more suited for a comprehensive characterisation of particle tracks (Selva, Conte and Colautti, 2018; Rabus *et al.*, 2020).

Within the frame of this paradigm shift, the quantities P_v are the statistical expectation for the mean relative frequency of targets receiving an ionisation cluster v (and having positions that are characterised by a specific geometrical relation with the particle track, e.g. a certain radial distance from the primary particle trajectory).

The number of such targets found for a particular track is a stochastic quantity, and the track can be characterised by the probability distribution of this stochastic quantity. Or rather, the ensemble of probability distributions for the different geometrical arrangement of the targets (e.g. different impact parameter) and target properties (e.g. target size) is a complete characterisation of the track structure. This was the essence of the multi-scale approach proposed within the BioQuaRT project (Palmans *et al.*, 2015).

However, complete coverage of this subject is beyond the scope of this chapter of the thesis which focuses on presenting an augmented methodology for scoring aforementioned target frequencies from simulated particle tracks and on applying it to particular target size, namely the often used cylindrical targets of 2.3 nm diameter and 3.4 nm height (Grosswendt, 2004, 2005; Gargioni and Grosswendt, 2007; Bueno *et al.*, 2015; Casiraghi and Schulte, 2015; Ramos-Méndez *et al.*, 2018; Dai *et al.*, 2020).

3.2.2 **Simulation data**

The analysis reported in this section used track structure simulation data produced in previous work (Frauke Alexander *et al.*, 2015), and within this work as described in section 3.1.1 (Simulation setup).

In both cases, simulations of proton tracks in liquid water have been performed using the GEANT4-DNA toolkit that can track step-by-step interactions of particles in liquid water down to the eV scale (Incerti, Baldacchino, *et al.*, 2010; Bernal *et al.*, 2015; Incerti *et al.*, 2018). In all simulations, protons were used as primary particles that were started at the origin of the coordinate system with a given initial energy. Apart from the world volume, no specific target geometry was applied in the simulations as the intention was to perform the scoring with different options for the target geometry in a post-processing analysis (cf. Section 3.2.3., "Track data analysis")

Simulations in the heuristic approach were performed with release 10.4 patches 01 and 02 with the Geant4 physics processes and models for transport of low energy

particles in liquid water. The simulation data used in this analysis were obtained using the G4EmDNAPhysics_option2 physics constructor, which uses a set of discrete models for electron transport in liquid water.

Proton tracks were simulated for 25 different values of the initial energy of the protons between 1 MeV and 99 MeV. In this work, mainly results for these two and for 3 MeV, 10 MeV, 25 MeV and 30 MeV are presented. For each initial energy, $5x10^4$ primary particle histories were simulated. The protons were followed over a range of 650 nm along their initial direction of motion. The tracks of secondary electrons were followed inside a 650 nm-thick slab (limited by planes perpendicular to the proton direction of motion and limited by the start and endpoint of the considered proton trajectory segment) until their energies fell below the ionisation threshold of water of about 10.7 eV. For both protons and electrons, the POSTSTEP positions and energy transfers for each ionising interaction were recorded in ROOT (Brun and Rademakers, 1997) data trees.

The simulations of (Frauke Alexander *et al.*, 2015) were performed using Geant4-DNA release 9.6 and applied an energy cut of 7.4 eV for the electron transport, which was considered as the lower limit of the validity range for the elastic electron-scattering cross-sections. Between 50 and 500 tracks per energy were simulated for protons starting from the centre of a 20 µm liquid water cube along the *z*-axis. The initial energies were 3 MeV, 10 MeV, 25 MeV, 50 MeV and 100 MeV, and the protons were followed over 10 µm path length and the secondary electrons until their energy fell below the energy threshold for transport.

3.2.3 **Track data analysis**

The simulated data analysis was performed by scoring the ionisations at specific spatial coordinates (as obtained from the simulations) in specific target volumes to determine the frequency of targets experiencing ionisation clusters of different size (number of ionisations in the targets). This task was accomplished by processing the simulation output files with in-house programs that are described in Chapter 8.

In principle, cylindrical targets (diameter 2.3 nm, height 3.4 nm) were placed at different positions along and at different radial distances from the proton trajectory, as shown in Fig. 44. In contrast to earlier work in section 3.2, we used two mathematical tricks to improve the statistics:

First, as indicated in Fig. 44 and Fig. 46, we scored the ionisations in targets with the same impact parameter but positioned at different azimuth angles around the proton trajectory. In this way, the information contained in the individual tracks is made better use of. (The same could also be achieved by increasing the number of histories at the expense of longer CPU time.)

Second, we exploited the fact that the nanodosimetric probabilities P_ν vary only slowly along the proton trajectory so that their values are essentially equal to the average over a short segment of the track.

$$P_\nu(r, s|E_0) \approx \frac{1}{\Delta s} \int_{s-\Delta s/2}^{s+\Delta s/2} P_\nu(r, z|, E_0)\, dz \qquad (31)$$

This allows for further improvement of statistics by using a discretisation of Eq. (31), i.e. by scoring with target cylinders placed at different (equidistant) positions along the primary particle trajectory and taking the average. The result is an estimate for the probability P_ν at $z = z_0 + s$, which is also an approximation of the probability P_ν at all z values in the interval $[s\text{-}\Delta s/2,\ s\text{+}\Delta s/2]$. It is understood that in the analysis of a simulated track, this interval must be contained entirely in the slab where ionisations were recorded. Furthermore, in the initial part of the volume used for registering ionisations as well as in the region before its distal boundary, interactions are missed that would be present in a real track. Therefore, the scoring of ionisations in the tracks was limited to a 400 nm-thick region (between two planes perpendicular to the proton trajectory) starting at 150 nm downstream from the start point of the protons.

It should be emphasised that in the evaluation of Eq. (31), the step size Δs used in the numerical integration may be chosen smaller than the diameter of the targets. In this way, all ionisation points are captured. This is possible because the quantity to

be calculated (the average number of targets with a certain ionisation cluster size) is a deterministic quantity.

Both aforementioned tricks improve the statistics without the need for increasing the number of primary particle histories because they better exploit the information obtained by the simulation. As is evident from Fig. 44 and Fig. 46, however, obtaining good statistics at large radial distances where only a rapidly decreasing fraction of targets undergo ionisations remains a challenge.

In section 3.1, the first approach was presented to tackle this issue via a complete segmentation of the penumbra region into disjoint cylinder shell segments that had

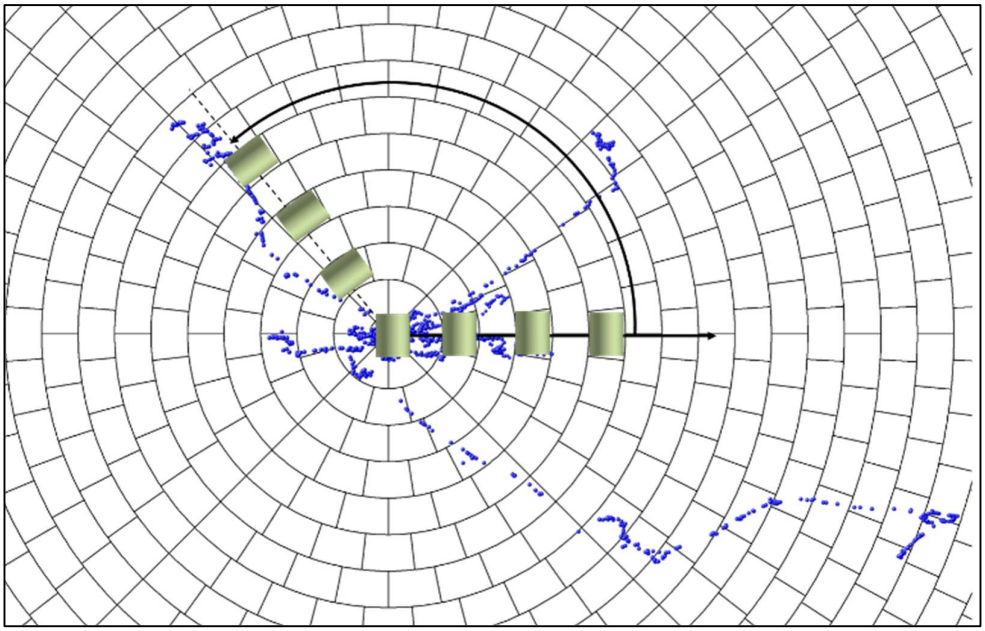

Fig. 45 The same particle track as shown in Fig. 44 seen along the direction of propagation of the primary particle. The grey lines show the cross-sections of cylinder shell segments that are used for a more comprehensive scoring of the penumbra region where most of the cylindrical targets would not encounter ionizations.

the same volume (and the same thickness along the trajectory direction) as the cylindrical targets (Fig. 46). This approach ensured that all ionisations in the covered radial range were taken into account. However, the radial range was limited

to about 100 nm owing to the employed scoring algorithm that was based on checking coincidence with the elements of a set of predefined cylinder shell segments. In the present section, this limitation was overcome by an improved algorithm (see section 8.3) such that all ionisations in the penumbra of the simulated tracks were considered. To compensate for the strongly decreasing frequencies of targets scoring ionisations with increasing radial distance, for radial distances exceeding about 30 nm, an exponentially increasing number of radial shells was merged into larger radial bins procedure used by (Wang and Vassiliev, 2014).

The trade-off for completely scoring all ionisations in the penumbra in a computationally very efficient way is that it requires the use of a target geometry that differs from the cylindrical targets commonly considered in nanodosimetry. It may be expected that the influence of target size will be less significant far away from the particle trajectory. Nevertheless, the question arises from which radial distance the scoring with cylinder shell segments is equivalent to scoring with cylinder targets of the same volume and whether there is a bias due to the fact that the cylinder shell segments are not fully convex or due to the choice of their geometrical dimensions. (The requirements that they have the same volume as the cylinders and that they allow a complete segmentation without overlaps are not imposing a unique choice.)

To address the question of equivalence, the scoring was performed using three different options for defining the cylinder shell segments:

In option 1, the parameters defining the target positions were the same as those used in (see section 8.3), i.e. the extension of the cylinder shells along the z-direction was equal to the diameter of the cylinders (2.30 nm), and the n-th cylinder shell was divided into 8 n azimuthal segments (Fig. 46). This resulted in a radial thickness of the cylinder shells of Δr = 2.80 nm (and an inner cylinder, corresponding to n = 0, with its height along the z-axis and a diameter of 2.8 nm.)

In option 2, the cylinder shell thickness along the z-direction was equal to the mean chord length of the primary particle track through the cylindrical targets, i.e. about 1.80 nm, and the n-th cylinder shell was also divided into 8 n azimuthal segments.

The resulting radial thickness of the cylinder shells (and diameter of the inner cylinder) was $\Delta r = 3.16$ nm.

In option 3, the cylinder shells were divided into 4 *n* segments, and the same value of 2.08 nm was used for radial thickness and thickness along the *z*-axis. The rationale behind this was to have an 'aspect ratio' of the target 'height' (along the azimuth) to the 'diameter' (the radial size) as well as the shape of the 'cross-section' (for fixed azimuth) similar to that of cylindrical targets. In consequence, the inner cylinder (for $n = 0$) had only half the volume of the cylinder segments. This does not cause a problem, as the results obtained from scoring in-cylinder shell segments are only needed in the penumbra region.

To obtain reference data for assessing the equivalence between the different scoring target geometries, for each of the three options scoring was also performed by placing cylindrical targets at the locations of the segments of the first 11 cylinder shells (Fig. 46), i.e. up to radial distances from the proton trajectory of about 30 nm. For detailed determination of the radial dependence close to the primary particle trajectory, cylindrical targets we placed in 0.1 nm steps up to a radial distance of about 10 nm, where 16 equidistant azimuths were used.

From the ICS frequency distributions, the complementary cumulative probabilities F_k for a minimum number of k ionisations in a target between 1 and 4 were calculated and used for the analysis presented in this work. In addition, also the radial integrals defined by Eq. (32) were determined by numerical integration.

$$y_k^{\#}(R, z|E_0) = 2\pi \int_0^R y_k(r, z|E_0)\, r\, dr \qquad (32)$$

In Eq. (32), y_k denotes any of the nanodosimetric quantities F_k ($k = 1, 2, \ldots$), and $y_k^{\#}$ is the respective radial integral up to a radial distance R from the primary particle trajectory.

3.3 Dependence Of Nanodosimetric Parameters On The Target Orientation

3.3.1 Simulation setup

In this investigation, simulations in section 3.1 "Variation Of Nanodosimetric Parameters In Proton Tracks – Heuristic Approach" are used to evaluate the influence of the angular variation of the target cylinder (volume) relative to the protons track. In this investigation, 4000 events were simulated for a 1 MeV proton track.

3.3.2 Track data analysis

The simulation analysis was carried out by scoring ionisation clusters in defining target volumes, as depicted in Fig. 48 below. The scoring slab is defined according to the analysis presented in Fig. 40 for both the core and the penumbra region.

In the current investigation, the target cylinders are rotated (representing the substitute volume) to study the influence of different orientations, but only through such orientations where the impact parameter remains constant. To achieve this goal, the size of the substitute volumes is chosen such that in the penumbra region, a cylinder of height 3.4 nm and diameter 2.3 nm whose centre is coinciding with the centre of the substitute volumes will be completely contained in the substitute volume for any orientation of the cylinder. This condition is fulfilled if the central cylinder has a height $h_b = 4.2$ nm, and a radius $r_b = 2.7$ nm is used.

The cylinder shell segments also have a height $h_b = 4.2$ nm. They are confined by cylindrical boundaries defined in the equation below:

$$radial\ limits = \begin{cases} r_{n_b-} = r_{n_b} - r_b \\ r_{n_b+} = r_{n_b} + r_b \end{cases}, where \tag{33}$$

$$r_{n_b} = 2n_b r_b \tag{34}$$

and n_b is an integer indicating the number of the shell.

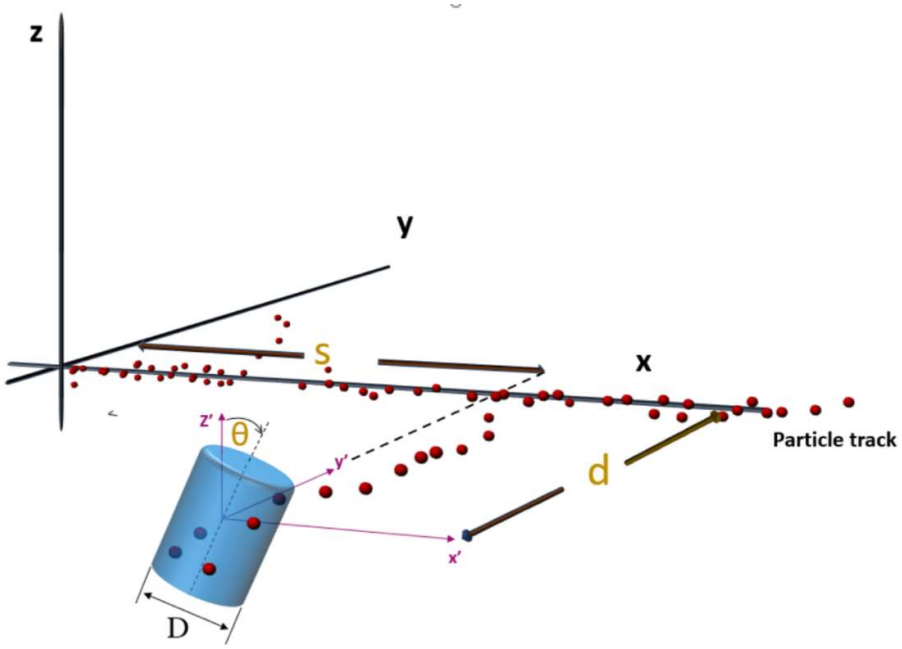

Fig. 47 Angular variation of nanodosimetric parameters. The shown angle was varied using a parameterisation scheme described below.

The azimuthal boundaries of the cylinder segments are given by

$$azimuth\ limits = \begin{cases} \varphi_{k_b-} = \varphi_{k_b} - \dfrac{\pi}{8n_b} \\ \varphi_{k_b+} = \varphi_{k_b} + \dfrac{\pi}{8n_b} \end{cases}, where \qquad (35)$$

$$\varphi_{k_b} = k_b \frac{\pi}{4n_b} + \frac{\pi}{8n_b}, \quad k_b = 0, 1, \ldots, 8n_b - 1 \qquad (36)$$

To calculate the required parameters, which is the ionisation cluster size distribution and ultimately the needed cumulative frequency distribution, say F2, the simulation data is sorted to enable easy and efficient cluster counting. In particular, the data is sorted from the different slabs from the files produced first for ascending track number, then for ascending n_b finally for ascending k_b.

Every ionisation locus is put through a check to determine if it falls within the selected slabs by using the height of the cylinder segment. The condition is determined by the integer value determined by Eq. 37.

$$m_b = \left[\frac{z - z_s}{h_b} + \frac{1}{2}\right] \tag{37}$$

where h_b=4.2 nm, z_s is the centre of the slab, and the square brackets [] means taking the integer of the floating-point number. If $m_b = 0$, this means the ionisation position is within the size of the target in the considered slab; therefore, one has to then calculate the integers given by:

$$n_b = \left[\frac{r}{2r_b} + \frac{1}{2}\right] \tag{38}$$

where r_b=2.7 nm, determining the shells as per the geometric configuration depicted in Fig. 40. If n_b>0, i.e. when the ionization occurs not in the core cylinder, then calculate the parameter depicting the angular position given by:

$$k_b = \left[4n_b \frac{\varphi}{\pi}\right] \tag{39}$$

All the parameters, the numbers n_t (track number), n_b and k_b and the coordinates x, y and z are collected and used in the analysis.

For each radial shell, n_b, the centre of the radial shell is given by:

$$r_c = 2n_b r_b \tag{40}$$

And for each azimuthal position of a target, k_b, the following parameters are defined:

$$c_c = \cos\left(\frac{\pi}{8n_b} \times (1 + 2k_b)\right) \tag{41}$$

$$s_c = \sin\left(\frac{\pi}{8n_b} \times (1 + 2k_b)\right) \tag{42}$$

such that,

$$y_c = r_c c_c \tag{43}$$

$$z_c = r_c s_c \tag{44}$$

are the center coordinates of the target cylinders in a plane perpendicular to the proton trajectory.

To study different cylinder orientations a set of polar angles was used whose cosines and sines are given by:

$$\cos(\theta_k) = 1 - 0.25\ k, \tag{45}$$

$$\sin(\theta_k) = \sqrt{1 - [\cos(\theta_k)]^2} \tag{46}$$

Where $k = 0, 1, \ldots, 7$.

The condition to count ionisations in the rotating cylinder is given in the equation below:

$$\begin{aligned} -1.7\ \text{nm} \leq (x - x_s)\ \cos(k) + (z - z_c)\ \sin(k) \\ \leq 1.7\ \text{nm} \end{aligned} \tag{47}$$

$$\begin{aligned} \left(y - y_c\right)^2 + \left((x - x_s)\ \cos(k) - (z - z_c)\ \sin(k)\right)^2 \\ \leq 1.3225\ \text{nm}^2. \end{aligned} \tag{48}$$

For each radial target position considered, the counted number of ionisations is scaled by $\frac{1}{8n_b}$. Finally, after processing all the tracks, each element of the ionisation cluster distribution calculated is divided by the number of tracks to obtain the relative frequencies $P_\nu(n_b, k)$ of cluster size ν in the n_b-th radial shell around the proton trajectory and for the k-th orientation.

3.4 **Ion Collection Efficiency in the PTB Nanodosimeter**

3.4.1 **Introduction**

The Ion Counter nanodosimeter, developed initially by Garty et al. (Garty *et al.*, 2002), is shown schematically in Fig. 44. The evacuated interaction volume features two parallel circular-plate electrodes A and C, separated by a distance of 5 cm, confine an interaction region B which is filled with a dilute gas (e.g. propane or nitrogen) at low pressure, in the order of 100 Pa. The selection of parameters like the gas type, its pressure and the voltage is such that the defined target volume would be equivalent to condensed liquid water volumes simulating short segments of the DNA. As such, a voltage of 300 V is applied between the plates so that the electrical field drifts electrons and positive ions, produced by charged particles interactions, to the anode A and cathode C, respectively. In practice, the rate of traversing primary particles (trajectory indicated by dashed line I) is kept low

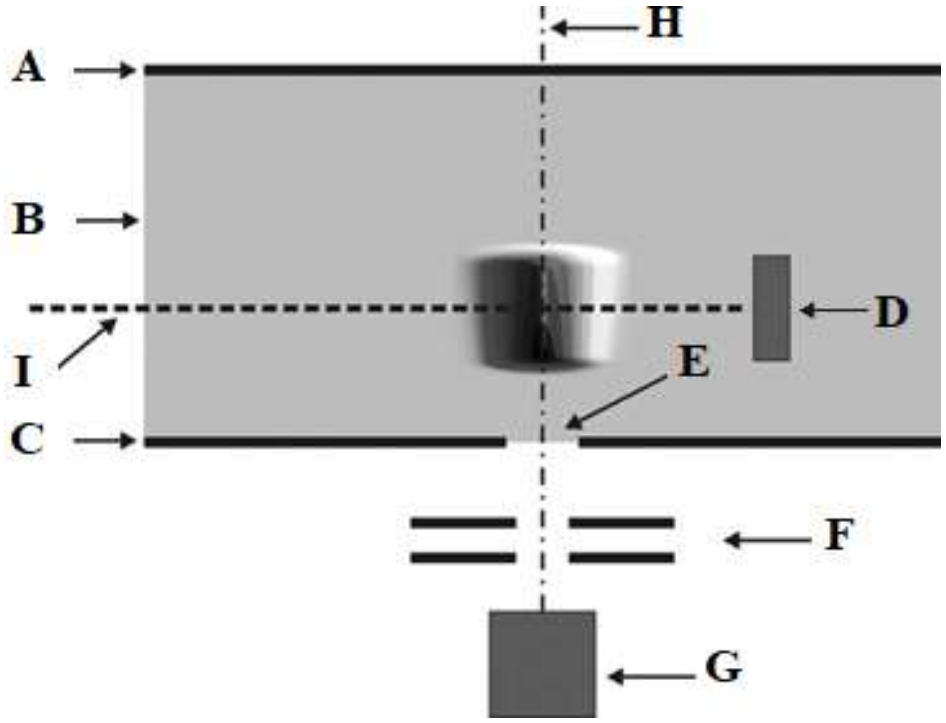

Fig. 49: Schematic cross-sectional side view of the PTB ion counter nanodosimeter (Rabus *et al.*, 2019). Indicate the z axis on the drawing as well as the plate separation of 5 cm.

enough so that all secondary ions produced within one primary particle track are removed from the interaction region B before the next particle arrives.

Positive ions passing through a circular orifice (E) of diameter 1 mm in the centre of the cathode are accelerated under the influence of a high voltage of 8 kV and guided by an ion optics F to an ion counter G where they are registered. In the data analysis, only cations arriving at G within a predetermined time after the solid-state detector, labelled D have detected the primary particle, are counted.

The probability η for an individual cation produced between the plates A and C to contribute to the measured ionisation cluster size is as a function of the location at which the ion is created and is therefore called efficiency map (Garty *et al.*, 2002; Hilgers *et al.*, 2015).

The geometry of the experimental setup is rotationally symmetrical around the axis H passing through the centre of the extraction aperture E. Therefore, the resulting efficiency map can be assumed to be a function $\eta(z,r)$ of the cylinder coordinates z and r if H is chosen as the z-axis.

The function values of the probability $\eta(z,r)$ depend on the size of the extraction aperture E, the shape of the electrical field lines between electrodes A and C and the chosen time window. They furthermore depend on the type of gas and the number density of gas molecules in the interaction region. Fig. 52 shows examples of efficiency maps obtained by simulations based on SIMION (*SIMION*, 2018) with an extension by a user code to account for collisions with the gas molecules in the interaction region B. For the Ion Counter nanodosimeter, the efficiency map was initially evaluated by the developers at the Weizmann Institute (Garty *et al.*, 2002) and further validated later on by simulations and experiments with proton beams performed at the Loma Linda proton therapy centre (Schulte *et al.*, 2006).

3.4.2 **Definition of the effective target in the measurements**

To relate the nanodosimetric measurement to the conceptual approach based on cylindrical target geometry, an effective target should be defined as a cylindrical volume that is 'equivalent' to the efficiency map. While it is evident that the cylinder

centre should be given by the centre of gravity of the efficiency distribution, the choice of the cylinder dimensions is not as straightforward. Using the diameter and height of a cylinder that best approximates the contour surfaces at 50% or another percentage of the maximum efficiency would be possible. As this would be mathematically very intricate, a different approach is suggested here, where analogues of the moments of inertia of the efficiency distribution are considered. Defining

$$V_\eta = 2\pi \iint \eta(r,z) r dr dz \tag{49}$$

The z coordinate of the centre of gravity, z_t, is given by

$$z_t = 2\pi \iint z\eta(r,z) r dr dz / V_\eta \tag{50}$$

Demanding that a cylinder of radius r_t and height h_t centred at the point (0,0, z_t) with uniform 'density' η_t has the same expectation values for r^2 and $(z - z_t)^2$ as are obtained from the efficiency map, gives the following values for r_t and h_t:

$$r_t = \sqrt{4\pi \iint r^2 \eta(r,z) r dr dz / V_\eta} \tag{51}$$

$$h_t = \sqrt{4\pi \iint (z - z_t)^2 \eta(r,z) r dr dz / V_\eta} \tag{52}$$

3.4.3 **The simulated nanometric target**

Ionisation cluster size distributions in the gas target of a nanodosimeter are equivalent to those obtained in a nanometric target in water.

The basis for this is a density scaling principle for the mean ionisation cluster size. As was shown by Grosswendt (Grosswendt *et al.*, 2004) in a Monte Carlo simulation study, the mean ionisation cluster size M1 is approximately proportional

to the mean number of ionisations of the primary ion within the target volume. For the central passage of the primary particle through a target cylinder perpendicular to the cylinder's axis, the scaling principle is contained in the relation

$$M_1 = D_{cyl}/\lambda_{ion} \qquad (53)$$

where D_{cyl} is the cylinder diameter and λ_{ion} is the mean free path for ionisation of the target molecules by interactions of the primary ion. The simulated target cylinder size that corresponds to the effective target defined by Eqs. (3) and (4) is obtained from Equation (5) as:

$$r_s = r_t \times f_s(p_g, T_g;\ E_p), \quad h_s = h_t \times f_s(p_g, T_g;\ E_p) \qquad (54)$$

The scaling factor f_s depends on the pressure p_g and temperature T_g of the gas in the nanodosimeter and on the energy E_p of the primary particle according to

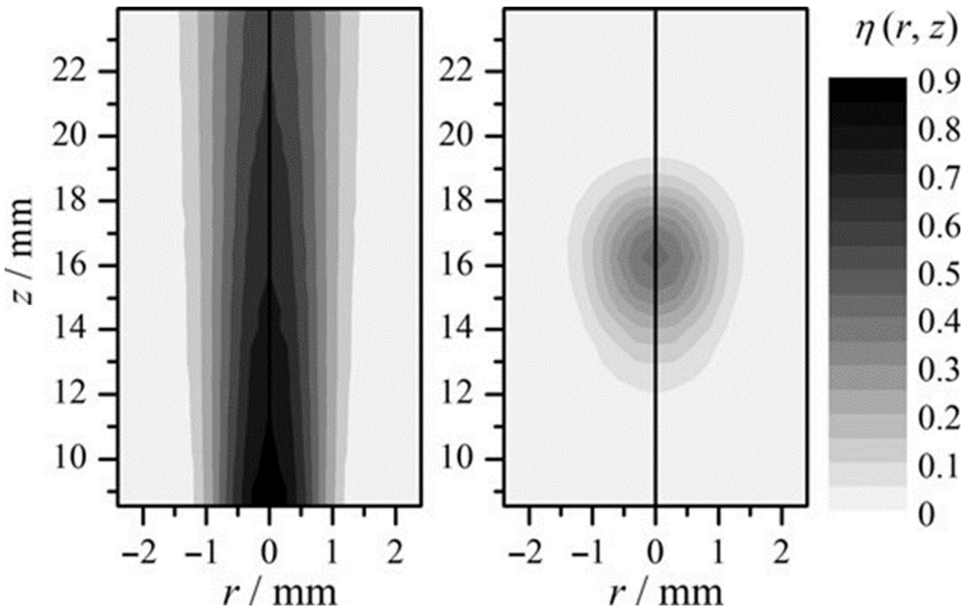

Fig. 51: Efficiency maps for the operation of the PTB nanodosimeter with propane at a pressure of 120 Pa for the case of time windows for secondary ion collection between 0 µs and 150 µs (left) and between 30.5 µs and 35.5 µs (right) (Rabus *et al.*, 2019).

$$f_s(p_g, T_g;\ E_p) = \frac{P_g}{n_w k_B T_g} \times \frac{\sigma_{i,g}}{\sigma_{i,w}} \qquad (55)$$

Here, $k_B = 1.38 \times 10^{-23}$ J/K is Boltzmann's constant and $n_w = 3.33 \times 10^{22}$ cm^{-3} is the number density of molecules in liquid water (at 25°C). $\sigma_{i,g}$ and $\sigma_{i,w}$ are the total ionisation cross-sections of the gas in the nanodosimeter and of water, respectively, which both depend on the primary particle energy E_p. As total ionisation cross-sections of different materials can be well approximated by scaling with the ratio of the numbers of valence electrons (Itoh *et al.*, 2013), the dependence of the scaling factor on primary particle energy can be expected to be small.

3.4.4 **Modelling the collection efficiency**

The simulated target size, according to Eq. (54) depends explicitly on the nanodosimeter's operating parameters p_g and T_g via Eq. (55) and also implicitly through the dependence of the efficiency map on the number density of gas molecules. To make this dependence more transparent, an attempt is made to obtain an approximate analytical representation of the efficiency map based on the following considerations.

The motion of the cations in the interaction region B is governed by collisions of the ions with neutral gas molecules and can be described as the superposition of the drift by the electric field and thermal diffusion. This leads to the following differential equation for the probability ρ that an ion located at point $\boldsymbol{r} = (x,y,z)$ at time 0 s is found at time t at point $\boldsymbol{r'} = (x',y',z')$:

$$D\Delta\rho - (v_d/E)\boldsymbol{E}.\nabla\rho - \frac{\partial\rho}{\partial t} = 0 \qquad (56)$$

D is the diffusion constant, v_d is the magnitude of the drift velocity, $\boldsymbol{E}$ and E are the electric field vector, and its magnitude ∇ is the gradient, and Δ is the Laplace operator. The probability for detection of an ion produced at position $\boldsymbol{r}$ is then obtained by calculating the integral of the perpendicular component j_z of the transport current $\boldsymbol{j}$ defined by

$$\boldsymbol{j} = -D\Delta\rho + \boldsymbol{v_d}\rho \tag{57}$$

over the area of the extraction aperture and over the chosen time window between t_1 and t_2.

$$\eta(r,z) = -\eta_m \int_{t_1}^{t_2} \oiint_{A_E} j_z(x',y',0,t)\, dx'dy'\, dt \tag{58}$$

Here, $\eta_m < 1$ is the probability that cations passing the extraction aperture E are registered. The coordinate origin is in the cathode plane (i.e. $z = 0$) and the minus sign indicates that z-axis points towards the anode A.

If the approximation is made that the disturbances of the electric field near the extraction aperture E and at the outer edges of the electrodes can be neglected, the equation of motion simplifies to

$$D\Delta\rho + v_d \frac{\partial\rho}{\partial z} - \frac{\partial\rho}{\partial t} = 0 \tag{59}$$

where the change of sign in front of v_d is due to the z-axis pointing opposite to the electric field direction. In the absence of electrodes, the solution of this differential equation that satisfies the initial value condition $\rho(r',t = 0)$ is given by

$$\rho(r',t) = (4\pi Dt)^{-3/2} exp\left(-\frac{(x'-x)^2 + (y'-y)^2 + (z'-z+v_d t)^2}{4Dt}\right) \tag{60}$$

This is the solution of Eq. (59) for the case that a single ion is produced at time $t = 0$ s at position $\boldsymbol{r}$.

If the additional simplifying assumption is made that the function defined in Eq. (60) can be used as an approximate solution of Eq. (59) in the presence of the electrodes, the efficiency map is obtained as:

$$\eta(r,z) = -\eta_m \int_{t1}^{t2} \frac{z + v_d t}{2t\sqrt{4\pi D t}} \times exp\left(-\frac{(z - v_d t)^2}{4Dt}\right) I_E(t) dt \quad (61)$$

$$I_E = \iint_{A_E} \frac{1}{4\pi D t} exp\left(-\frac{(x - x')^2 (y - y')^2}{4\pi D t}\right) dx' dy' \quad (62)$$

While the integral in Eq. (62) can be solved analytically, Eq. (61) requires numerical integration. However, the evaluation of Eq. (49) through (52) for the efficiency map given by Eq. (61) and (62) can still be achieved analytically and gives the following results:

$$V_\eta = \eta_m v_d \Delta t {r_E}^2 \pi z_t = v_d t_c \quad (63)$$

$$r_t = \sqrt{{r_E}^2 + 8Dt_c} \quad h_t = \sqrt{(v_d \Delta t)^2 + 24Dt_c} \quad (64)$$

Here, $\Delta t = (t_2 - t_1)$ is the width and $t_c = (t_1 + t_2)/2$ is the centre of the drift time window, and r_E is the radius of the extraction aperture.

CHAPTER 4: RESULTS AND DISCUSSION

4.1 **Ionisation Cluster Size Distributions Of Proton Tracks**

The relative ionisation cluster size distributions were derived from the heuristic investigation for 1 MeV protons. The results below are derived from the track core and are calculated at various distances along the track.

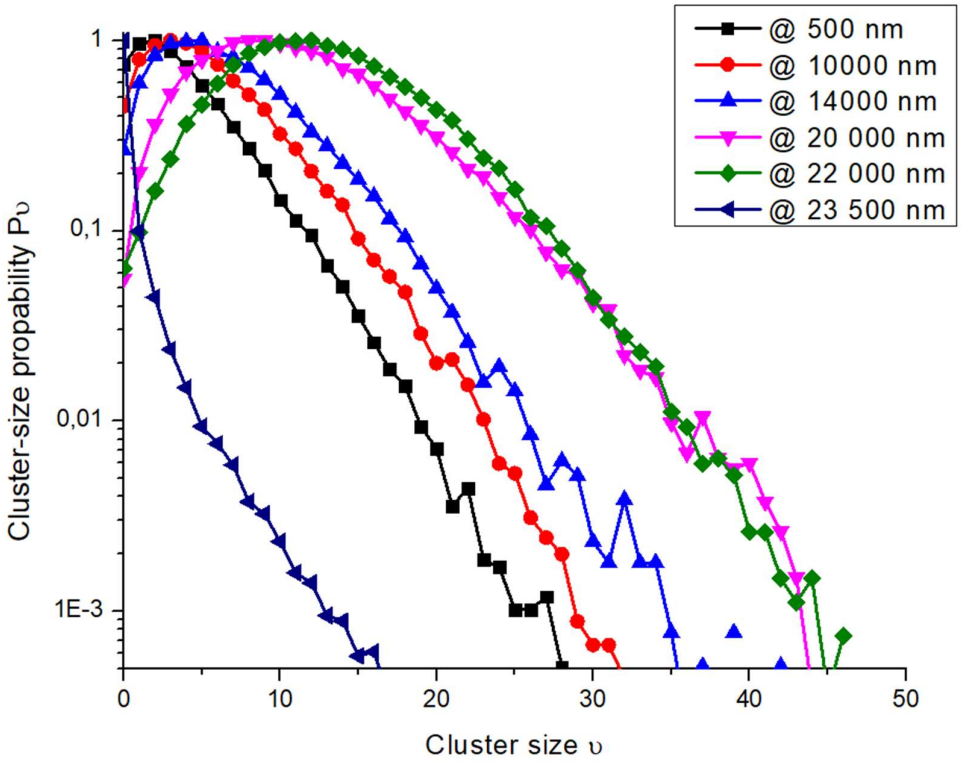

Fig. 53: Ionisation cluster-size distribution along the proton track of energy 1 MeV. The calculated clusters are taken at selected different pathlengths from 500 nm to 23500 nm.

As shown in Fig. 54, as the proton particle loses energy, as it traverses the medium, more ionisations per pathlength result and thus, the mean cluster size increases. At a pathlength of 500 nm, the mean cluster size is 2, and it increases to 3 at about 10000 nm, it is around 9 at 20 000 nm and rises to a maximum around 22 000 nm from the start of the 1MeV track. The result in Fig. 54 shows that the fact that complex clusters are formed as the proton losses energy, which suggests that the

radiobiological effectiveness of the particles increases towards the end of its track. At the peak of the BP, the biological effectiveness reaches its maximum. The cluster size at the distal falloff reduces to a mean cluster size distribution of 0, indicating that the probability of DNA damage at the end of the track quickly drops to zero beyond the range of the proton track.

Fig. 56 shows how the ICSD varies with the radial distance and at pathlengths before the BP region. Clearly visible is the increased cluster size probability with pathlength, especially for cluster size distribution at r = 0.0 nm. The likelihood of getting a cluster size of 0 decreases at one moves from 500 nm to 14000 nm. This is because the 1 MeV proton particle loses its energy, and at 14000 nm it has relatively low energy and a high probability to form clusters. For radial distances in the penumbra region, in this case at 5.4 nm and higher, the most probable cluster size, υ, is zero. In the penumbra region, secondary electrons can form cluster sizes of up to 15.

For pathlengths around the BP as shown in the probability for cluster size distribution, Fig. 58, the probability of larger cluster sizes (compared to those in Fig. 58) increases until the BP, and it then decreases, as shown in Fig. 58 (c). The most probable ionisation cluster size in the core region increases from 2, at 500 nm, to about 9 in the BP, as stated above. At the end of the track, Fig. 58 (c), the ICSD curves at higher radial distances are not shown because of the relatively small range of secondary electrons, because of their low energy, resulting in an exponential reduction of the probability to created ionisation cluster sizes greater than zero. At the end of the track, for the core regions, r = 0.0 nm, the most probable cluster size is zero, Fig. 58 (c).

The increasing probability of complex cluster sizes near the BP indicates that as the proton loses energy and delivers most of its energy at the end of its track, the maximum of its energy is delivered at the BP, also the biological effectiveness of the proton track increases, and falls drastically until the end of the range for the proton.

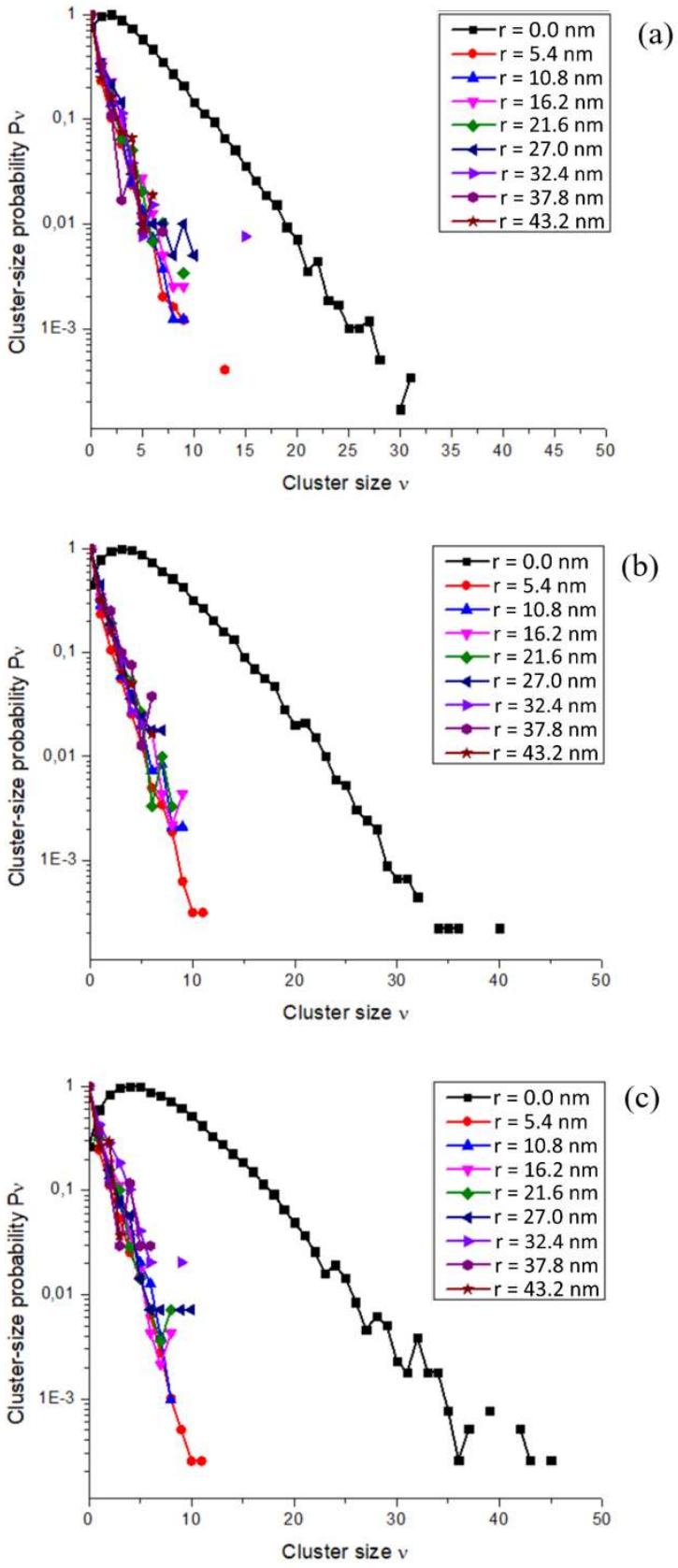

Fig. 55: Ionisation cluster-size distibution variation with radial distance, r, before the BP. (a) @ 500 nm, @ 10000 nm, and @ 14000 nm.

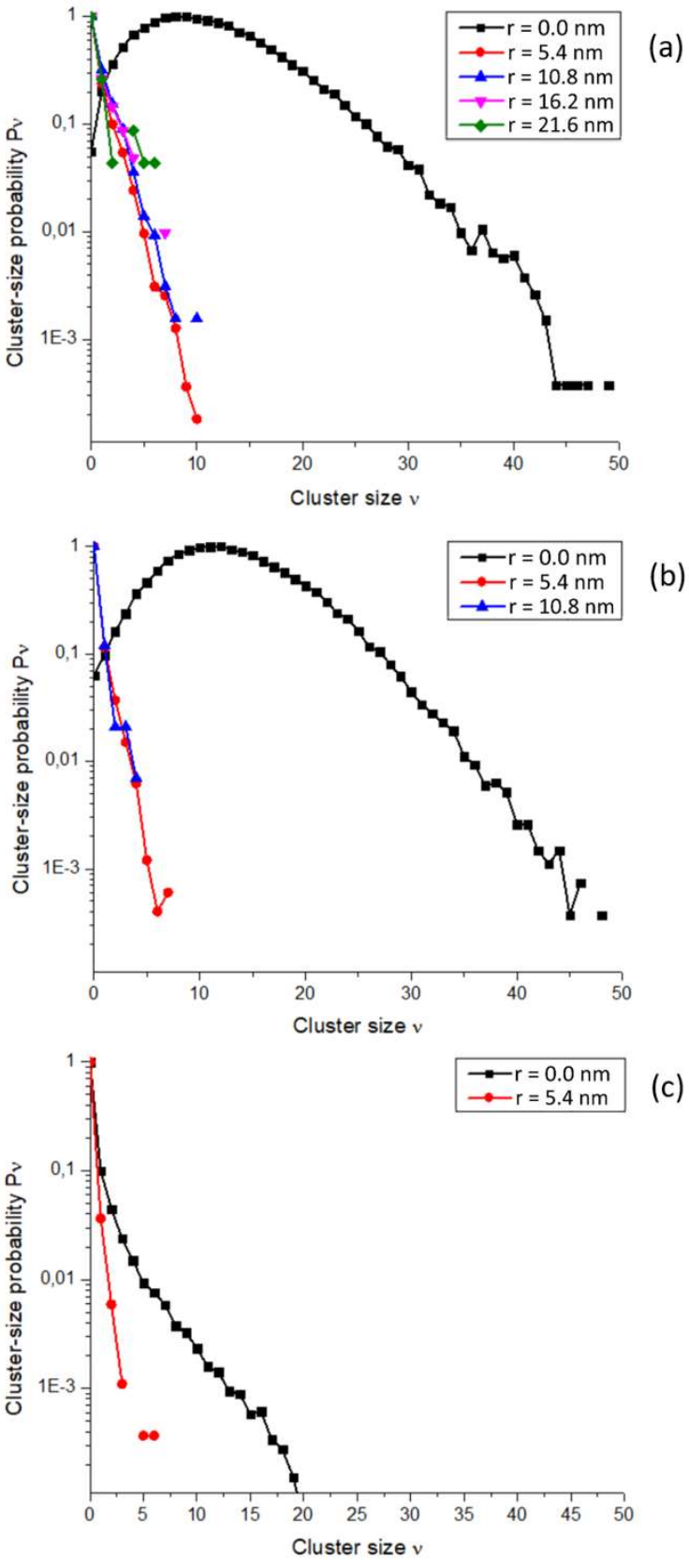

Fig. 57: Ionisation cluster-size distibution variation with radial distance, r, around the BP. (a) @ 20000 nm, @ 22000 nm, and @ 23000 nm.

4.2 Variation Of Nanodosimetric Parameters In Proton Tracks – Heuristic Approach

4.2.1 Introduction

4.2.2 Energy dependence of range straggling

The results for range straggling of the protons are presented in Fig. 30. The upper panel (a) shows the standard deviation of the position distribution as a function of the mean for the different energy values considered, and as indicated by the black dashed and solid blue curves, the position straggling exhibits saturation for energies below 35 MeV. This saturation is due to the broadening of the distribution from the increasing number of interactions, which is counteracted by the rise of the stopping power towards the end of the proton's path, thus resulting in a decrease in the spread of positions.

Fig. 60 (b) shows the relative frequency density in the deviation of the proton position from the mean position observed for the different energies. The solid line is a Gaussian function centred at 0 mm with a standard deviation given by the saturation value observed in Fig. 60 (a), and this curve represents a good fit for the data in Fig. 60 (b). As indicated in section 3.1.5, a Gaussian of this width was therefore used to consider position straggling along the full path of the proton beam in order to get the PBP. Even though position straggling is smaller for residual energies higher than 35 MeV, the area integral of deposited energy and the effective cross-sections of the nanodosimetric parameters at positions less than 65 mm (corresponding to the mean position for 35 MeV) can be approximated by a linear function at the ± 2.5 mm (or smaller).

interval around the mean position. Hence, convolution with a Gaussian of fixed width will not significantly change the values in the entrance region of the PBPs.

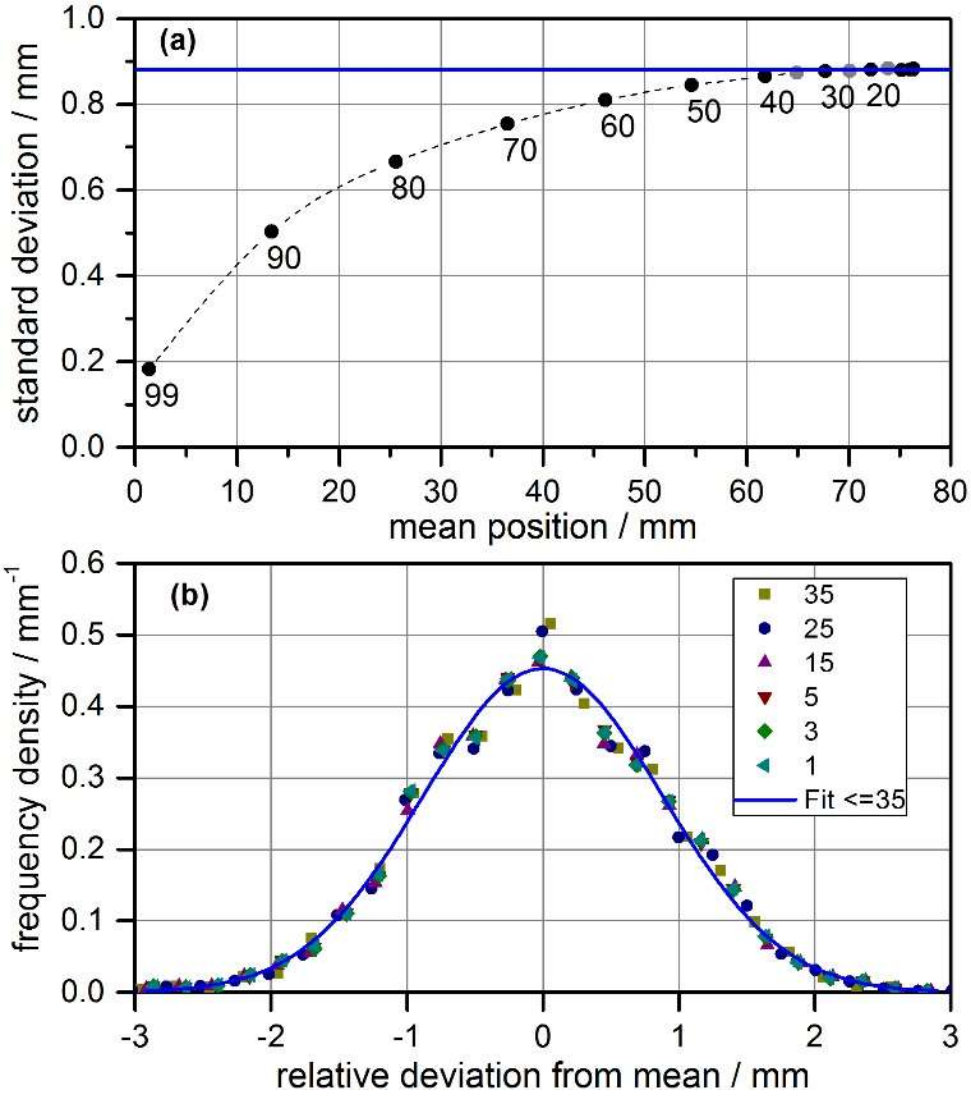

Fig. 59: (a) Range straggling of the path travelled in water by protons with 100 MeV initial energy until their remaining energy takes the value shown as labels to the data points (black circles). The x axis is the mean path travelled and the y axis shows the standard deviation of the position distribution obtained by simulating 5000 proton tracks. The dashed line is a guide to the eye. (b) Sample frequency density distributions of the relative position of the protons for residual proton energies between 1 MeV and 35 MeV (symbols) along with the Gaussian fit curve applying to all data sets (line).

Fig. 62 shows a comparison of the energy dependence of the mean residual range of the protons as a function of their kinetic energy, which was obtained from the analysis described in section 3.1.5 using data for the CSDA range taken from the pstar database (Berger *et al.*, 2005). (The CSDA range from the pstar database shows only negligible deviation from the projected range in the energy interval shown.)

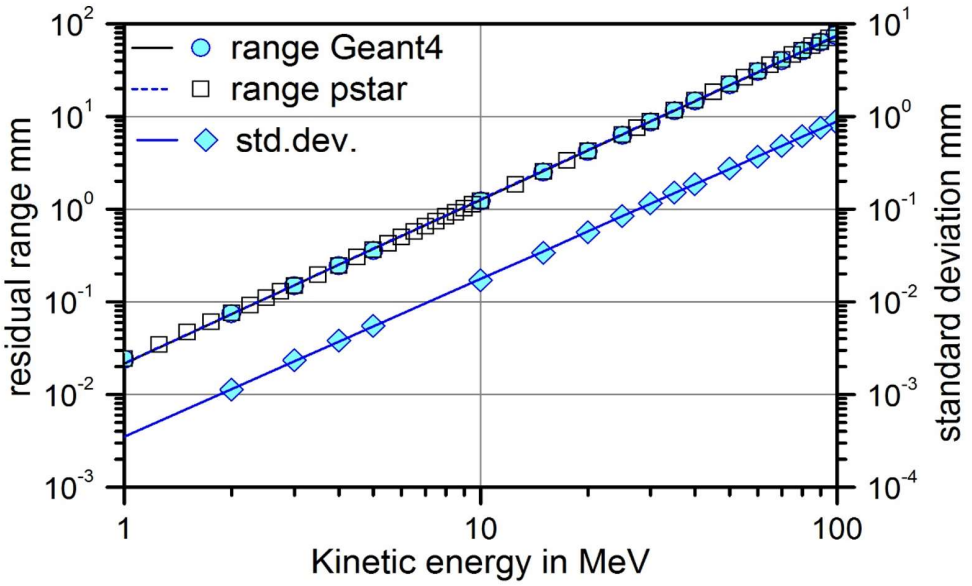

Fig. 61: Mean residual range of the protons versus their kinetic energy as obtained by the present Geant4 simulations (blue circles) compared to data (squares) from the NIST pstar database (Berger *et al.*, 2005). The (coincident) solid black and dashed blue lines indicate the respective best fit with a power function. The blue diamonds indicate the standard deviation of the range travelled by a proton when slowing down to 1 MeV from the energy given on the *x* axis (refers to right-hand side *y* axis).

Both data sets have been fitted with a power function (lines), where the exponents were determined to be 1.767(6) and 1.769(4), i.e. in good agreement with each other. The diamonds indicate standard deviations of the distribution for the distance travelled by a proton of the energy given on the *x*-axis until its energy is reduced to 1 MeV. The solid blue line is the respective fit to a power function, wherein this case the exponent is 1.700(4), which is significantly smaller than that for the range as a function of energy. The fitted power-law curves can be used to extrapolate the

range and the width of the position distribution in the case of an initial proton energy other than 100 MeV.

4.2.3 **Range dependence of radial integrals**

Fig. 64 shows the data sets obtained by combining the mean residual range for a particular proton energy (as shown in Fig. 62) with the results of the radial integrals, according to Eq. (22) for the AISEI and the cumulative probability for two or more ionisations in the nanometric target.

The results of the best-fit curves to the data points for ranges of 5 µm or greater (indicated by the larger symbols) to Eqs. (23) and (24) are also shown. In the case of the AISEI, the simple power law is a good description of the data, and the second-order polynomial coincides with the straight line in the log-log plot of Fig. 64(a).

For the effective cross-section, F_2*, shown in Fig. 64(b), there are significant deviations from the power-law (dashed), and the data are better fitted according to Eq. (24). As indicated by the dotted line in Fig. 64(b), the nanodosimetric data at large ranges can also be reasonably reproduced with a power-law function that has the same exponent as found for the AISEI data (-0.477). This finding means that the nanodosimetric parameters are more enhanced in the region of the maximum compared to the AISEI. It should be noted, however, that the exponent for the AISEI is smaller than the inverse of the slope in the log-log plots of Fig. 62, which amounts to 0.565.

The results for the PBPs obtained by convoluting the raw data of the radially integrated cumulative frequencies with the Gaussian position straggling distribution are shown in Fig. 66(a). For all four nanodosimetric parameters, F_1* to F_4*, the effective track cross-sections are below 1 nm² even in the peak area.

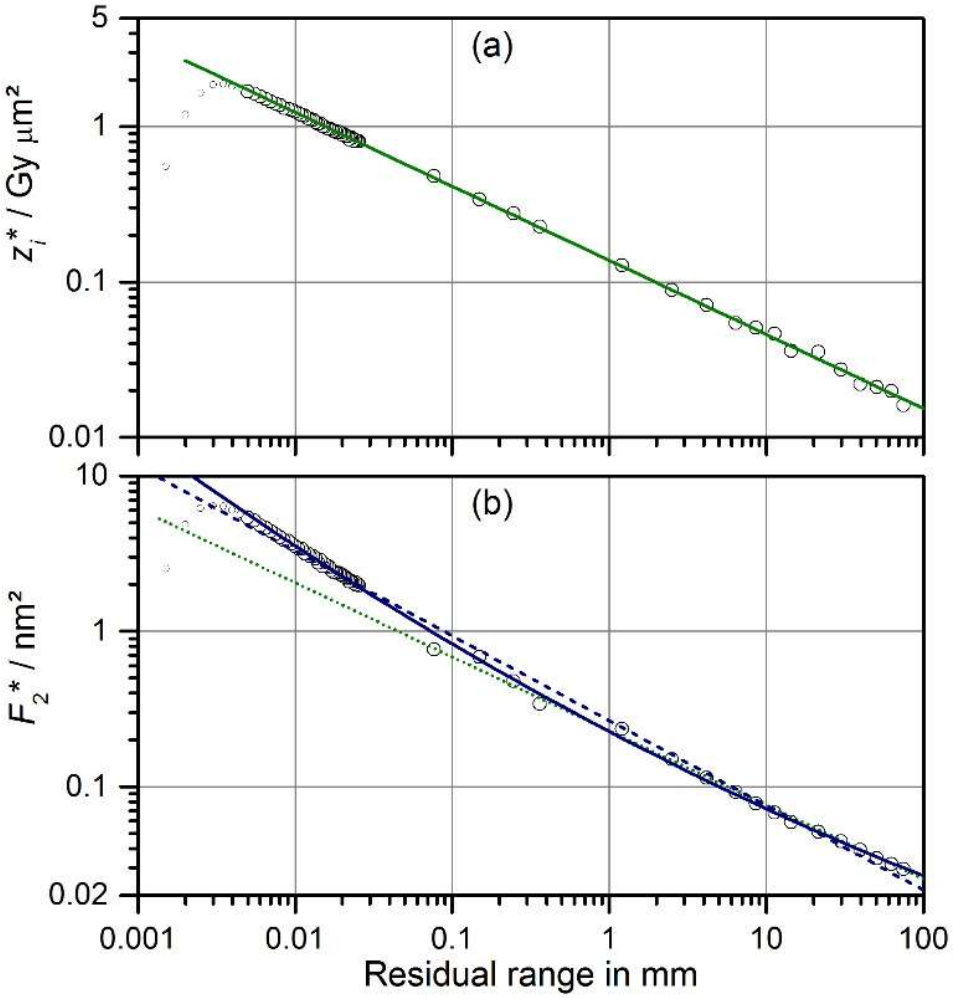

Fig. 63: (a) Dependence of the AISEI obtained from the track simulations on the residual range of the proton (symbols). The line shows the best fit to a power law for residual ranges exceeding 5 µm (larger symbols). (b) Dependence of the effective track cross section with respect to nanodosimetric parameter F_2 on the residual range of the proton (symbols). The lines show best fits to a power law (dashed) and to a second-order polynomial in the log-log plot (solid line) for residual ranges exceeding 5 µm (larger symbols). The dotted line is the best fit to the data at energies ≥ 3 MeV (residual range > 0.1 mm) where the exponent in the power law was forced to be equal to the one found for the AISEI.

The relative variation of the probability area integrals and the AISEI in the PBPs are shown in Fig. 66(b). Here, the data curves have been normalised to unity at the

start of the proton path, and different spans have been chosen for the left- and right-hand part of the figure, such as to emphasise the PBP region.

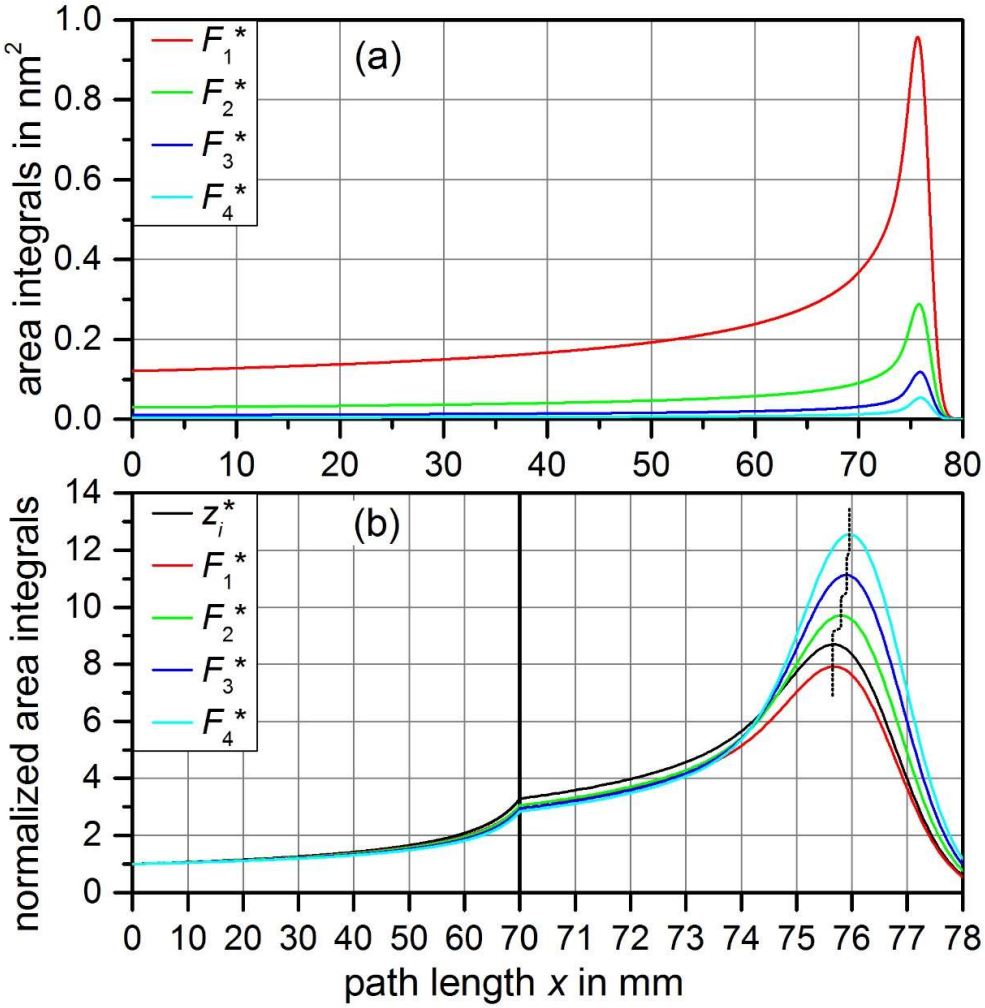

Fig. 65: (a) Variation with path length of the area integrals of the first four nanodosimetric cumulative frequencies F_1 to F_4 for a proton beam with 100 MeV initial energy. (b) Relative variation with path length of the area integrals of energy deposited by ionizations z_i and of the first four nanodosimetric cumulative frequencies F_1 to F_4 for a proton beam with 100 MeV initial energy. The right half shows a close-up of the pristine Bragg peak region. All curves have been normalized to their respective value at 0 mm. The dotted line is a guide to the eye illustrating the shift in peak position.

It can be seen that all curves exhibit a similar relative dependence with the path in the entrance region where the AISEI curve is higher than those of the nanodosimetric parameters.

The curve for the probability area product that a target receives at least one ionisation (and, hence, energy is subsequently deposited in the target) peaks at the same position as the AISEI but with a slightly lower value than that of the AISEI.

This finding is to be expected as the mean energy deposited by ionisations should be proportional to the mean ionisation cluster size, which is given by the sum of the curves shown in Fig. 66(a).

As indicated by the connected vertical dashed lines in Fig. 66(b), the peaks of the nanodosimetric quantities for a higher minimum number of ionisations are increasingly shifted to larger path lengths by as much as 0.3 mm for F_4*. Furthermore, their peak values relative to the value at path 0 mm are also significantly enhanced compared to the curve for the AISEI. Both findings suggest an enhanced probability for more complex DNA damage and, hence, a potential higher RBE at the distal edge of the PBP.

Fig. 68 shows the SOBPs for maximum proton energy of 100 MeV, where $n = 80$ PBPs were superimposed applying Eqs. (25) and (26) with a target relative width of the SOBP of 25%, the maximum range for the SOBP of the AISEI. The results for F_1* have been suppressed as they almost coincide with those for the AISEI. In order to illustrate the relative variation along the SOBP, all data curves in Fig. 68 were normalised to their value at path length 60 mm, which also shows the values at path length 0 mm to coincide. (Normalisation at the distal edge position, where the AISEI is 80% of the value in the plateau region, would be unsuitable for this comparison.)

As with the PBPs, the AISEI is slightly higher than the nanodosimetric results in the entrance region, although these differences are only marginal. Starting from about the middle of the SOBP, the curves for F_2* to F_4* all rise above unity and peak at different positions with maximum values between 1.1 for F_2* and 1.35 for

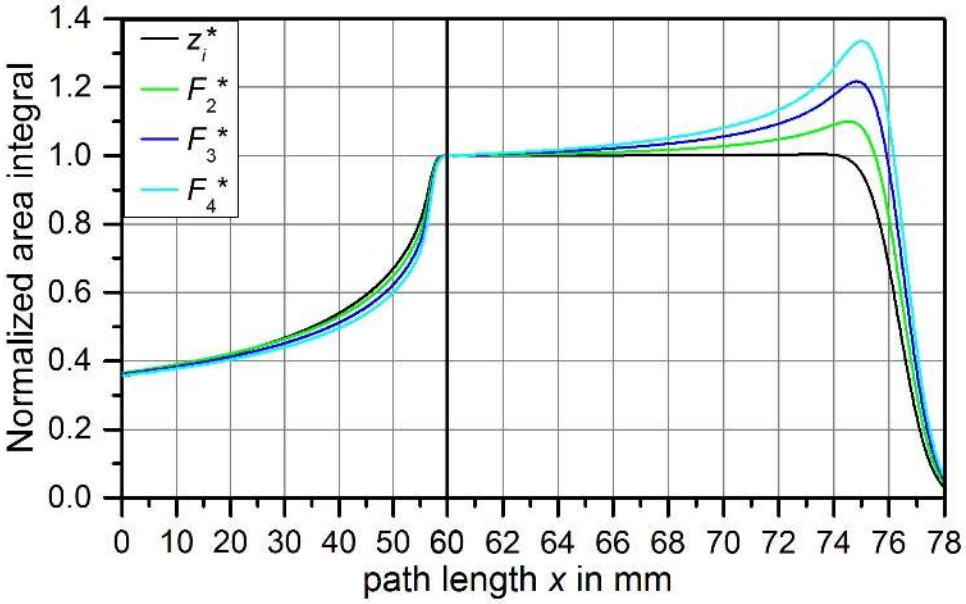

Fig. 67: Relative variation of the area integrals of the nanodosimetric cumulative frequencies F_2 to F_4 for a range distribution leading to a constant area integral of deposited energy along a proton SOBP. The maximum initial proton energy is 100 MeV and the relative width of the SOBP is 25% of the maximum range. The right panel shows a close-up of the SOBP peak region. All curves have been normalized to their respective value at path length 60 mm. The area integral of the specific energy by ionisations (z_i*) is also shown.

F_4*. It is also evident from Fig. 68 that the distal fall-off of the nanodosimetric curves occurs at slightly higher values than the fall-off of the AISEI.

4.3 **Detailed Analysis Of The Radial Dependence**

4.3.1 **Introduction**

Considering the limitations of the results presented in the heuristic approach of the previous section (4.2); due to the imposed radial limit of 100 nm in the calculation of clusters, the current section presents detailed results that overcome this limitation. The radial cut-off at 100 nm results in underestimating the radial integrals of nanodosimetric quantities calculated in this study because the contribution of ionisations due to electrons with higher ranges are ignored. Fig. 71

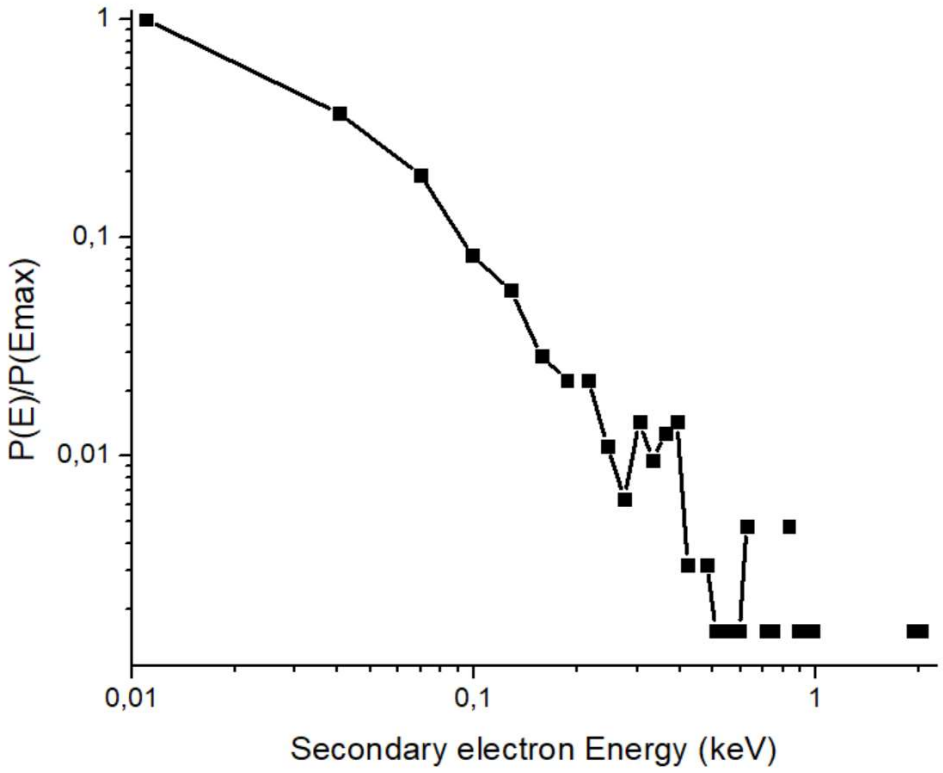

Fig. 69 The relative secondary electron spectrum from a 1 MeV proton calculated from simulations in Geant4-DNA presented in section 3.1.1. The spectrum is normalised to the maximum value.

presents the calculated recoil spectrum of secondary electron released by a 1 MeV primary proton.

It is apparent from this figure that secondary electrons resulting from 1 MeV proton primary particles are primarily of energies of 100 eV and below. However, there is a finite number of electrons of energies larger than 100 eV, which are excluded by the cut-off of 100 nm used in the previous section. Therefore, the current study explores an efficient and detailed analysis of the radial dependence and extends the analysis to radial distance more than 100 nm.

4.3.2 **Radial dependence**

Sample results for the dependence of the first four elements of the complementary cumulative ICS distribution on the radial distance from the proton trajectory are

shown in Fig. 73 for the lowest and highest simulated proton energy, i.e. for 1 MeV and for 99 MeV.

The graphs in Fig. 73(a) qualitatively all show a decrease with radial distance. While the primary trajectory passes through the target, the parameter values decrease significantly as the impact parameter approaches the cylinder radius (1.15 nm). For trajectories passing nearby the cylinder, no power law applies (that would be represented as a straight line in a double logarithmic presentation of the data). Beyond $r \approx 100$ nm, a stronger decrease with radial distance is seen, and at even larger distances the data seem to follow a power law.

Fig. 73(b) shows a similar qualitative relation between the different frequencies. In the radial region, where the proton trajectory intersects the target cylinder, much lower frequency values are observed than for 1 MeV protons, which is explained by the decrease of the proton ionisation cross-sections with increasing proton energy. At this proton energy, the data points almost follow a linear trend from about $r \approx 10$ nm, while a steeper fall-off is observed at $r \geq 1000$ nm.

The double logarithmic presentation of Fig. 73 seems to be appropriate given the several orders of magnitude variation of the nanodosimetric parameters with radial distance. In other work (Wang and Vassiliev, 2014; Frauke Alexander *et al.*, 2015) such a presentation of results has also been used for comparison of data and fits to functional models of the radial dependence. However, it should be noted that this method of presentation does not include the data point at $r = 0$ nm, nor does it properly show the contribution of different radial ranges to the overall radial integral.

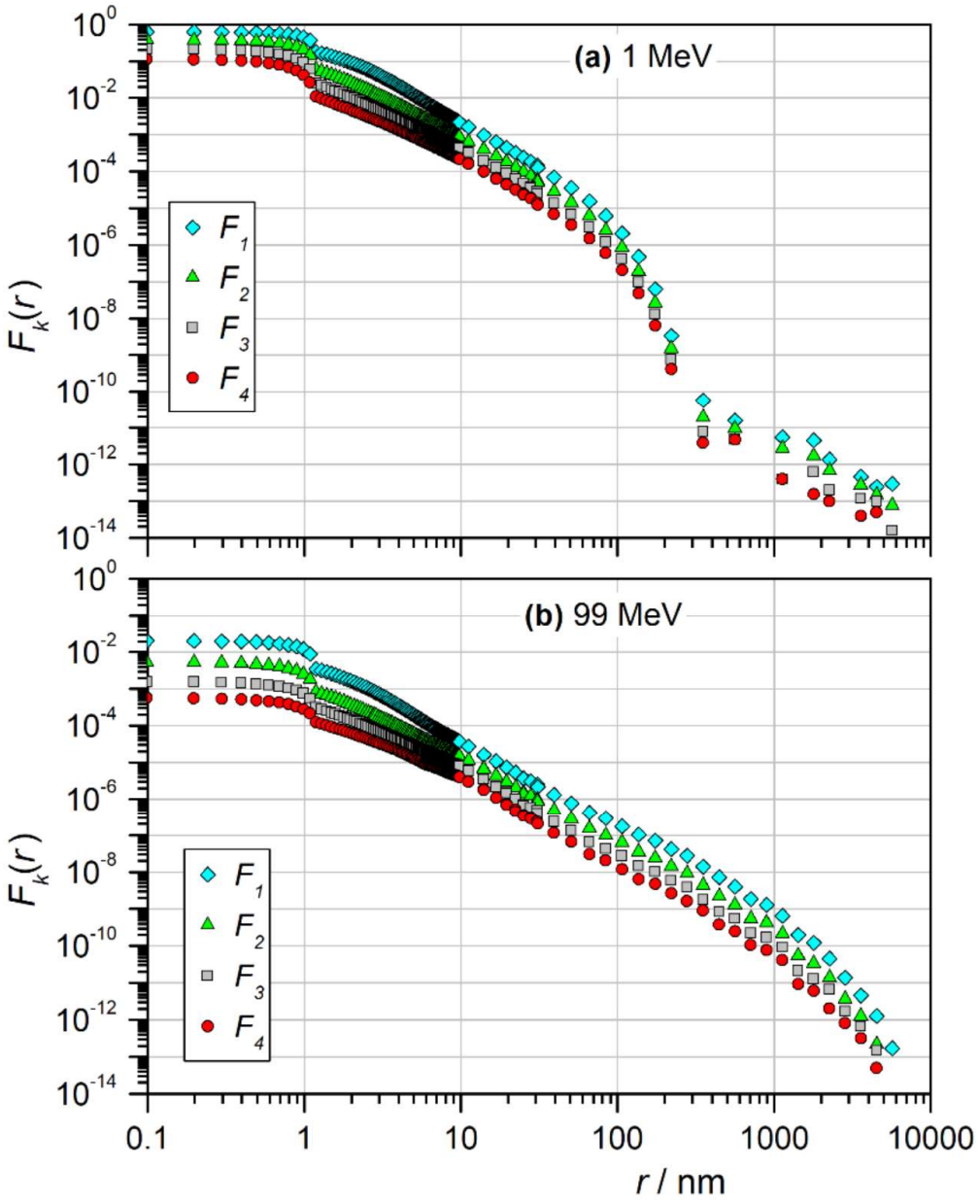

Fig. 72: Radial dependence of the frequencies for nanometric targets receiving at least one (F_1), two (F_2), three (F_3) or four (F_4) ionizations as a function of the radial distance from the trajectory of a proton in water for (a) 1 MeV and (b) 99 MeV proton energy. The proton tracks were simulated using Geant4-DNA and scored with cylindrical target volumes of r_0 = 1.15 nm radius and 3.4 nm height or cylinder shell segments as illustrated in Fig. 46.

4.3.3 **Improved presentation of the radial dependence**

The presentation of the radial dependence as presented in Fig. 73 has a few problems, and we now address these issues. A different way of presenting results, inspired by the conventional way of graphically displaying microdosimetric spectra (Rossi and Zaider, 1996; Lindborg and Waker, 2017), is introduced. But, the current presentation is different from microdosimetry in that a mixed presentation is used; where the first part of the x-axis (from 0 to r_0) is linear and the second part is logarithmic. This allows including the data point at $r = 0$ and gives a degree of freedom in plotting, namely the choice of the ratio of the tick interval lengths (on paper) that are used left and right of the point $r = r_0$. This choice gives the possibility to balance the heights of the peaks occurring in the ranges $r < r_0$ and $r > r_0$ (see, e.g. Fig. 75). In this work, the plotted length of a decade at $r > r_0$ corresponds to the length of the interval between 0 and r_0 so that effectively the following change in coordinates for the x-axis is applied:

$$t = \begin{cases} r/r_0 & @\ r \le r_0 \\ 1 + log_{10}(r/r_0) & @\ r > r_0 \end{cases} \tag{65}$$

where $r_0 = 1.15$ nm is the radius of the target cylinder and $\log_{10}$ the decimal logarithm.

The requirement that the area under the curve shall be proportional to the contribution of the respective radial range to the total radial integral, then implies that the quantities given by Eq. (66) are to be plotted on the y-axis.

$$y^*(t) = \begin{cases} 2\pi r_0 r\, y(r) & @\ r \le r_0 \\ ln(10)\, 2\pi r^2 y(r) & @\ r > r_0 \end{cases} \tag{66}$$

Here y denotes any of the scored quantities, i.e. F_1, F_2, F_3, F_4, and ln denotes the natural logarithm.

The results for the complementary cumulative frequency of targets receiving at least one ionisation (F_1) are shown for five proton energies in Fig. 75. These selected energies cover the energy range of simulated protons from less than 1 MeV to 100 MeV and are thought to be representative of the entire dataset and the resulting

findings. In order to highlight the dependence of the radial distribution on the energy of the primary particle, each of the panels in Fig. 75 shows two consecutive energies (among those chosen for presentation), where the higher energy value is used as the lower one in the subsequent panel. The results show that there is only minor variation with energy in the range $r < r_0$. In the remaining track core and inner penumbra regions, variation with energy is observed at the smallest considered proton energies. From about 10 MeV and beyond, however, the radial dependence remains the same. For the outer penumbra region, the dependence is invariant with energy at least from about 30 MeV, and the variations between 10 MeV and 30 MeV are also minor.

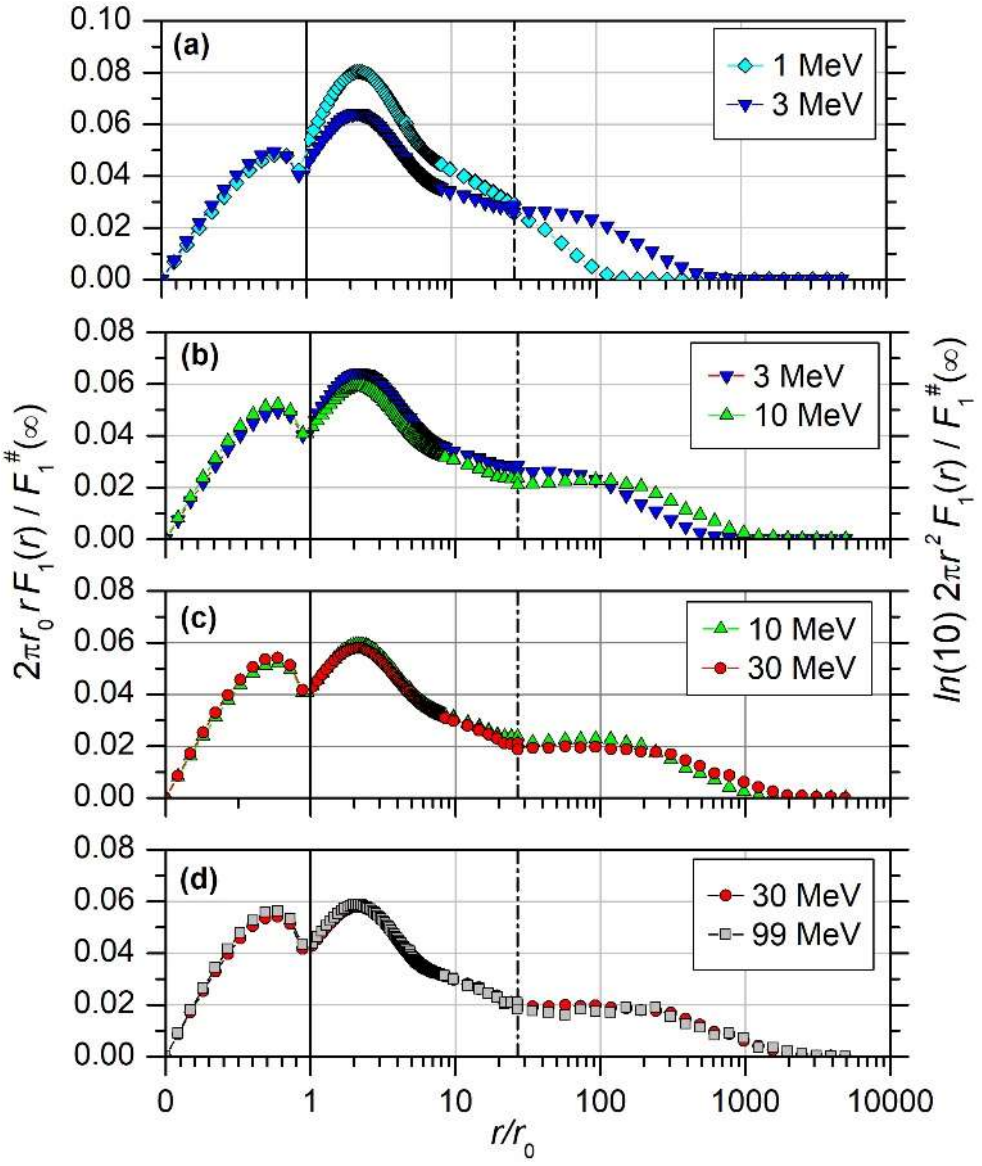

Fig. 74: Dependence of the frequency F_1 of nanometric targets scoring one or more ionizations as a function of the radial distance from the trajectory of a proton in water for different proton energies. The proton tracks were simulated using Geant4-DNA and scored in either cylindrical target volumes of r_0 = 1.15 nm radius and 3.4 nm height (left of the dash-dotted vertical line) or cylinder shell segments as illustrated in Fig. 46 (only data for $r/r_0 > 10$ are shown). The results are plotted such that the area under the curve is proportional to the contribution of the respective distance range to the complete radial integral $F_1^{\#}(\infty)$. The solid vertical line indicates the change from a linear to a logarithmic scale on the x-axis.

Fig. 75 also shows for higher proton energies a plateau region in the radial dependence of the frequency of targets receiving at least one ionisation around $r/r_0 = 100$ that indicates an approximate $1/r^2$ dependence for higher proton energies, while for significantly larger radial distances, a steeper decrease applies.

Fig. 77 shows results for the complementary cumulative frequency of targets receiving at least two ionisation (F_2) are shown for at least six proton energies. In order to highlight the dependence of the radial distribution on the energy of the primary particle, the two panels in Fig. 77 shows three consecutive energies (among those chosen for presentation), where the higher energy value is used as the lower one in the subsequent panel. The results show that there is a significant variation of F_2 with energy, in the range $r < r_0$ to the end of the inner penumbra regions, at energies of 10 MeV and less. For energies of about 10 MeV and beyond, the radial

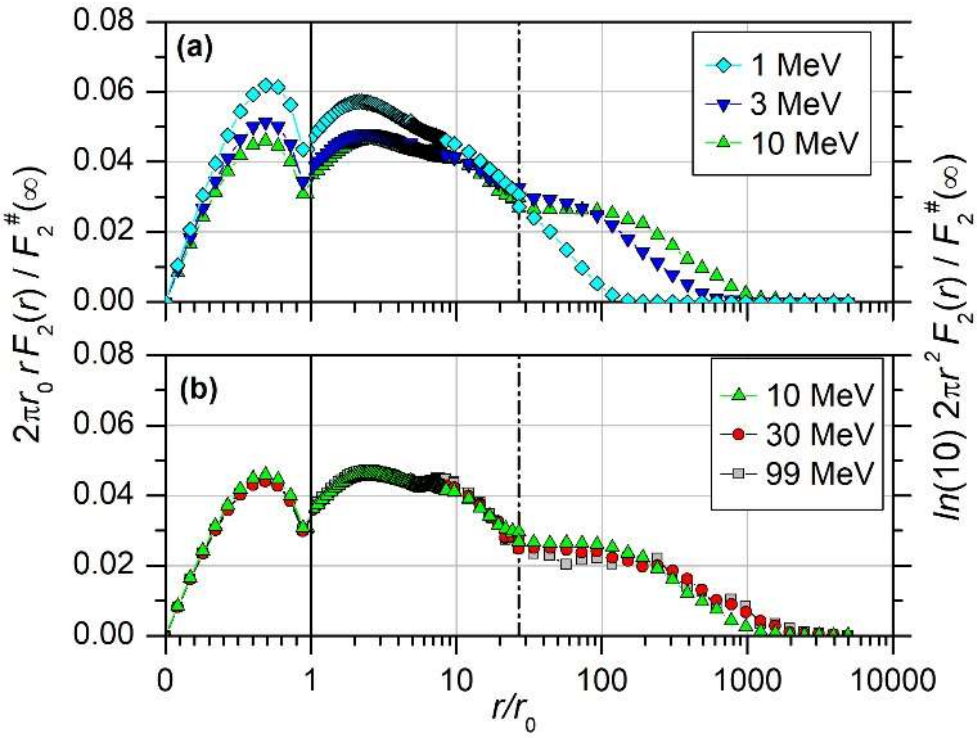

Fig. 76: Dependence of the frequency F_2 of nanometric targets with two or more ionizations as a function of the radial distance from the trajectory of a proton in water for different proton energies. See Fig. 75 for details of the simulation setup and presentation of results.

dependence remains invariant with energy from $r = 0$ *to* the end of the out penumbra (at $r/r_0 = 30$ *nm*).

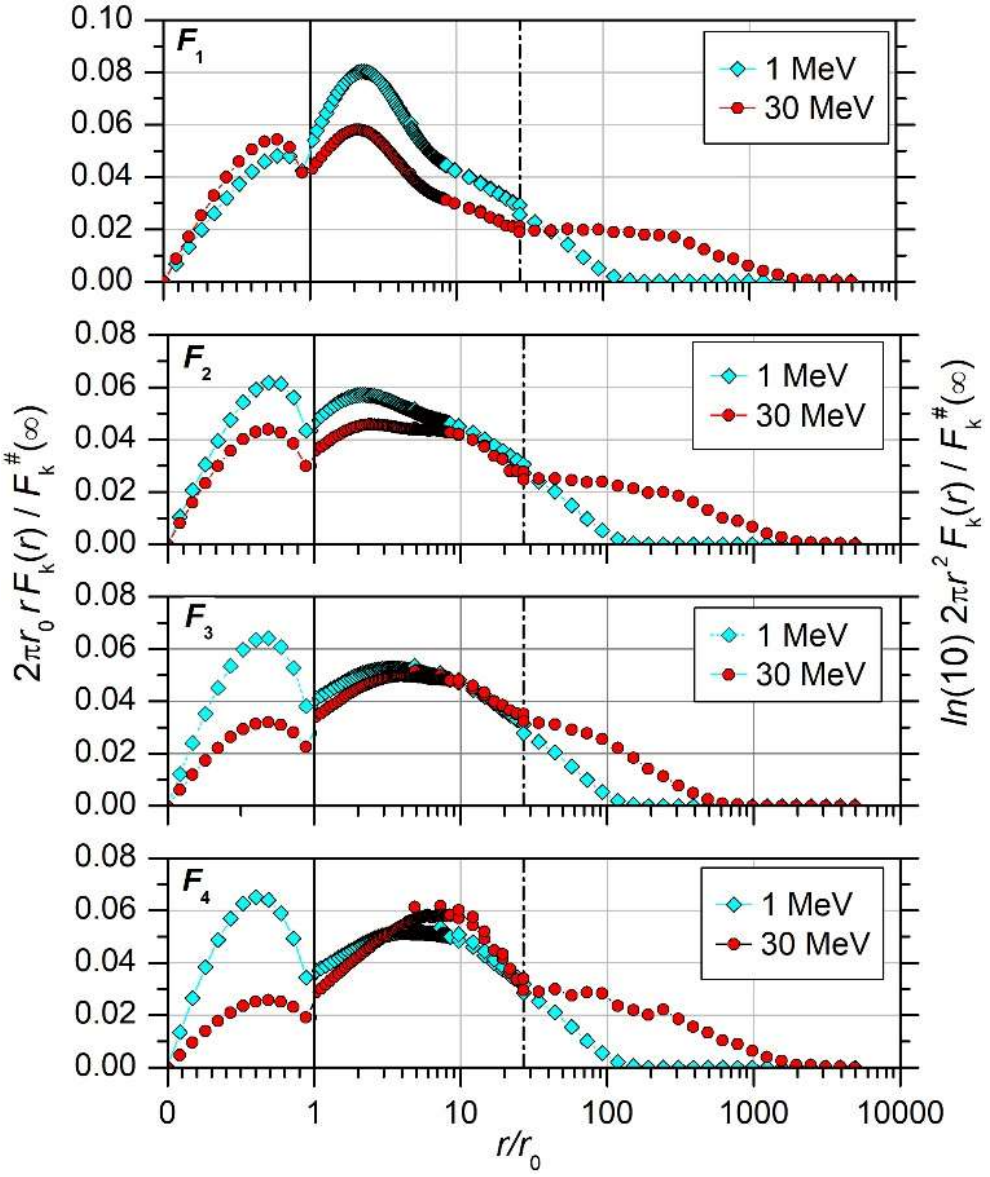

Fig. 78: Comparison of the radial distributions for the complementary cumulative frequencies of targets receiving at least (a) one, (b) two, (c) three or (d) four ionizations at 1 MeV and 30 MeV proton energy. See Fig. 75 for details of the simulation setup and presentation of results.

To further investigate these observations, Fig. 79 shows a synopsis of the radial dependences for the occurrence of targets with at least one, two, three or four ionisations.

Proton energies of 1 MeV and 30 MeV are shown, where the latter represents the energy range in which the radial distribution was found to be invariant with proton energy (Fig. 75 and Fig. 77).

4.3.4 **Modelling of the radial dependence of simulation results**

As discussed in the literature review, the prescription of radiotherapy treatment and the evaluation of the treatment plan is usually done by considering physical objective functions. Except for heavy charged particles like carbon ions, biological treatment planning is still in the developmental stage. The intention of the present study was to provide input data for the future development of radiobiological models that would contain overlap integrals of the radial distributions of nanodosimetric parameters as well as geometrical models of biological entities. These would then ultimately find application in modern treatment planning, especially for particle therapy. Hence, the qualitative analysis presented in the preceding section was further investigated, and the dependence of the nanodosimetric parameters on the radial distance was analysed by fitting data-driven parametric models. The 'starting' model used was adapted from the description of Wang and Vassiliev (Wang and Vassiliev, 2014) for the radial dependence of deposited energy in proton tracks:

$$y^*(r) = \left[1 + \left(\frac{r}{r_1} - 1\right) e^{-r/r_2}\right] b_4 e^{-(r/r_3)^{b_6}}, \quad r > r_0 \tag{67}$$

Where y^* denotes any of the considered cumulative frequencies F_1, F_2, F_3, and F_4 transformed according to Eq. (66), and the coefficients b_4, b_6, r_1, r_2 and r_3 are adjustable model parameters that depend on the proton energy. It should be noted that by using the transformed quantities y^* according to Eq. (66), the data and the model curve do not have the $1/r^2$ dependence of the fit curve used by Wang and Vassiliev (Wang and Vassiliev, 2014). This makes it easier to see details in the

comparison between data and fit curves. Further, in contrast to the work of (Wang and Vassiliev, 2014), the data in the inner region at $r \leq r_0$ are not modelled as a constant, but rather according to Eq. (68).

$$y^*(t) = a_1 t\sqrt{1-t^2} + a_2 t^3 \quad t \leq 1 \tag{68}$$

In this equation, t is the surrogate radial coordinate defined in Eq. (65), and the model is a superposition of a term proportional to the chord length of the proton trajectory in the target cylinder and a heuristic second term representing the contribution of secondary electrons (see section 3.1.3), respectively. The coefficients a_1 and a_2 depend on the proton energy.

The respective fit of the data for the total frequency of targets with ionisations F_1 with 30 MeV protons are shown in Fig. 81 (a) for two cases: the best fit to all data points with $r > r_0$ and the fit curve that is obtained if only data point at $r > 30\ r_0$, i.e. starting from the onset of the 'plateau' are considered (dashed line). In the first case, clear discrepancies can be seen at the distal shoulder of the second peak and in the first part of the 'plateau', which indicate deficiencies of the chosen model function. In the second case, the 'plateau' and the fall-off at large distances are well reproduced, while the peak region is underestimated. This indicates that an additional scaling factor would be needed in front of the second summand in the square bracket in Eq. (67).

Fig. 81 (b) shows additional open symbols (triangles) that represent the difference between the data and the dotted curve in Fig. 81 (a). This latter curve corresponds to the factor behind the square brackets in Eq. (67). Visual inspection suggests that these data approximately have the shape of a Gaussian curve which is confirmed by the dot-dashed curve that shows the best fit to a Gaussian function of the radial variable t.

The solid line in Fig. 81 (b) is the best-fit curve based on Eq. (68) and the following model function in the penumbra region with a Gaussian component:

$$y^*(t) = \left[1 + g_1 e^{-g_2(t-g_3)^2}\right] b_4 e^{-b_5 e^{b_6 t}} \quad t > 1 \tag{69}$$

The model parameters b_4 and b_6 correspond to those designated with the same symbols in Eq. (67), and the exponential factors behind the square brackets in both equations describe the same functional form. Comparison of this fit curve with the data reveals a slight reduction in discrepancies in the range between $r/r_0 = 10$ and $r/r_0 = 100$.

Finally, Fig. 81 (c) shows the data together with the best fit to Eq. (68) and a model function for the penumbra given by:

$$y^*(t) = [b_1 L(b_2 t + b_3) + b_4] e^{-b_5 e^{b_6 t}} + b_7 e^{-b_8 t} \qquad t > 1 \qquad (70)$$

Here, L is a Landau distribution defined by

$$\mathrm{L(x)} = \frac{1}{\sqrt{2\pi}} \mathrm{e}^{-\frac{1}{2}(\mathrm{x}+\mathrm{e}^{-\mathrm{x}})} \qquad (71)$$

The coefficients a_1, a_2, and b_1 through b_8 are adjustable model parameters that depend on the proton energy.

In Fig. 81 (c), the dotted line is the curve described by the factor behind the square brackets in Eq. (70). The dashed line is the sum between the dotted line and the last summand in Eq. (70) and represents a function that continues the fitted curve for $r < r_0$. The open symbols are the difference between the data and the dashed line, which are well reproduced by the best-fit Landau function (dot-dashed line). Overall, the fit according to Eq. (70) shows the least deviations from the data among the three model functions tested. The two additional parameters can, in principle, be eliminated if continuity at $r/r_0 = 1$ is required between the dashed line and the fit curve for $r \leq r_0 = 1$.

The comparison of data and fits for the first three elements of the cumulative ICS frequency distribution in Fig. 83 (for 30 MeV protons) shows, on the other hand, that for ICS of higher complexity, the radial dependence in the penumbra is not well described by the model functions given by Eqs. (67), (69) or (70). The data have all been fitted to Eq. (70) with the requirement that the initial slope of the data at $1 < r/r_0 < 2.5$ and the dependence at large radial distances are reproduced. The best fit over the whole radial range would have led to large discrepancies between the

data and fit. Furthermore, it is worth noting that for F_3, there would not be a 'baseline' that is a smooth continuation of the curve at $r/r_0 < 1$ as was found with the dashed line in Fig. 81 (c). In fact, for F_2 there is also a clear step between the regions $r/r_0 < 1$ and $r/r_0 > 1$.

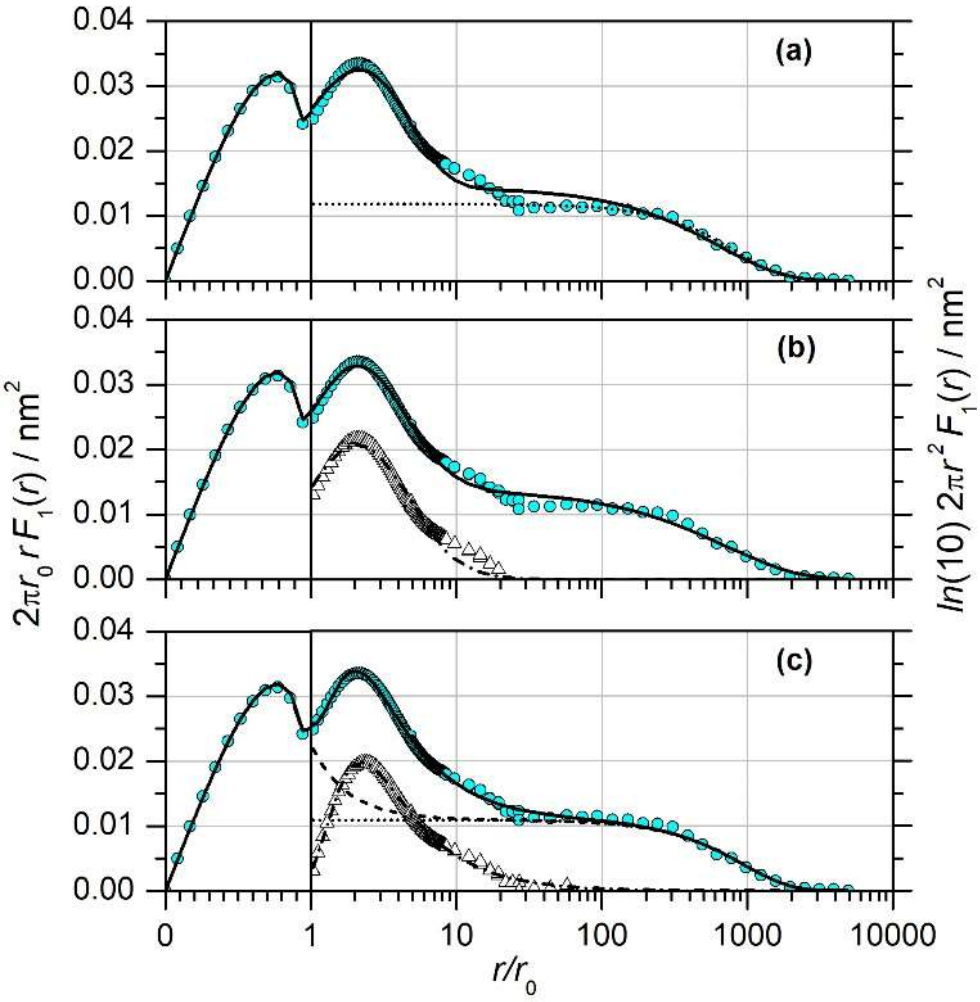

Fig. 80 Fits of the radial dependence of the frequency of nanometric targets with ionizations for 30 MeV protons. In all panels, the full circles show the results from the simulations and the solid line at $r \leq r_0$ is the best fit to Eq. (68). The meaning of the additional symbols and the lines for $r > r_0$ is as follows: (a) The solid line is the fit of the radial dependence with the model adapted from (Wang and Vassiliev, 2014), Eq. (67). Dotted line: Result of the fit to the data at $r > 30\, r_0$ and extrapolation towards smaller radial distances. (b) Open symbols are the difference of the data and the dotted line in (a). Dot-dashed line: Fit of these data with a Gaussian function of log r. Solid line: Best fit to Eq. (69) (c) Solid line: Best fit to Eq. (70). Dotted line: Extrapolation towards smaller radial distances of part of the fit function describing the radial dependence at $r > 30\, r_0$. Dashed: Superposition of the dotted line and the last term in Eq. (70). Open symbols: Deviation of the data from the dashed line. Dot-dashed line: Fit of the open symbols with a Landau distribution of log r.

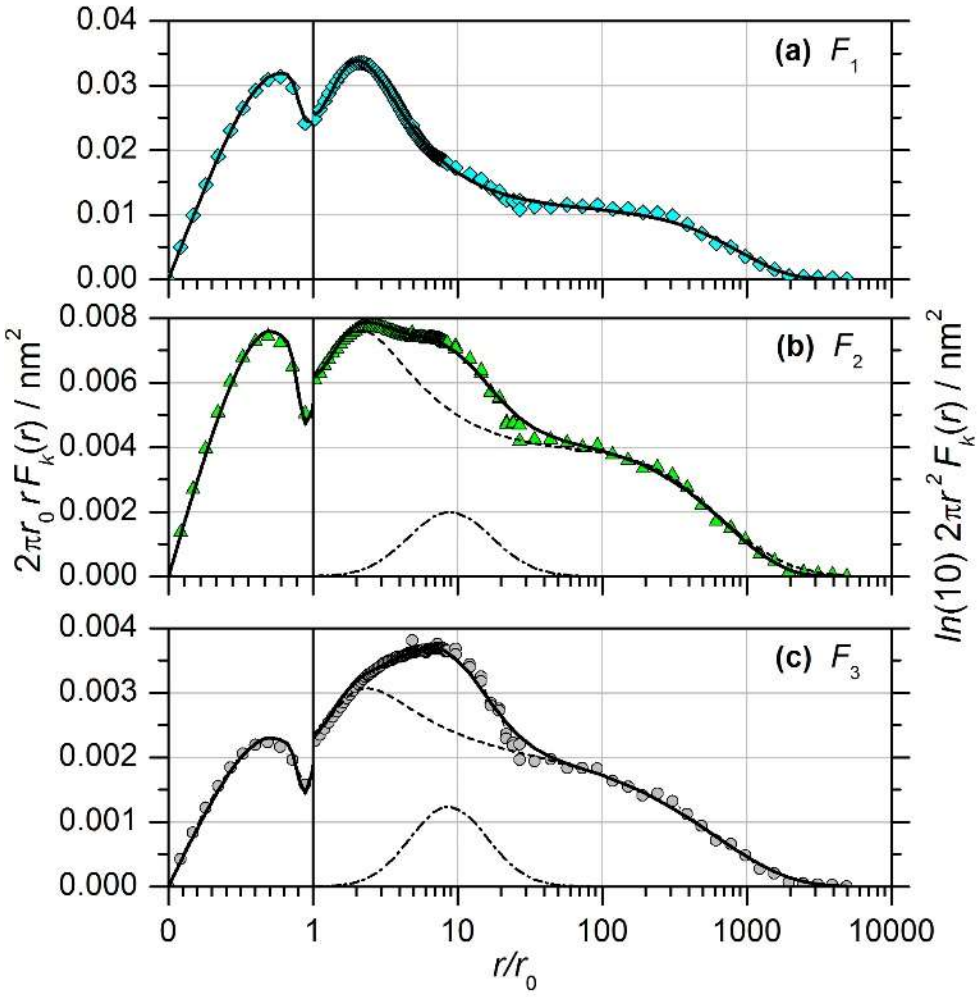

Fig. 82 Comparison of the results and fits of the radial dependence of the frequency of nanometric targets with at least one (a), at least two (b) and at least three (c) ionizations for 30 MeV protons. The results from the simulations are shown as symbols. The solid lines at $r/r_0 < 1$ are the best-fit curves, according to Eq. (68). The dashed line in (a) is the best-fit curve according to Eq. (70). The dashed lines in (b) and (c) are best fits to Eq. (70). If only data at $r/r_0 < 2.5$ and at $r/r_0 > 30$ are taken into account. The solid lines in (b) and (c) are the sum of the dashed line and the additional Gaussian component shown as dot-dashed lines.

The dashed lines in Fig. 83(b) and (c) include the Landau functional shape that peaks at the same radial distance of about $r = 1.38\ r_0$. The missing contribution required for the best-fit curves (shown as solid lines) has a Gaussian shape (dot-dashed curve) as a function of the surrogate radial variable t, where the maximum is found at about $r/r_0 = 9$ and the widths are comparable to each other.

4.3.5 **Cumulative radial distributions**

A common feature of the results shown in Fig. 75 through Fig. 81 is that even though for almost all proton energies the modal value occurs for radial distances where the proton trajectory passes through the target cylinder, the larger fraction of targets with ionisations or with at least two ionisations is not intersected by the proton trajectory. This is further illustrated by Fig. 85, which shows the cumulative frequencies of targets receiving at least one (a), two (b) or three (c) ionisations depending on their maximum distance from the trajectory.

For all proton energies, only about 25% to 30% of the targets receiving ionisations are traversed by the proton trajectory, where these values are generally slightly lower for at least two energies of 1 MeV, with increasing minimum complexity of the ionisation cluster, there is an increased probability that the proton trajectory traverses the affected target. For the two cases shown in Fig. 85(b) and (c), however, this probability remains below 50%.

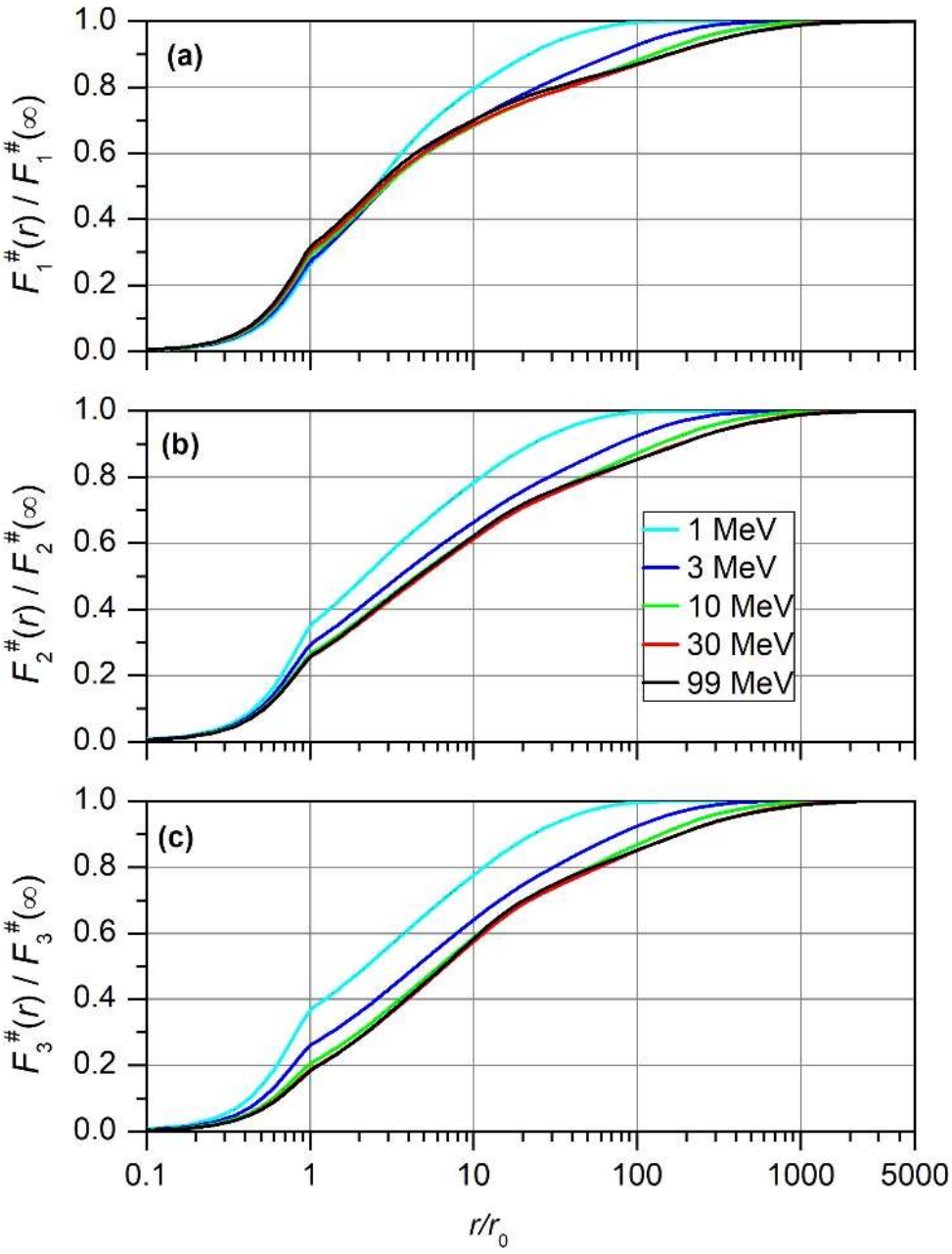

Fig. 84: Partial radial integrals between 0 and the value given on the *x*-axis of the complementary cumulative frequencies F_k of targets receiving at least one (a), two (b) or three (c) ionizations for protons of different energies as shown in the legend. The partial integral values, $F_k^{\#}(r)$, were normalized to their respective values when the intetegral is carried out to infinity, $F_k^{\#}(\infty)$.

4.3.6 **Consistency of the two scoring approaches**

The method of presenting results in Fig. 75 and Fig. 77 has the advantage that potential differences between the scoring approaches used in the inner and outer penumbra regions become more evident. In fact, particularly for the 1 MeV data in Fig. 75(a), there is a clear visible downward step in the data around $r / r_0 = 30$, i.e. at the radial distance (and beyond) where scoring was exclusively done using cylinder segment targets. This may indicate a systematic effect imposed by the different target shapes.

In fact, this downward step was observed for all proton energies and cumulative ICS frequencies. The respective values obtained for the first four cumulative ICS frequencies of the proton energies shown in Fig. 75 and Fig. 77 are shown in Table 5 Ratio of the results obtained for cylindrical targets and cylinder shell segments both with the same volume) for the specified proton start energies Ep and the first four cumulative ICS frequencies using option 1 (see section 3.2.3) for defining the cylinder shell segments. The values are the ratios for the largest radial distance where both scoring approaches were applied. The last row shows the mean over the five energies and the associated sample standard deviation (given in brackets as multiple of the last significant digit).

Ep / MeV	F1	F2	F3	F4
1	1.18	1.18	1.19	1.21
3	1.08	1.08	1.09	1.11
10	1.11	1.12	1.11	1.12
30	1.12	1.14	1.13	1.14

100	1.15	1.18	1.19	1.25
mean	1.12(4)	1.14(4)	1.14(5)	1.17(6)

Table 6 together with the mean and standard deviation (last row). These data also suggest that there may be a systematic effect related to the different target geometries that should be taken into account by scaling the data obtained with cylinder shell segments using a scaling factor independent of proton energy and minimum ICS complexity.

However, the results in Fig. 87 suggest that matching the data from the two scoring approaches at the largest radial distance where cylinder targets were used might lead to an overestimation of the 'true' values in the penumbra region. In Fig. 87, the open symbols indicate the results obtained for the case of 10 MeV protons with cylinders (squares) or cylinder shells (circles). The filled circles are the 'corrected' data for scoring with cylinder shells if the aforementioned matching is required.

Table 5 Ratio of the results obtained for cylindrical targets and cylinder shell segments both with the same volume) for the specified proton start energies E_p and the first four cumulative ICS frequencies using option 1 (see section 3.2.3) for defining the cylinder shell segments. The values are the ratios for the largest radial distance where both scoring approaches were applied. The last row shows the mean over the five energies and the associated sample standard deviation (given in brackets as multiple of the last significant digit).

E_p / MeV	F_1	F_2	F_3	F_4
1	1.18	1.18	1.19	1.21
3	1.08	1.08	1.09	1.11
10	1.11	1.12	1.11	1.12
30	1.12	1.14	1.13	1.14
100	1.15	1.18	1.19	1.25
mean	1.12(4)	1.14(4)	1.14(5)	1.17(6)

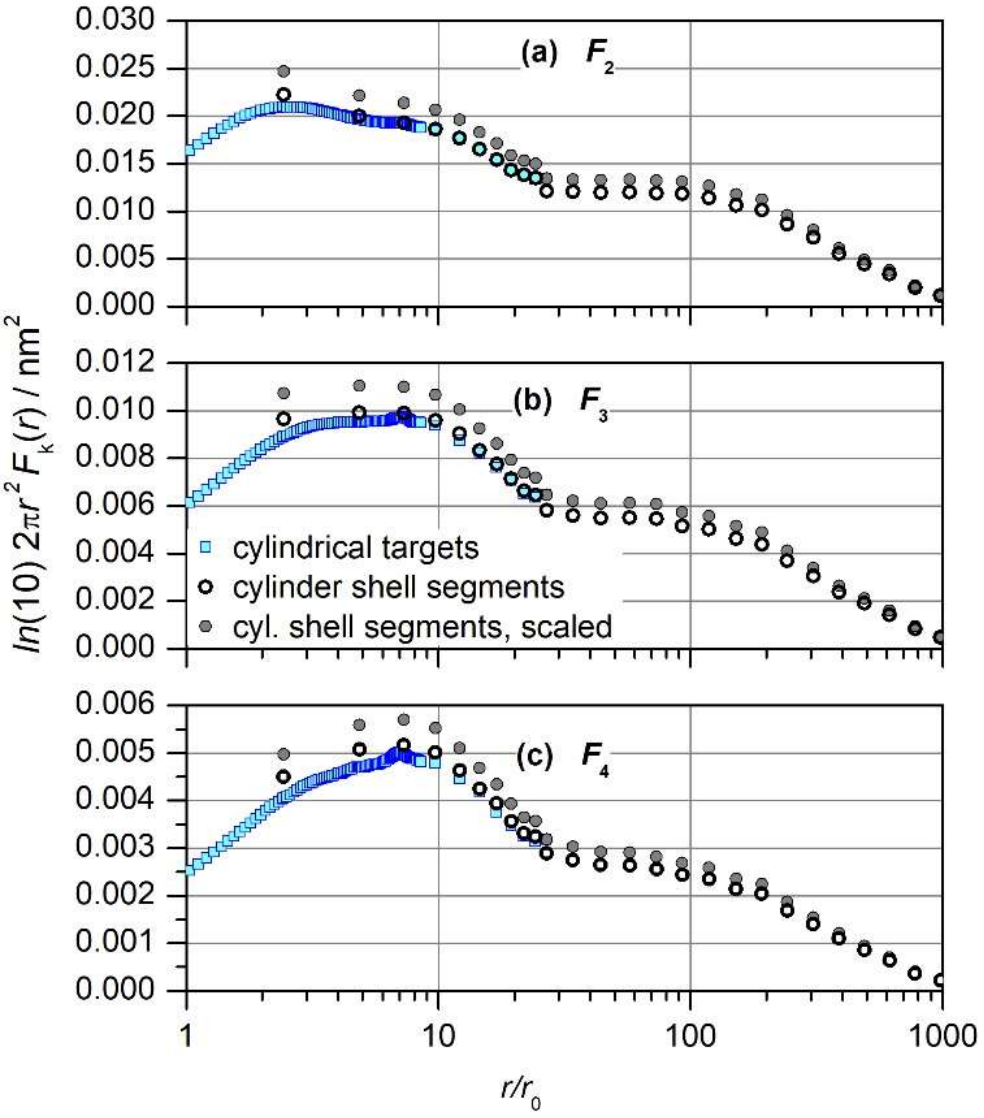

Fig. 86: Comparison of the results for the radial dependence of the cumulative probabilities F_2, F_3 and F_4 for 10 MeV proton energy. The squares indicate data obtained by using cylidrical targets (2.3 nm diameter, 3.4 nm height) and the open circles represent data obtained with targets that are cylinder shells with the same volume as the cylinders according to option 2 (see section 3.2.3). The filled circles are the latter data scaled with a constant factor such that the data of both scoring approaches match at the largest radial distance where cylinder scoring was used.

Table 7 Ratio of the results obtained for cylindrical targets and cylinder shell

For all three parameters F_2, F_3 and F_4, the 'corrected' data in the overlap region (where both scoring approaches were applied) exhibit the same relative dependence on radial distance as the data obtained with cylindrical targets. Only the first two or three data points are an exception to this statement, but for these small radial distances, the discrepancy of the target shape is very pronounced (see Fig. 46), so that discrepancies are to be expected. In fact, for all nanodosimetric cumulative frequencies F_k and all proton energies, it was found that for the first three radial distances, the data obtained with the cylinder-shell segment approach were

Table 8 Ratio of the results obtained for cylindrical targets and cylinder shell segments (both with the same volume) for the specified initial proton energies E_p and for the first four cumulative ICS frequencies using option 2 (see section 3.2.3) for defining the cylinder shell segments. The values are the average of the ratios obtained over targets centred in the third to tenth cylindrical shell around the proton trajectory. The values in brackets are the sample standard deviations of the ratios for eight different radial distances. In the last row, the value in brackets is the standard deviation of the ratio calculated over the eight radial distances and the five energies.

E_p / MeV	F_1	F_2	F_3	F_4
3	1.00(1)	1.00(2)	0.99(3)	1.01(3)
10	0.99(2)	1.00(2)	1.03(4)	1.00(4)
25	0.99(2)	1.00(2)	1.00(5)	1.01(6)
50	1.00(2)	0.99(3)	0.98(5)	0.92(8)
100	1.00(4)	1.00(6)	1.00(5)	1.00(5)
mean	1.00(1)	1.00(1)	1.00(2)	0.99(4)

significantly enhanced, where the discrepancy reduced with radial distance. Consequently, the first three data points obtained with this approach were suppressed when plotting Fig. 73, Fig. 75 and Fig. 77, whereas all other data points were included.

To further investigate the extent to which the data obtained by the two scoring approaches are consistent, the ratio of the data points obtained with cylindrical targets and with cylinder shell segments have been considered. For target centres located between 3 and 10 times the cylinder shell thickness, the ratio was found to hover around a constant value. For the first option of scoring in the outer penumbra, which was also that used in section 3.1.2, the mean values and standard deviations are shown in Fig. 89 as a function of proton energy.

For all nanodosimetric parameters, F_1 to F_4, the ratio of the results obtained with the two different scoring approaches seem to be independent of proton energy, with values of about 1.01, 1.00, 0.98 and 0.96 for F_1, F_2, F_3 and F_4, respectively. Table 8 Ratio of the results obtained for cylindrical targets and cylinder shell segments (both with the same volume) for the specified initial proton energies Ep and for the first four cumulative ICS frequencies using option 2 (see section 3.2.3) for defining the cylinder shell segments. The values are the average of the ratios obtained over targets centred in the third to tenth cylindrical shell around the proton trajectory. The values in brackets are the sample standard deviations of the ratios for eight different radial distances. In the last row, the value in brackets is the standard deviation of the ratio calculated over the eight radial distances and the five energies.

Ep / MeV	F1	F2	F3	F4
3	1.00(1)	1.00(2)	0.99(3)	1.01(3)
10	0.99(2)	1.00(2)	1.03(4)	1.00(4)
25	0.99(2)	1.00(2)	1.00(5)	1.01(6)

50	1.00(2)	0.99(3)	0.98(5)	0.92(8)
100	1.00(4)	1.00(6)	1.00(5)	1.00(5)
mean	1.00(1)	1.00(1)	1.00(2)	0.99(4)

Table 9 Ratio of the results obtained for cylindrical targets and cylinder shell segments both with the same volume) shell for the specified proton start energies Ep and for the first four cumulative ICS frequencies using option 3 (see section 3.2.3) for defining the cylinder shell segments. The values are the average of the ratios obtained over targets centred in the third to tenth cylindrical shell around the proton trajectory. The values in brackets are the sample standard deviations of the ratios at the 8 different radial distances. In the last row, the value in brackets is the standard deviation of the ratio calculated over the eight radial distances and the five energies.**Table 10** and Table 11 Ratio of the results obtained for cylindrical targets and cylinder shell segments both with the same volume) shell for the specified proton start energies Ep and for the first four cumulative ICS frequencies using option 3 (see section 3.2.3) for defining the cylinder shell segments. The values are the average of the ratios obtained over targets centred in the third to tenth cylindrical shell around the proton trajectory. The values in brackets are the sample standard deviations of the ratios at the 8 different radial distances. In the last row, the value in brackets is the standard deviation of the ratio calculated over the eight radial distances and the five energies.

Ep / MeV	F1	F2	F3	F4
3	0.99(1)	0.99(2)	1.00(3)	0.99(3)
10	0.99(2)	0.99(2)	0.99(4)	1.03(4)
25	0.99(2)	1.01(2)	1.01(5)	1.00(6)

50	0.98(2)	0.99(3)	0.99(5)	1.00(8)
100	1.00(4)	1.00(6)	1.00(5)	1.00(5)
mean	0.99(2)	1.00(3)	1.00(4)	1.00(6)

Table 12 show the respective results for the other two options for defining the cylinder shell segments described in section 3.2.3.

These data were obtained from performing the analysis to the data of (Frauke Alexander *et al.*, 2015) that offer the advantage of longer track segments of 10 µm but with fewer simulated primary particles. The results obtained for option 1 have the same average values as those seen in Fig. 89. Conversely, both options 2 and 3 gave mean values that suggest an average ratio between target cylinders and cylinder-segment targets of unity. This better agreement is presumably due to the similar aspect ratio of the cylinder shell targets (arc length by radial diameter) to that of cylinders (height by diameter).

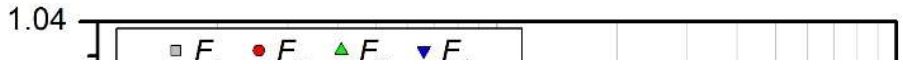

Table 11 Ratio of the results obtained for cylindrical targets and cylinder shell segments both with the same volume) shell for the specified proton start energies E_p and for the first four cumulative ICS frequencies using option 3 (see section 3.2.3) for defining the cylinder shell segments. The values are the average of the ratios obtained over targets centred in the third to tenth cylindrical shell around the proton trajectory. The values in brackets are the sample standard deviations of the ratios at the 8 different radial distances. In the last row, the value in brackets is the standard deviation of the ratio calculated over the eight radial distances and the five energies.

E_p / MeV	F_1	F_2	F_3	F_4
3	0.99(1)	0.99(2)	1.00(3)	0.99(3)
10	0.99(2)	0.99(2)	0.99(4)	1.03(4)
25	0.99(2)	1.01(2)	1.01(5)	1.00(6)
50	0.98(2)	0.99(3)	0.99(5)	1.00(8)
100	1.00(4)	1.00(6)	1.00(5)	1.00(5)
mean	0.99(2)	1.00(3)	1.00(4)	1.00(6)

4.3.7 **Corrections due to long-range electrons**

The scoring procedure for the penumbra as described in section 3.2.3 and illustrated in Fig. 46 ensures that all ionisations produced within the region of interest are scored provided that they arise from proton interactions or from electron tracks that commenced within the 650 nm-thick slab (within which the ionising interactions were scored).

To analyse the influence of electrons with longer ranges that could escape from or enter the 650 nm slab from outside, we used the data of (Frauke Alexander *et al.*, 2015) that were based on simulations of longer track segments (10 µm). Using a variant of the program described in section 8.3.1, The interaction points of first-generation secondary electrons and their daughter particles with respect to the interaction position of the primary particle that produced the secondary electron was determined for each first-generation secondary electron. These secondary electron data were used to obtain the frequency distributions of the radial and longitudinal coordinates of secondary electron interactions. Sample results for the complementary cumulative frequency distributions are shown in Fig. 91 for the cases of 100 MeV, 25 MeV and 3 MeV protons. Fig. 91(a) shows the fraction of the number of ionisations by electrons that occur at a radial distance from the primary particle trajectory larger than the respective value on the *x*-axis. As expected, the radial extension of the penumbra increases with increasing primary particle energy and extends to about 10 µm radial distance for 100 MeV protons, where more than 13% of the ionisations by electrons occur at radial distances larger than 1 µm.

Similarly, it can be seen in Fig. 91(b) and Fig. 91(c) that several percent of the secondary electrons produce ionisations that deviate from the position of the point where the first generation secondary electron was produced by more than the 650 nm slab thickness used in the simulations. Furthermore, for higher proton energies, there is also a significant fraction of electron interactions occurring in the backward direction at distances exceeding a few 100 nm.

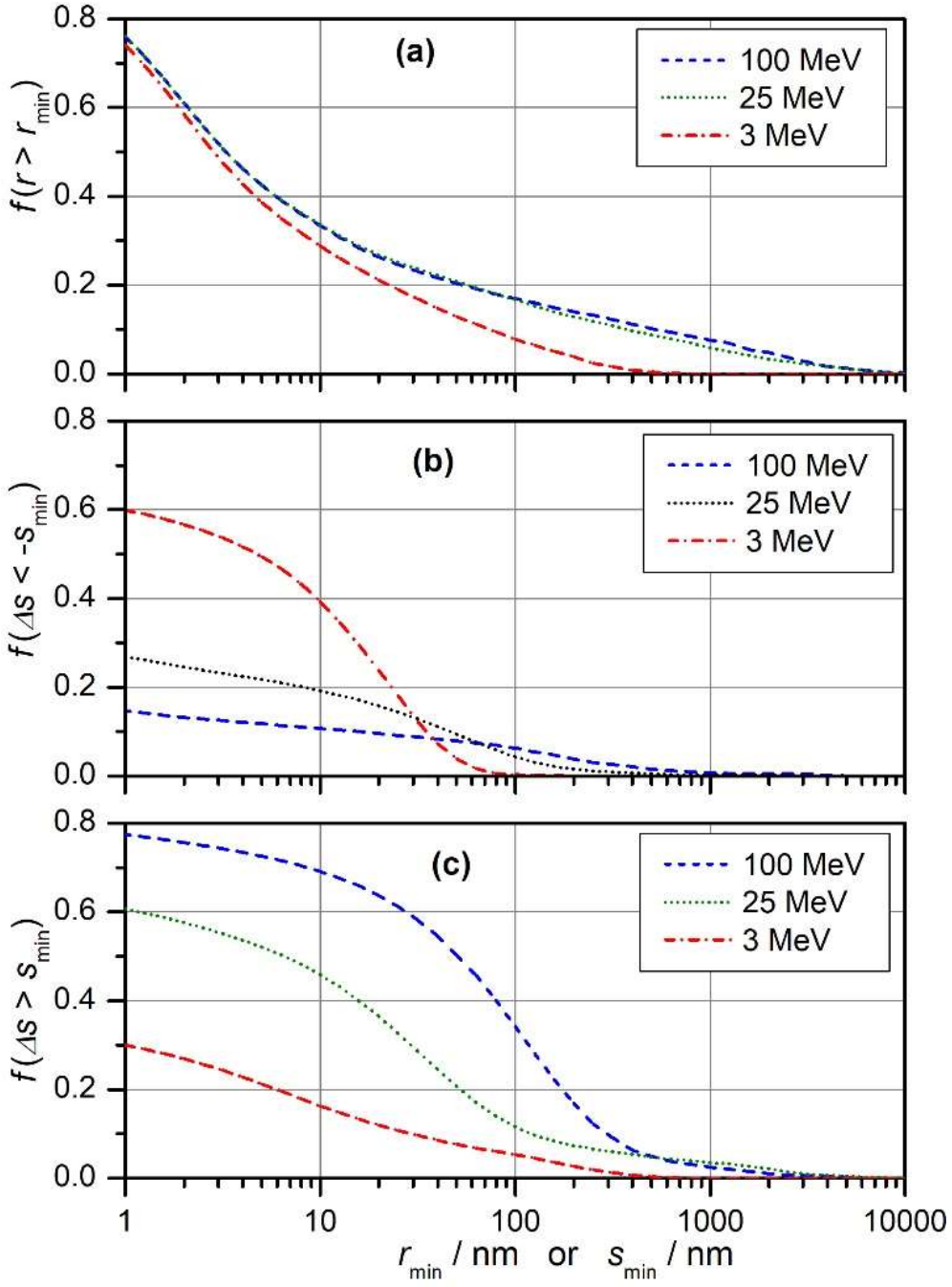

Fig. 90: Complementary cumulative frequency distribution of energy transfer points with ionizing interactions by secondary electrons as a function of: (a) radial distance from the proton trajectory; (b) upstream and (c) downstream distance along the proton trajectory from the interaction point at which the electron track originated. The presentation in (b) and (c) is such that the sum of the frequences in upstream and downstream direction is unit.

These findings suggest that there may be an underestimation of the frequency of ionisations within targets inside the penumbra. This is confirmed by Fig. 93, which shows for two proton energies a comparison of the radial distributions for the first two elements of the complementary cumulative ICS distribution for the present data and the results obtained based on data from the BioQuaRT project (Frauke Alexander *et al.*, 2015).

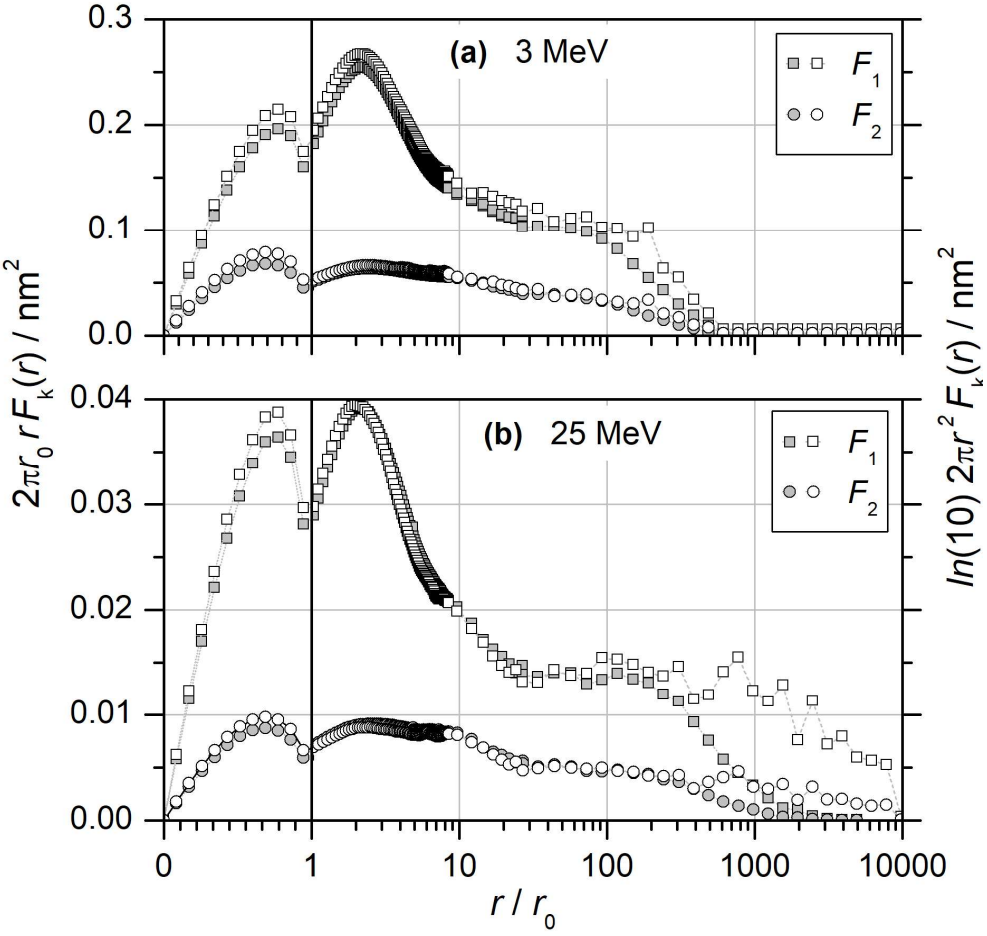

Fig. 92: Comparison of the radial distributions for the first two complementary frequencies F_1 and F_2 obtained in the present work (filled symbols) with those obtained using the same analysis for data from the BioQuaRT project (Frauke Alexander *et al.*, 2015) (open symbols).

The main features in the radial distributions are the same for the two data sets.

Table 14 Ratio of the effective track cross sections obtained with the data from (Frauke Alexander *et al.*, 2015) and with the simulation results of (Rabus *et al.*, 2020) for the specified initial proton energies E_p and for the first four cumulative ICS frequencies using option 1 for defining the cylinder shell segments in the penumbra region (see section 3.2.3). The last row shows the arithmetic mean over the four energy values and the value in brackets is the sample standard deviation.

E_p / MeV	F_1	F_2	F_3	F_4
3	1.11	1.10	1.11	1.11
10	1.21	1.18	1.18	1.18
25	1.16	1.13	1.12	1.10
50	1.16	1.12	1.10	1.09
mean	1.16(4)	1.13(3)	1.13(4)	1.12(4)

Whilst the BioQuaRT-based data are systematically higher by about 5% when the proton trajectory intersects the target cylinder, the two maxima in the track core region occur at about the same positions, and their intensity is also approximately the same. In contrast, the BioQuaRT clearly show radial distributions that have significantly higher values at higher radial distances, where the magnitude of the effect increases with increasing proton energy. In terms of the full integral to infinity, the effect is in the order of 12% to 16% for all energies where data from both simulations were available (Table 14 Ratio of the effective track cross sections obtained with the data from (Frauke Alexander *et al.*, 2015) and with the simulation results of (Rabus *et al.*, 2020) for the specified initial proton energies Ep and for the first four cumulative ICS frequencies using option 1 for defining the cylinder shell segments in the penumbra region (see section 3.2.3). The last row shows the

arithmetic mean over the four energy values and the value in brackets is the sample standard deviation.

Ep / MeV	F1	F2	F3	F4
3	1.11	1.10	1.11	1.11
10	1.21	1.18	1.18	1.18
25	1.16	1.13	1.12	1.10
50	1.16	1.12	1.10	1.09
mean	1.16(4)	1.13(3)	1.13(4)	1.12(4)

Table 15). ¶

One of the shortcomings of the BioQuaRT data was the limited number of primary particles owing to the computation time required for detailed simulation over the 10 µm range. In principle, following the primary particle and all secondary electrons produced by its interactions over such a long track segment may not be necessary. One could rather select a shorter proton trajectory segment as long as the secondary electrons are followed until their energy falls below the ionisation threshold of water of about 10.7 eV. For this, their interactions need to be scored in a larger volume that assures that they lose their kinetic energy by interaction within this scoring volume.

In order to estimate the additional contribution to the fraction of targets within the region of interest (ROI) that receive a certain ICS, it must be assumed that the interference of different electron tracks (that arise from interactions of the protons) is negligible as is the variation of the energy and directional distributions of the

emitted electrons over the proton trajectory segment from which secondary electrons can contribute to the ICS distributions in the ROI.

Then the frequency distributions of targets receiving a certain ICS due to electron tracks starting outside the scoring slab could be derived by the following convolution procedure that is defined by Eqs. (72), (73) and (74).

$$P_{\nu}^{(0)}(r_j, s) = \delta_{\nu 0} \tag{72}$$

$$Q_{\nu}^{(n)}(r_j, s) = \sum_{k=0}^{\nu} P_{\nu-k}^{(n-1)}(r_j, s) P_k(r_j, s + nD_s) \tag{73}$$

$$P_{\nu}^{(n)}(r_j, s) = \sum_{k=0}^{\nu} Q_{\nu-k}^{(n)}(r_j, s) P_k(r_j, s - nD_s) \tag{74}$$

In Eq. (72), s is the centre of the ROI, δ_{v0} is the Kronecker symbol, i.e. 1 if $v = 0$ and else 0. D_s is the thickness of the slab in which proton interactions are scored and the quantities $P_k(r_j, s \pm nD_s)$ are the scored ICS frequencies in slabs of thickness D_s whose centres are offset downstream and upstream from the ROI centre by n times the slab thickness? Owing to the aforementioned assumptions, these frequencies are used as estimators for the contributions in the ROI by electron tracks started in slabs of thickness D_s located upstream or downstream of the ROI, respectively, by nD_s.

Eq. (72) is the starting condition of the recursion relations (73) and (74) that apply for $n \geq 1$, and the Q_v are auxiliary quantities.

Corrected ICS frequencies $P_v^{(*)}$ would then be obtained by convoluting the result obtained by scoring ionisations by protons and electrons in the ROI with the result of the recursion:

$$P_{\nu}^{(*)}(r_j, s) = \sum_{k=0}^{\nu} P_{\nu-k}^{(n_{max})}(r_j, s) P_k(r_j, s) \tag{75}$$

4.4 Dependence Of Nanodosimetric Parameters On The Target Orientation

The following set of results showcase preliminary results of the variation of the cumulative frequency distribution (or the relative frequency distribution) for a cluster of two or more (F2) with the target orientation defined by the *k* value as defined in section 3.3.2. The results are considered preliminary since the radial

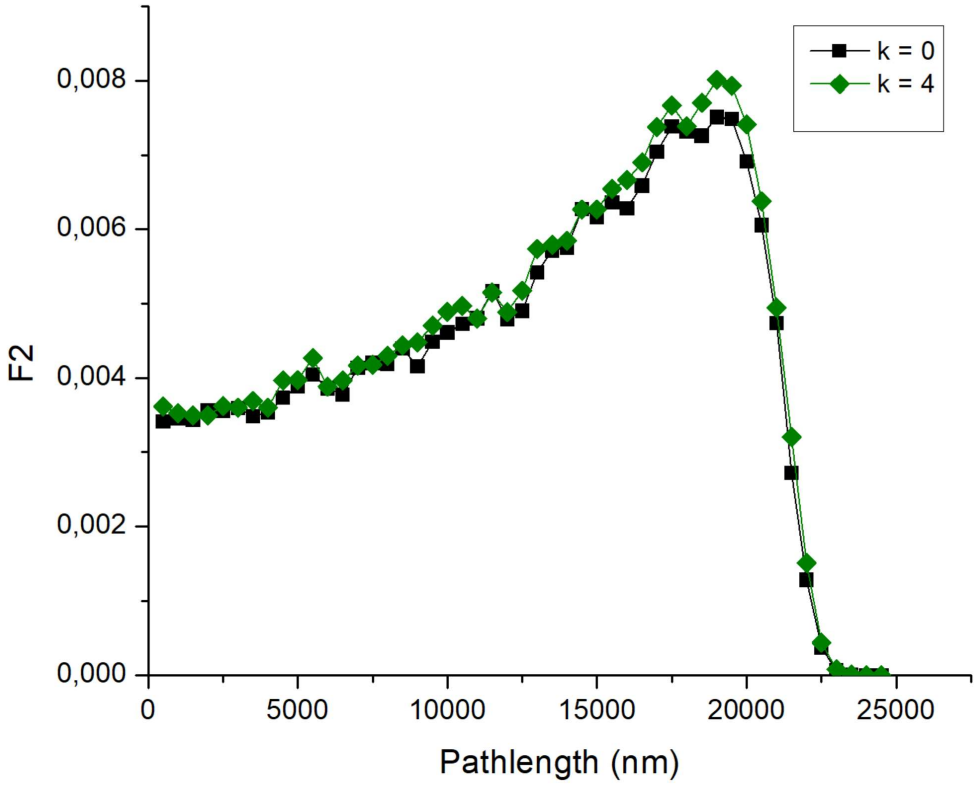

Fig. 94: Presented is the variation of F2 with target orientation along the pathlength. The target volume is rotated through 8 angles and the results are presetent for th the cumulative probability distribution to create 2 or more clusters. The plotted graphs are for radial distance of 5.4 nm.

dependence was analysed using the heuristic method in section 3.1. Therefore, only the results for k=0 and k=4 (i.e. cylinder axis parallel to the proton trajectory or

perpendicular to it) are shown here, for which this error does not have consequences.

From Fig. 95, it is apparent that the cumulative frequency of two or more ionizations (plotted at a radial distance of 5.4 nm) for a 1 MeV proton track shows a minor change as the cylindrical segment is rotated. The relative dependence of the value of F2 for the two orientations is almost the same where the case of a cylinder axis parallel to the proton trajectory gives slightly higher values than an orientation of the cylinder axis perpendicular to the proton trajectory. The change in the value of the cumulative frequency, F2, is related to the range of ionisations defined along the direction of the primary track (distance related to the chord length) and is maximum when this range is defining the longest chord length in the target volume.

Further demonstration of this effect is depicted in Fig. 97 to Fig. 105 where F2 is plotted against the radial distance for all target orientations.

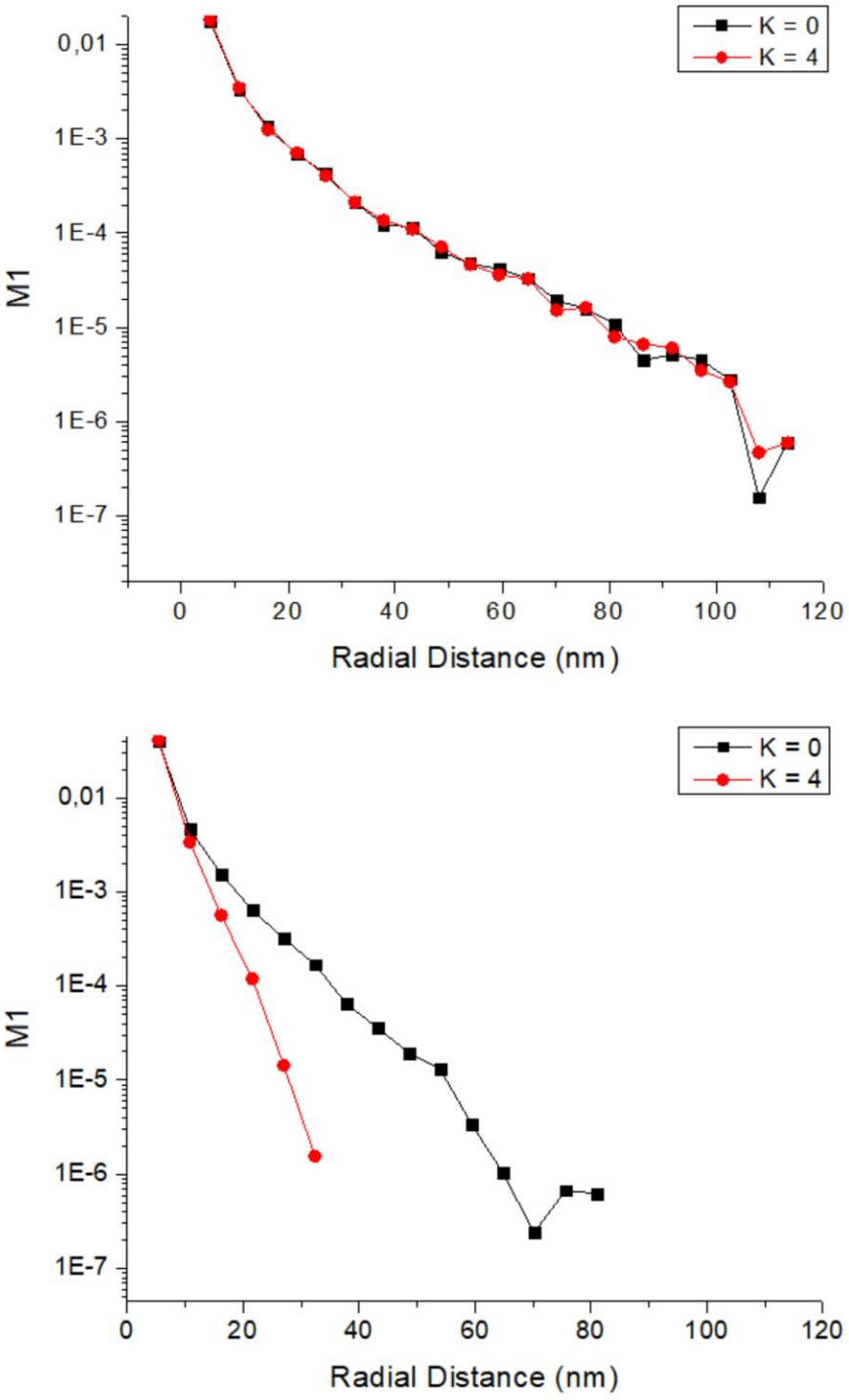

Fig. 96: Mean cluster size M1 variation with the radial distance for multiple target orientations for k = 0 and k = 4. The first graph (Top) presents the results at a pathlength of 500 nm and the second graph is for a pathlength of 19000 nm.

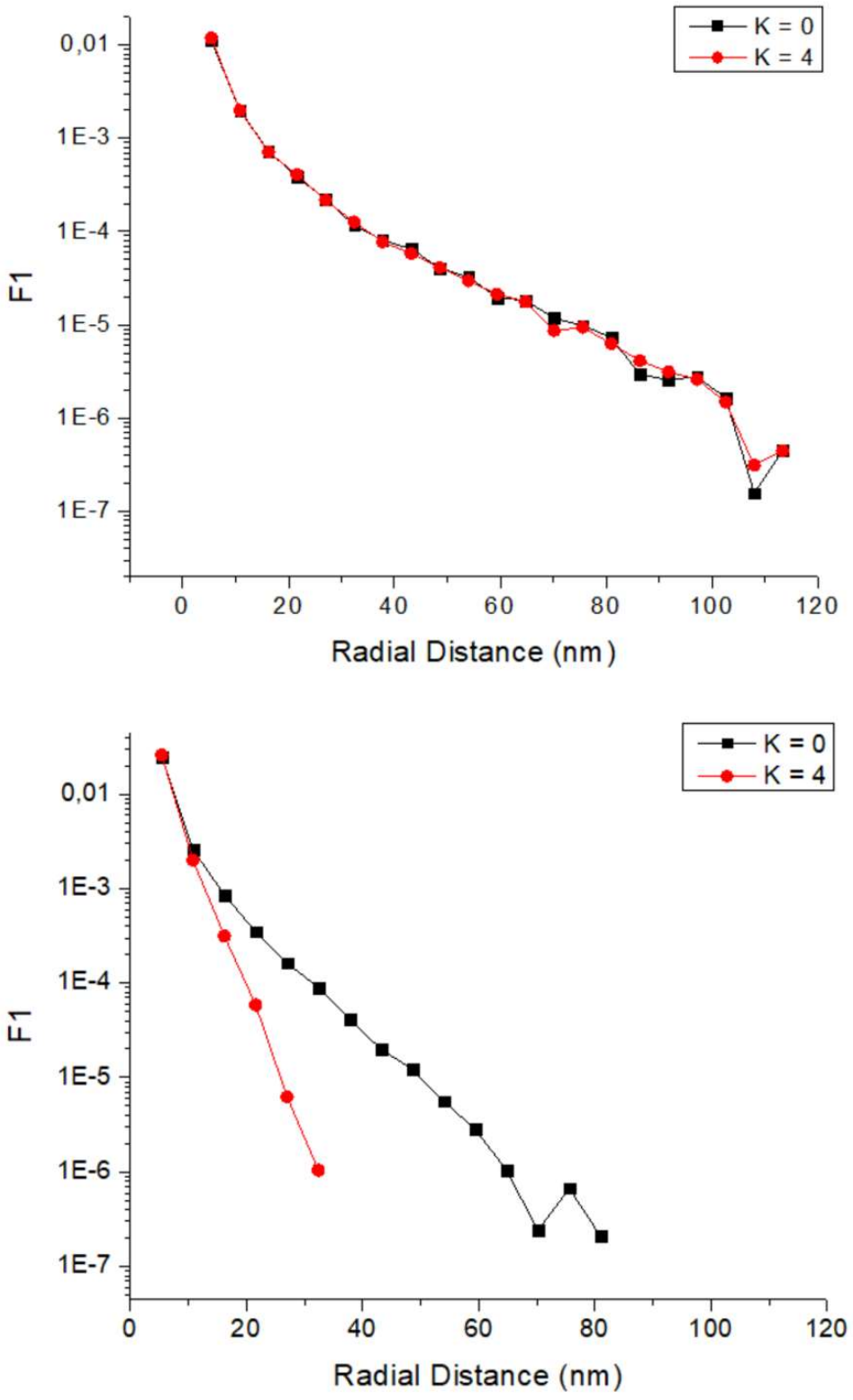

Fig. 98: F1 variation with the radial distace for multiple target orientations for k = 0 and k = 4. The first graph presents the results at a pathlength of 500 nm and the second graph is for a pathlength of 19000 nm.

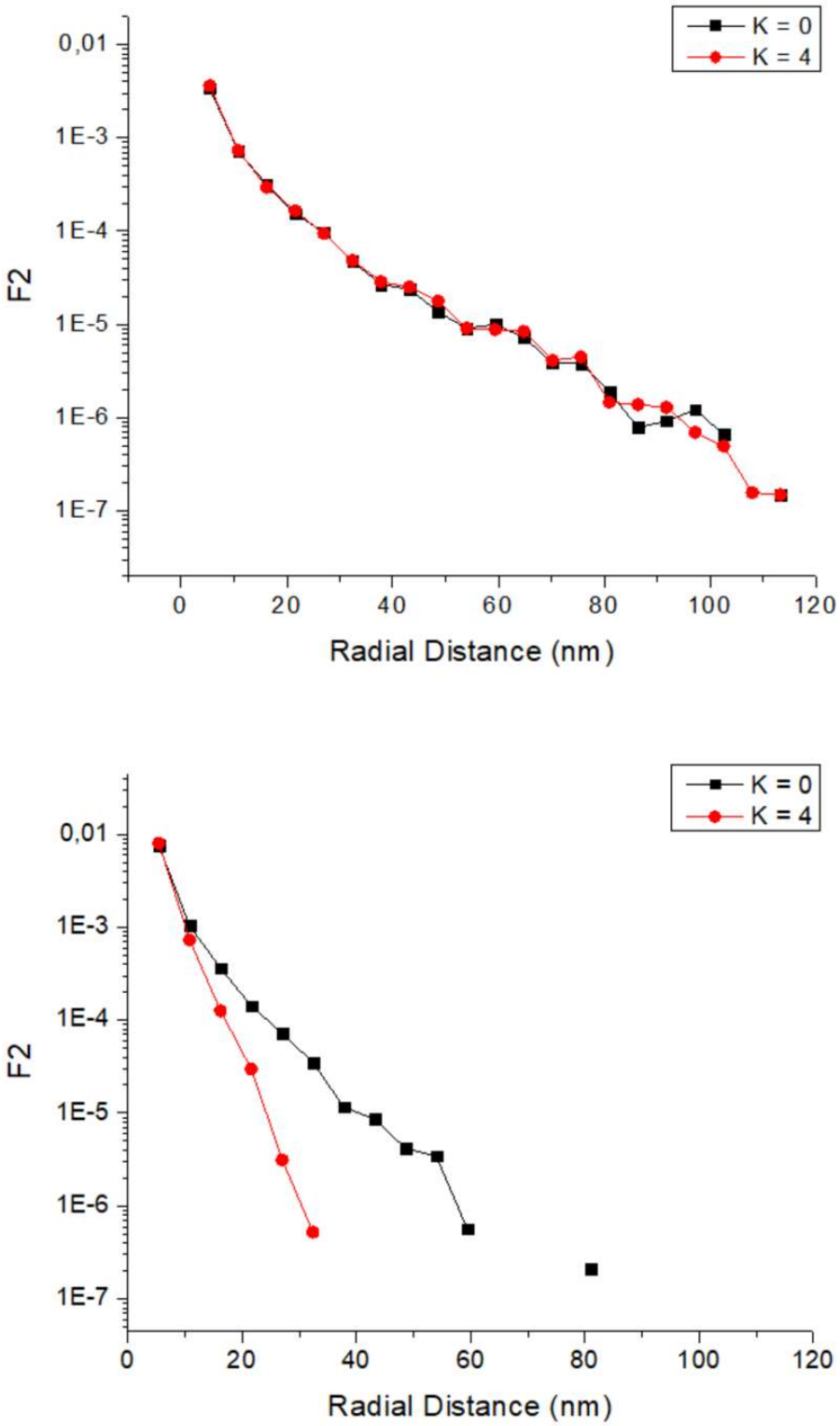

Fig. 100: F2 variation with the radial distance for multiple target orientations for k = 0, 1, 2…,7. The first graph presents the results at a pathlength of 200 nm and the second graph is for a pathlength of 19000 nm.

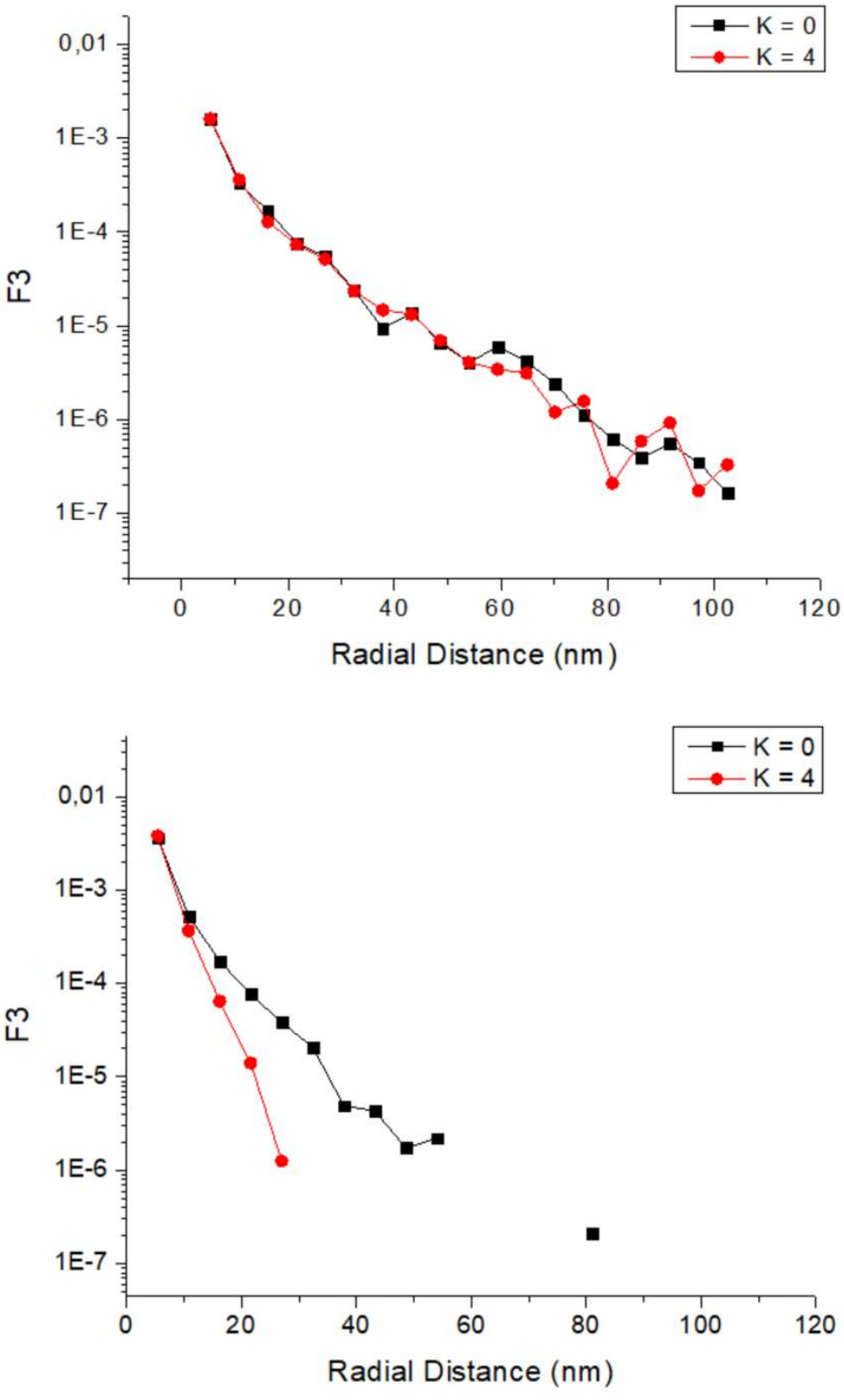

Fig. 102: F3 M1 variation with the radial distance for multiple target orientations for k = 0 and k = 4. The first graph presents the results at a pathlength of 500 nm and the second graph is for a pathlength of 19000 nm.

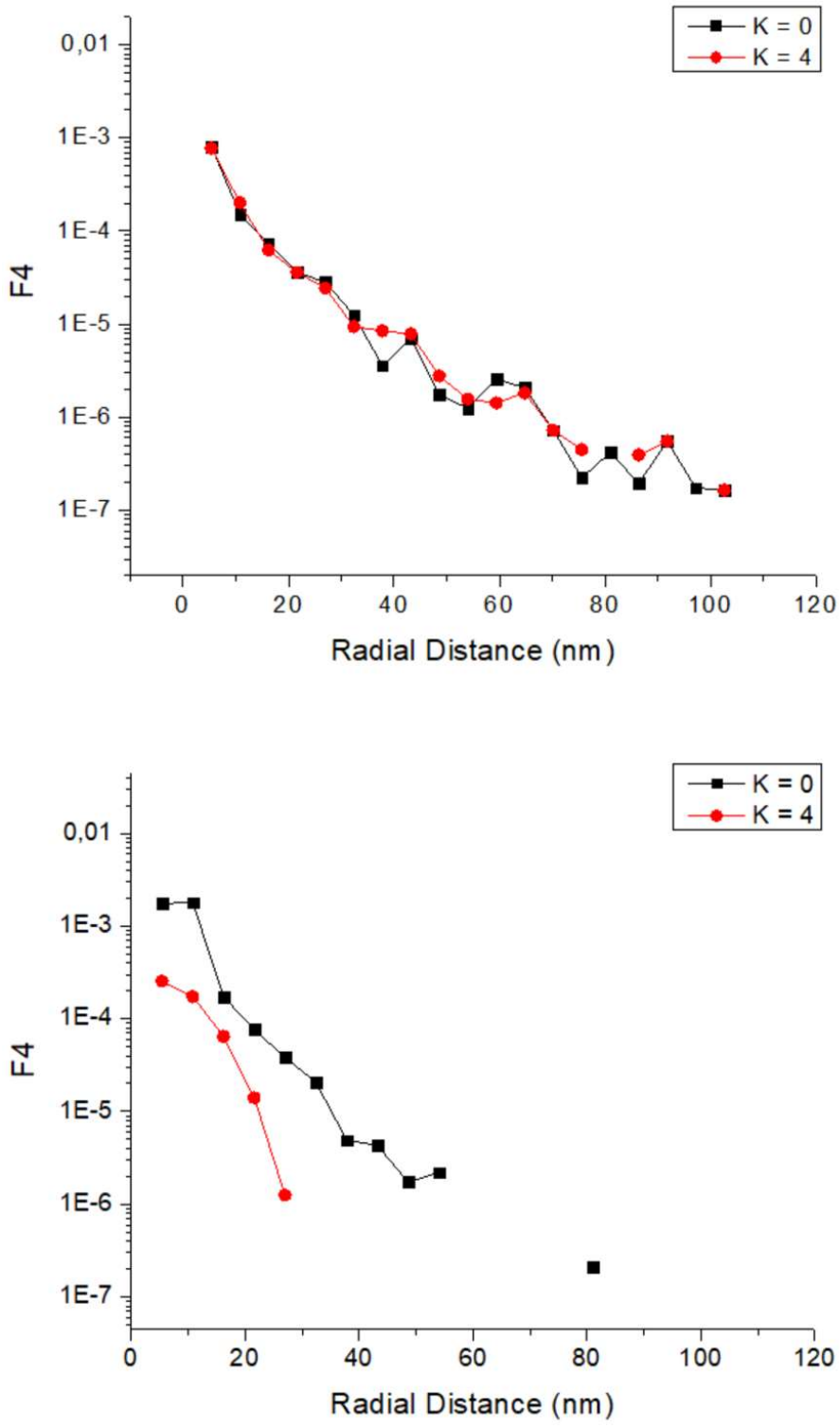

Fig. 104: F4 variation with the radial distance for multiple target orientations for k = 0 and k = 4. The first graph presents the results at a pathlength of 200 nm and the second graph is for a pathlength of 19000 nm.

4.5 Considerations On The Target Size In A Wall-Less Nanodosimeter

Fig. 106 shows a comparison of the efficiency maps obtained by simulation with SIMION (left) and by applying the model (right). For the model calculation, v_d was determined from Eq. (64) using the value of z_t obtained by Eq. (51) using the efficiency map calculated with SIMION. Similarly, D was determined from Eq. (64) using the value of r_t obtained by Eq. (52) when using the SIMION efficiency

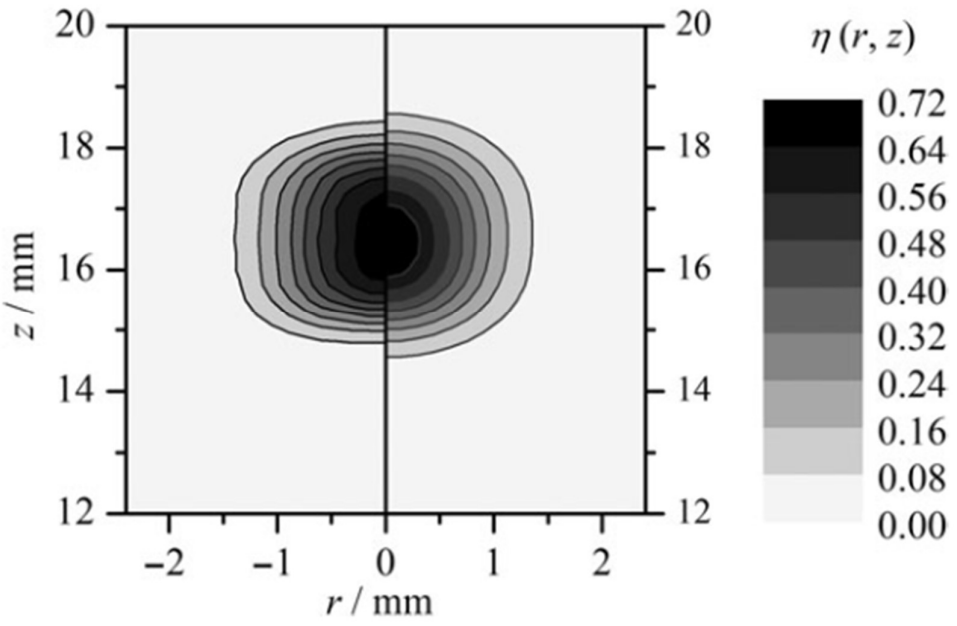

Fig. 106: Comparison of the efficiency maps for a detection time window from 30.5 µs to 35.5 µs and the nanodosimeter operated with 120 Pa of propane as obtained by simulation with SIMION (shown in the left part of the fig- ure) and of the efficiency map obtained with eq. (61) (Rabus *et al.*, 2019).

map. Furthermore, to obtain the same value of η_t from Eqs. (54), the model results had to be multiplied by a factor of 2.5.

CHAPTER 5: GENERAL DISCUSSION

The study that evaluates the variation of nanodosimetric parameters along the pathlength employing the heuristic approach depicts the results that indicate an enhanced probability for inducing ionisation clusters at the distal edge of the SOBP. The increased probability of clusters is due to the low energy of primary protons at the end of their path. This enhancement increases with the complexity of the ionisation cluster (from F_1 to F_4) and thus may provide nanodosimetric evidence for an increased proton RBE at the distal edge of proton SOBPs.

These findings are in qualitative agreement with the results from the review of numerous experimental biological data by (Lühr, von Neubeck, Krause, *et al.*, 2018) (see section 2.6.4, 'Relative biological effectiveness of protons'), the data reported in this work (Fig. 66, Fig. 68) also gives proof of increasing biological effectiveness with depth (along the proton's path) in the absorbing material, where the largest values are toward the distal end of the SOBP.

The current results provide qualitative proof or a possible enhancement in RBE at the distal edge. A quantitative comparison with radiobiological studies could, in principle, be performed using an extrapolation of the range straggling based on the power laws exhibited in Fig. 62. However, such a comparison is beyond the scope of this work, as the results presented here are considered preliminary. The quantitative comparison can more appropriately be made using the detailed analysis presented in the second approach (see section 3.2), the analysis of the radial dependence of the biological effectiveness of proton beams using nanodosimetry. The current results are considered preliminary because the radial cut (maximum cylinder shell radius) used in scoring was chosen based on an assessment of the radial fall-off in the simulated tracks for 1 MeV protons. This may not be an adequate cut-off for the evaluation of high energy protons used in clinical beams, as in the second approach. The consequence of using the small radial cut-off of 100 nm is a significant reduction in the number of ionisations (clusters) observed beyond the chosen maximum radial distance. While the secondary electron spectrum for higher proton energies is also dominated by electrons at energies

below 100 eV, see Fig. 71, with ranges of a few tens of nanometers, the spectrum also extends to higher energies that are associated with larger ranges of the emitted electrons. Hence, limiting the radial integral to an upper limit of 100 nm may lead to an underestimation of the true values of both the AISEI and the nanodosimetric track cross-sections and the nanodosimetric track cross-sections.

Table 16 Normalized ratio of the ETCSs for minimum ICS from 1 to 4 as a function of the proton energy E_p. The data have been obtained by numerical integration of the radial dependence of ionization cluster frequencies obtained from simulation data produced in the BioQuaRT project (Frauke Alexander *et al.*, 2015) using an alternative scoring scheme where the radial range is not limited.

E_p / MeV	F_1^*/z_i^*	F_2^*/z_i^*	F_3^*/z_i^*	F_4^*/z_i^*
3	0.936	1.094	1.164	1.219
10	0.957	1.033	1.040	1.073
25	0.985	1.013	1.012	1.007
50	0.999	1.003	0.975	0.985
100	1.000	1.000	1.000	1.000

An indication that such an underestimation occurs is the significantly smaller exponent in the power-law determined for the AISEI, which was significantly smaller than that expected for the power law of the proton range as a function of its energy. Presented in the detailed approach (see section 3.2, 'Detailed Analysis of the Radial Dependence') is an alternative way of implementing the scoring schemes that take into account larger radial distances (beyond 100 nm) and optimise the scoring methods to improve cluster statistics at the far penumbra. One new analysis method has been applied to simulation results produced within the BioQuaRT project (Frauke Alexander *et al.*, 2015), where a small number (between 25 and 500) of proton tracks with start energies of 3 MeV, 10 MeV, 25 MeV, 50 MeV and 100 MeV were followed over a 10 µm path length.

The preliminary results are summarised in Table 5 Ratio of the results obtained for cylindrical targets and cylinder shell segments both with the same volume) for the specified proton start energies Ep and the first four cumulative ICS frequencies using option 1 (see section 3.2.3) for defining the cylinder shell segments. The values are the ratios for the largest radial distance where both scoring approaches were applied. The last row shows the mean over the five energies and the associated sample standard deviation (given in brackets as multiple of the last significant digit).

Ep / MeV	F1	F2	F3	F4
1	1.18	1.18	1.19	1.21
3	1.08	1.08	1.09	1.11
10	1.11	1.12	1.11	1.12
30	1.12	1.14	1.13	1.14
100	1.15	1.18	1.19	1.25
mean	1.12(4)	1.14(4)	1.14(5)	1.17(6)

Table 6, which shows the ratios of the ETCSs and the AISEI (normalised to their values at 100 MeV). For proton energies of 3 MeV and 10 MeV, which correspond to positions on the proximal shoulder of the BP (see Fig. 62), a significant enhancement of the ETCSs for minimum cluster sizes 2 through 4 can be seen. Therefore, one would expect the core finding of a significantly enhanced probability for complex ionisation clusters at the distal end of the SOBP to remain valid even under the current radial limitation.

The work on the detailed radial analysis (see section 3.2) present results (see section 4.3), giving a comprehensive view of the radial dependence of nanodosimetric parameters around the proton track with energies from 100 MeV to less than 1 MeV. As was mentioned before, the quantitative analysis and comparison of the enhanced probability of nanodosimetric parameters, which imply an enhancement in the RBE, is not covered anywhere in the current work but reserved for future studies. In summary, Fig. 73 shows that the radial cut-off at 100 nm used in earlier work (Rabus *et al.*, 2020) will lead to an underestimation of the radial integrals of the nanodosimetric cumulative frequencies for higher energies of the proton. This may have an impact on the dependence of these integrals (termed effective track cross-sections in (Rabus *et al.*, 2020)) on proton energy and residual range.

In both parts of Fig. 73 all four cumulative probabilities show similar radial dependence. For radial distances below 30 nm, the relative radial dependence is also similar between the two proton energies. The same was also observed for data obtained with other simulated proton energies (not shown). These observations are a qualitative confirmation of previously reported experimental findings (Conte *et al.*, 2012; Hilgers, Bug and Rabus, 2017).

Furthermore, it should be noted that the data shown in Fig. 73(a) show a finite frequency of ionisation clusters at distances larger than 200 times the target radius (about 200 nm). The maximum energy of secondary electrons produced by 1 MeV protons is about 2 keV. Therefore, extrapolating the range data given in the NIST ESTAR database (Berger *et al.*, 2005), one would expect a maximum range of about 200 nm for the secondary electrons.

The ESTAR database, however, only contains data for electron energies above 10 keV as shell corrections are not considered in the calculations from which the database was derived. It is important, however, to consider such shell corrections at lower electron energies as the velocity of the incident electron becomes comparable to the velocities of electrons in atomic orbitals, especially those of the inner shells. In the Monte Carlo simulation, the electron interaction cross-sections of the different shells were taken into account. In addition, the data shown in

Fig. 73(a) at radial distances greater than 200 nm corresponds to one target in the respective radial bin that receives four or more ionisations and about 10-20 targets receiving one or more ionisations if 50,000 proton track segments of 400 nm in length are used for scoring. The total number of targets receiving one or more ionisations was in the order of 4×10^8.

For primary trajectories traversing the target cylinder as well as those passing close by the cylinder, maxima can be seen in the radial dependence that occurs for all primary particle energies at the same radial distance. For targets traversed by the proton trajectory, the occurrence of this maximum is due to an interplay of two factors counteracting each other: On the one hand, the number of target positions along the perimeter increases with increasing radial distance. On the other hand, the chord length of the primary particle inside the cylinder decreases, while the contribution of ionisations by secondary electrons should stay more or less the same. As long as this latter condition holds, the position of this maximum in terms of r/r_0 should also stay the same for other target sizes and media, and probably also projectile types. However, if the ionisation density produced by the projectile or the target size becomes so large that F_1 approaches its saturation value of unity, of course, this peak will be shifted towards $r/r_0 = 1$.

In contrast, the occurrence of the maximum in the near penumbra is not expected a priori. It may be due to the fact that many of the emitted electrons have comparatively low energies and deposit their energy in interactions close to the primary particle trajectory. So, the maximum would occur as a consequence of the interplay between the decreasing fluence of electrons with increasing radial distance from the proton trajectory and their limited range. In this case, it would be expected that this maximum should stay at the same radial distance from the track and hence shift to smaller or larger values of r/r_0 if bigger or smaller values would be used for r_0. For different media, it would move inward or outward depending on the medium's electron interaction cross-sections.

In any case, the fact that the same maximum location in the penumbra was observed for all investigated target shapes makes it unlikely that its occurrence is an artefact

of the scoring method. It is probably a consequence of the basic concept of nanodosimetry, namely that interactions are scored within defined target volumes.

Qualitatively, similar behaviour of the radial dependence with proton energy as in Fig. 75 is also observed in Fig. 77 for the second cumulative probability for targets receiving at least two ionisations. For protons with energies below 10 MeV, the fraction of targets receiving two or more ionisations at distances larger than 30 times the target radius (for this target size) increases with increasing proton energy, whereas the variation with particle energy above 10 MeV is less important: about a quarter of the targets receiving two or more ionisations are placed at distances larger than 30 times the target radius, independent of proton energy. However, two distinct differences can be seen in Fig. 77: First, that for protons with energies below 10 MeV and trajectories intersecting the target volume or passing with impact parameters up to ten times the target radius, the relative frequency of targets with two or more ionisations decreases with increasing energy. Second, that the shoulder at the far side of the maximum around $r \approx 2.5\ r_0$ is more pronounced at low proton energies and there appears to be a second peak in the near penumbra in the logarithmic interval centred at about 10 times the target cylinder radius (Fig. 77(b)). This observation suggests that there may be a higher fraction of targets that receive two or more ionisations following an ionisation event at these distances, which may also imply an enhanced probability for DNA lesions. However, it is understood that the volumetric density of these targets is comparatively low.

The results shown in Fig. 79 demonstrate that for targets intersected by the proton trajectory, the location of the peak is not only invariant with proton energy but also appears to be independent of the complexity of the ionisation clusters scored in the targets (as long as F_2 is far from saturation).

However, the increased variation of the peak's magnitude with proton energy observed in Fig. 77 for F_2 (compared to F_1 in Fig. 75) is further enhanced for F_3 and F_4. In addition, for 30 MeV protons, the overall fraction of targets intersected by the proton trajectory and producing a certain ionisation cluster size decreases from F_1 to F_4, i.e. with increasing ionisation cluster size complexity.

For 1 MeV protons, however, the fraction of targets receiving at least two, three or four ionisations and being intersected by the primary particle trajectory are almost the same. Furthermore, this fraction is greater than that of targets receiving one or more ionisations. This is presumably related to the fact that when the primary particle trajectory traverses the target, ionisations are produced from the primary particle or secondary electron interactions.

The peak at about 2.5 r_0 that is clearly visible in the data for F_1 and for F_2 at 1 MeV overlaps with a second peak in the near penumbra around 10 r_0 for the other cases. For the F_3 and F_4 data, the two peaks are difficult to distinguish at both proton energies considered. But it seems evident that the second peak, which emerges at 30 MeV proton energy in the F_2 data, becomes clearly dominant for the F_4 data at 30 MeV. This suggests that targets with larger ionisation cluster sizes seem to occur at larger impact parameters around 10 r_0 preferentially. To what extent these observations can be generalised for other target sizes is to be addressed in future studies.

Finally, for the outer penumbra region and 1 MeV protons, a similar radial dependence is found for all parameters F_1 to F_4. For 30 MeV, the radial distributions exhibit a plateau region only for F_1 and F_2, whereas for F_3 and F_4 the radial distribution seems to drop steadily in this region.

For fitting data-driven models onto the radial dependence of the frequency of nanodosimetric targets for 30 MeV protons, models Eqs. (67), (69) or (70), are derived and provide the best fit (see Fig. 81 and Fig. 83) for F_1 and also for F_2, and F_3 when applied with some minor conditions that include both the Landau and Gaussian functions (see section 4.3.5). To achieve the best fit of data in for both F_2 and F_3 in Fig. 83 (c) and (d), a Gaussian correction (see dashed-line on graphs). For F_3, this extra contribution seems to be slightly more pronounced than in the case of F_2. This indicates that if the cumulative ICS frequencies are related to the induction of lesions in DNA (Grosswendt, 2004, 2005; Garty *et al.*, 2006, 2010; Bantsar *et al.*, 2018), then there may be a significant contribution of such lesions that are induced by primary particles passing the target volume at impact parameters in the order of about 10 nm.

The fraction of such lesions would be in the same order of magnitude as those originating from the peak at around 3 nm that can be seen in Fig. 81 and Fig. 83. Both peaks are superimposed on a background of targets receiving at least two or three ionisations that may be located as far as 1000 nm from the proton trajectory. This applies to the 30 MeV protons considered in Fig. 81 and Fig. 83, which are representative also for higher proton energies, as can be qualitatively seen in Fig. 75 and Fig. 77. For smaller proton energies, the relevant radial range becomes smaller but still extends to ranges of the order 100 nm.

An important observation can be seen in Fig. 85 that for energies of 10 MeV and higher, the cumulative radial probabilities as a function of radial distance have almost an identical shape and essentially reach unity at r / r_0 of about 1000, i.e. radial distances about 1 µm. Truncation of the radial integrals at 100 nm (i.e. r / r_0 of about 85), as in section 3.1, implies underestimation of the full radial integral (the effective track cross-section) by about 12% to 18%, depending on which of the nanodosimetric parameters F_k is considered. Therefore, enhancement of the probability in creating large clusters at the end of the track, thus increasing the radiobiological effectiveness at the distal end of the SOBP, is still valid but reduced.

For the two energies below 10 MeV shown in Fig. 85, a distinctly different radial dependence can be seen with a more rapid convergence to unity. For the 1 MeV data, this saturation occurs below $r / r_0 = 100$. As mentioned above, for these energies that occur closer to the BP (within about 1 mm), the major fraction of impacted targets is located at radial distances where they are not traversed by the primary particle.

The cumulative radial distributions in Fig. 85 show only minor variation with primary particle energy at proton energies beyond 10 MeV. This suggests that they may not be useful as descriptors of radiation quality. Furthermore, there seems to be an almost constant vertical offset for the 1 MeV and 3 MeV curves compared to the curves for higher proton energies for a range of radial distances starting with the target radius. This could suggest that the features of track structure scored by targets intersected by the primary particle trajectory could be better suited as the specifier of radiation quality – a conjecture that has often been put forth or implicitly

used in nanodosimetry research (Grosswendt, 2004; Nettelbeck and Rabus, 2011; Schulte, 2011; Conte *et al.*, 2018; Selva, Conte and Colautti, 2018).

However, the curves in Fig. 79 and Fig. 85 show data that have been normalised to the respective full radial integral. The full radial integrals vary by several orders of over the energy range covered by Fig. 85. (See, e. g. Fig. 64 in 4.2.2 and 4.2.3 in conjunction with Fig. 64). This resulted in enhancements of the nanodosimetric parameters F_2, F_3 and F_4 at the distal end of a proton SOBP that were in the range between 1 and 2 and ascending in magnitude with the minimum cluster size (see section 4.2.3). This implies that there are small differences in the energy dependence of the full radial integrals of the parameters F_2, F_3 and F_4, which relate to the radiation quality.

Nevertheless, there are also clear differences between the curves for the same proton energy in the different panels of Fig. 85, i.e. for different F_k. This was already evident in Fig. 79, where changes with minimum cluster size could be seen in the track core and the near penumbra regions. This indicates that the signature of radiation quality lies in the differences between the radial distributions of the different parameters F_k as well as in their different energy dependence.

The preliminary results derived from simulation and the heuristic data analysis formalism presented in Fig. 95 to Fig. 103 showed that the orientation of the target cylinder relative to the primary track influences the calculated ICS only slightly. A minimal dependence of cluster size formation on the cylinder orientation is depicted in these figures (specifically at pathlengths before the BP region. At pathlengths near the BP, the $k = 0$ orientation deviates strongly from the $k = 4$ target orientation. A more detailed analysis to explore this dependence has to be done in future studies for the quantitative determination and its incorporation on the models determined in this work for the radial dependence of cluster size probability distribution.

For the investigation of the wall-less target volume in the ion counter, the results are shown in Fig. 106; the two efficiency maps are in good qualitative agreement. The model calculation gives a slightly larger spread in the vertical direction than the simulation with SIMION. This is most likely due to the simplifying assumption

that diffusion and drift in the electric field can be simply superimposed, while interference of the two processes is known to give different diffusion constants for motion parallel and perpendicular to the electric field (Schmidt and Roncossek, 1992).

The factor 2.5 needed to achieve the same average efficiency within the equivalent cylindrical target can be attributed to neglecting the influence of the extraction aperture on the electric field lines and on the particle density. There will be a penetration of the higher electric field below the cathode into region B in the vicinity of the extraction aperture where, in addition, the particle density is reduced owing to the gas flow from region B into the high-vacuum region underneath.

The latter effect implies an increase of drift speed and diffusion constant which, however, will be limited to a small region of a size comparable to the aperture diameter. The field penetration, on the other hand, will lead to funnelling of the ion trajectories through the aperture. Thus, the real aperture in the cathode corresponds to a larger virtual aperture located some distance (on the order of a mm) above the cathode, where the field distortion will indeed be negligible. The collection efficiency will be determined by this virtual aperture, and its radius should be used in Eqs. (62) to (64). How to determine this enhanced aperture radius from the given dimensions of the nanodosimeter setup and the applied voltages is still under study.

Further ongoing work investigates how to solve Eq. (59) with the boundary conditions imposed by the presence of the electrodes and to obtain independent estimates of the drift speed $v_{d,}$ and diffusion constant D. Both parameters can be expected to be a unique function of the cross-section for ion-molecule collisions. Hence, from kinetic gas theory, the diffusion constant D and drift velocity v_d can be expected to be related to the nanodosimeter's operating parameters by

$$D \propto \frac{T_g^{\frac{3}{2}}}{p_g} \quad v_d \propto \left(T_g/p_g\right)^{1/2} \tag{76}$$

In conjunction with Eqs. (54), (55) and (64), this equation allows determining the uncertainty component of nanodosimetric measurement coming from the nanodosimeter's operating parameters.

CHAPTER 6: CONCLUSION

The primary subject for this work has been the investigation – using a Geant4-DNA simulation toolkit and novel analysis tools - of nanodosimetric parameters around proton tracks, in particular how they change with both the radial distance from the proton track and along the proton trajectory. Nanodosimetric parameters are related to initial damage to DNA and are thus related to radiobiological effectiveness. Knowledge of the variation of nanodosimetric parameters with radius and pathlength was used to derive models using both published models and data-driven fits. Two approaches were used in this study. The first approach used a simple heuristic approach to map out the radial variation. Calculated radial integrals, dependent on the pathlength were utilised to map out the pristine nanodosimetric BP and ultimately derive the SOBP. The secondary investigation focused on the so-called wall-less cylindrical target in an ion nanodosimeter derived from the ion collection efficiency represented by a time-dependent model.

The primary investigation finding presents an unprecedented study where proton tracks have been characterised in terms of nanodosimetry over their full range. The radial dependence of the probabilities that ionisation clusters of different complexity are formed in a nanometric target has been translated into effective cross-sections of the track with respect to the considered nanodosimetric probabilities. The nanodosimetric equivalence of SOBPs, together with additional information on the position of protons during their slowing down, have been obtained. Results indicate that the probability for inducing ionisation clusters is enhanced at the distal edge of the SOBP, where the enhancement increases with the complexity of the ionisation cluster. Based on the previously reported link between nanodosimetry and cellular endpoints (Conte *et al.*, 2017), this can be seen as unique evidence for a potential enhancement of proton RBE at the distal edge of SOBPs predicted by nanodosimetry.

For reasons explained in the discussion, these results were preliminary and have been consolidated by a repeat of track data analysis with the aforementioned new and accurate scoring approaches, which overcame the limitations of a fixed scoring

geometry to allow full coverage of the radial range. Also, simulations at higher proton energies have been added to obtain better coverage of the full proton range with supporting points. The detailed dependence of ICS distributions as a function of radial distance gives a comprehensive three-dimensional characterisation of the proton tracks. The more advanced analysis of the radial dependence includes advanced models such as those of (Cucinotta, Nikjoo and Goodhead, 1999; Wang and Vassiliev, 2014).

The aforementioned detailed analysis of the radial dependence also includes an assessment of the uncertainty associated with the different scoring schemes for the track core and penumbra. This is important to verify the resulting radial variation and the model fitting done for the entire radial range.

In summary, results of the crude, heuristic approach, such as the enhancement of proton RBE at the distal edge of SOBPs, indicates the potential use of nanodosimetric track characteristics in proton therapy to qualitatively predict the probability for inducting lethal lesions in cells.

The work presented in section 3.2 (Detailed Analysis of the Radial Dependence) and the results in section 4.3 provides a detailed analysis of the radial dependence of the complementary cumulative ICS distributions in proton tracks, where the analysis is based on deterministic sampling from results for the loci of ionisations in proton tracks simulated with Geant4-DNA. The resulting radial variation of the ICS frequencies can also be interpreted as the spatial distribution of nanometric targets that receive an ICS of a given complexity. Together with the methodology presented in section 3.1 (Variation Of Nanodosimetric Parameters In Proton Tracks – Heuristic Approach), which linked proton energies and their positions along a full proton track, these results enable a full three-dimensional characterisation of proton tracks.

The augmented approach used in this part of the work for scoring ionisation clusters in the penumbra has overcome previous limitations imposed by the first method as previously mentioned. Scoring in the penumbra was performed using cylinder shell segments that have the same volume as the target cylinders used for scoring within

the track core. Three different options for defining the cylinder shell segments were studied, where the option that best approximated the aspect ratio of the cylinders also gave the same values as cylinder targets in the overlap region where both target geometries (cylinders and cylinder shell segments) were applied (see section 4.3.6, "Consistency of the two scoring approaches"). Option 1 that was used in the first analysis showed energy-independent deviations of up to a few percent depending on which element of the complementary cumulative ICS distribution was considered.

In the second approach, data of simulations were used in which protons were followed over a path segment of 650 nm, where ionisations by protons or secondary electrons produced inside a radially infinite 650 nm-thick plane-parallel slab were recorded. Comparison with earlier data obtained for a subset of the considered proton energies within the BioQuaRT project, which involved 10 µm-long proton tracks, indicate that there may be an underestimation of the full radial integral (effective track cross-section) in the order of 15% (see Table 14 Ratio of the effective track cross sections obtained with the data from (Frauke Alexander *et al.*, 2015) and with the simulation results of (Rabus *et al.*, 2020) for the specified initial proton energies Ep and for the first four cumulative ICS frequencies using option 1 for defining the cylinder shell segments in the penumbra region (see section 3.2.3). The last row shows the arithmetic mean over the four energy values and the value in brackets is the sample standard deviation.

Ep / MeV	F1	F2	F3	F4
3	1.11	1.10	1.11	1.11
10	1.21	1.18	1.18	1.18
25	1.16	1.13	1.12	1.10
50	1.16	1.12	1.10	1.09

mean	1.16(4)	1.13(3)	1.13(4)	1.12(4)

Table 15) owing to missing interactions from electron tracks started outside the 650 nm-thick slabs. As this underestimation seems to be independent of proton energy, the same relative variation of the effective track cross-sections along a SOBP as found in the first approach (in section 4.2.3 "Range dependence of radial integrals") is expected.

An improved method of presenting the results used in Fig. 75 and Fig. 77 elucidated that the radial dependence cannot be adequately described by a power law such as that used in (Frauke Alexander *et al.*, 2015). Only for radial distances from about 30 nm up to an energy-dependent radial distance where a steeper fall-off occurs does the data seem to follow a r^{-2} dependence. In the near penumbra region below about 30 nm, pronounced peaks occur where about 2/3 of targets with hits (i.e. ionisation clusters) can be found in this inner penumbra region (Fig. 85). It is this inner penumbra region that is generally accessible to experimental nanodosimetry (Conte *et al.*, 2012; Hilgers, Bug and Rabus, 2017).

Detailed modelling of the radial dependence will require further work to study advanced models that include the overlap of the track structure with cells or the overlap between different proton tracks at fluences related to therapeutic dose levels. The future continuation of the present work may also consider spatial correlations of targets receiving ionisation clusters. This could in principle be done with the tools developed in this work by modifying the analysis codes such that the centre positions of targets receiving ICS of a certain complexity are written to a data file, which could then be processed with routines using larger scoring volumes to establish ICS of a certain complexity. The outcome of this future work would provide input for models aimed at implementing nanodosimetric track structure in proton therapy treatment planning, such as the work proposed by (Besserer and Schneider, 2015a; Casiraghi and Schulte, 2015; F. Alexander *et al.*, 2015) and (Besserer and Schneider, 2015b).

Further issues to be investigated could be the uncertainty attributed to the results that originate, for example, in the different cross-sections used in different options of Geant4-DNA or other codes (Lazarakis *et al.*, 2012; Villagrasa *et al.*, 2019). Another aspect could be to investigate the dependence of the results on the target size used.

Further aspects to be covered in future work could include a study of the dependence of the outcome on the chosen target size (similar to that of the BioQuaRT multi-scale approach (Palmans *et al.*, 2015) and the use of a 3D-distribution of probabilities for targets to show ICSs of a certain complexity in statistical models that include cells or cellular structures (e.g. in a similar way as the MKM (Newpower *et al.*, 2019).

CHAPTER 7: REFERENCES

Abbas, Z. and Rehman, S. (2018) 'An Overview of Cancer Treatment Modalities', in *Neoplasm*.

Alexander, Frauke *et al.* (2015) 'Energy dependent track structure parametrisations for protons and carbon ions based on nanometric simulations', *European Physical Journal D*, 69(9), pp. 216-1-216–7.

Alexander, F. *et al.* (2015) 'Local weighting of nanometric track structure properties in macroscopic voxel geometries for particle beam treatment planning', *Physics in Medicine and Biology*, 60(23), pp. 9145–9156.

Allison, J. *et al.* (2006) 'Geant4 developments and applications', *IEEE Transactions on Nuclear Science*, 53(1), pp. 270–278.

Amols, H. I., Wuu, C. S. and Zaider, M. (1990) 'On possible limitations of experimental nanodosimetry', *Radiation Protection Dosimetry*, 31(1–4), pp. 125–128.

Anferov, V. and Das, I. J. (2015) 'Biological Dose Estimation Model for Proton Beam Therapy', *International Journal of Medical Physics, Clinical Engineering and Radiation Oncology*, 04(02), pp. 149–161.

Archambeau, J. O. *et al.* (1974) 'Proton radiation therapy', *Radiology*, 110(2), pp. 445–457.

Attix, F. H. (2008) *Introduction to Radiological Physics and Radiation Dosimetry*. Weinheim: John Wiley & Sons.

Bantsar, A. *et al.* (2018) 'State of the art of instrumentation in experimental nanodosimetry', *Radiation Protection Dosimetry*, 180(1–4), pp. 177–181.

Barrett, A. *et al.* (2009) *Practical radiotherapy planning*. 4th edn, *Radiology*. 4th edn. Italy: CRC Press.

Barton, M. B. *et al.* (2014) 'Estimating the demand for radiotherapy from the

evidence: a review of changes from 2003 to 2012', *Radiotherapy and Oncology*, 112(1), pp. 140–144.

Baskar, R. *et al.* (2012) 'Cancer and radiation therapy: Current advances and future directions', *International Journal of Medical Sciences*, 9(3), p. 193.

Beaton, L. *et al.* (2019) 'How rapid advances in imaging are defining the future of precision radiation oncology', *British Journal of Cancer*, 120(8), pp. 779–790.

Belli, M. *et al.* (1992) 'Direct comparison of biological effectiveness of protons and alpha-particles of the same LET. II. Mutation induction at the HPRT locus in v79 cells', *International Journal of Radiation Biology*, 61(5), pp. 625–629.

Belli, M. *et al.* (1998) 'RBE-LET relationships for cell inactivation and mutation induced by low energy protons in V79 cells: Further results at the LNL facility', *International Journal of Radiation Biology*, 74(4), pp. 501–509.

Berger, M. J. *et al.* (2005) *ESTAR, PSTAR, and ASTAR: Computer programs for calculating stopping-power and range tables for electrons, protons, and helium ions (version 1.2.3)*.

Bernal, M. A. *et al.* (2015) 'Track structure modeling in liquid water: A review of the Geant4-DNA very low energy extension of the Geant4 Monte Carlo simulation toolkit', *Physica Medica*, 31(8), pp. 861–874.

Bernier, J., Hall, E. J. and Giaccia, A. (2004) 'Radiation oncology: A century of achievements', *Nature Reviews Cancer*, 4(9), pp. 737–747.

Besserer, J. and Schneider, U. (2015a) 'A track-event theory of cell survival', *Zeitschrift fuer Medizinische Physik*, 25(2), pp. 168–175.

Besserer, J. and Schneider, U. (2015b) 'Track-event theory of cell survival with second-order repair', *Radiation and Environmental Biophysics*, 54(2), pp. 167–174.

Beyzadeoglu, M., Ozyigit, G. and Ebruli, C. (2010) *Basic radiation oncology*. Springer Science & Business Media.

Bortfeld, T. and Schlegel, W. (1996) 'An analytical approximation of depth-dose distributions for therapeutic proton beams', *Physics in Medicine and Biology*, 41(8), pp. 1331–1339.

Bortot, D. *et al.* (2017) 'A novel TEPC for microdosimetry at nanometric level: Response against different neutron fields', *Radiation Protection Dosimetry*, 180(1–4), pp. 172–176.

Boyle, P. and Levin, B. (2008) 'World Cancer report 2008', *IARC Press, International Agency for Research on Cancer*.

Braunroth, T. *et al.* (2020) 'Three-dimensional nanodosimetric characterisation of proton track structure', *Radiation Physics and Chemistry*, 176, p. 109066.

Brenner, D. J. and Ward, J. F. (1992) 'Constraints on energy deposition and target size of multiply damaged sites associated with DNA double-Strand breaks', *International Journal of Radiation Biology*, 61(6), pp. 737–748.

Breskin, A. *et al.* (1995) 'A single-electron counter for nanodosimetry', *Radiation Protection Dosimetry*, 61(1–3), pp. 199–204.

Britten, R. A. *et al.* (2013) 'Variations in the RBE for cell killing along the depth-dose profile of a modulated proton therapy beam', *Radiation Research*, 179(1), pp. 21–28.

Brun, R. and Rademakers, F. (1997) 'ROOT - An object-oriented data analysis framework', *Nuclear Instruments and Methods in Physics Research A*, 389, pp. 81–86.

Bueno, M. *et al.* (2015) 'Influence of the geometrical detail in the description of DNA and the scoring method of ionization clustering on nanodosimetric parameters of track structure: a Monte Carlo study using Geant4-DNA', *Physics in Medicine & Biology*, 60, pp. 8583–8599.

Bug, M. *et al.* (2014) 'Nanodosimetric characterization of ion beams', *European Physical Journal D*, 68(8), p. 217.

Casiraghi, M. and Schulte, R. W. (2015) 'Nanodosimetry-based plan optimization for particle therapy', *Computational and Mathematical Methods in Medicine*, 7, pp. 1–13.

Chaudhary, P. *et al.* (2014) 'Relative biological effectiveness variation along monoenergetic and modulated Bragg peaks of a 62-MeV therapeutic proton beam: A preclinical assessment', *International Journal of Radiation Oncology Biology Physics*, 90(1), pp. 27–35.

Chetty, I. J. *et al.* (2015) 'Technology for Innovation in Radiation Oncology', *International Journal of Radiation Oncology Biology Physics*, 93(3), pp. 485–492.

Conte, V. *et al.* (2012) 'Track structure of light ions: Experiments and simulations', *New Journal of Physics*, 14(9), p. 093010.

Conte, V. *et al.* (2017) 'Track structure characterization and its link to radiobiology', *Radiation Measurements*, 106, pp. 506–511.

Conte, V. *et al.* (2018) 'Nanodosimetry: Towards a new concept of radiation quality', *Radiation Protection Dosimetry*, 180(1–4), pp. 150–156.

Cox, R. *et al.* (1977) 'Inactivation and mutation of cultured mammalian cells by aluminium characteristic ultrasoft x-rays: II. Dose-responses of chinese hamster and human diploid cells to aluminium x-rays and radiations of different LET', *International Journal of Radiation Biology and Related Studies in Physics, Chemistry and Medicine*, 31(6), pp. 561–576.

Cruz, G. A. S. and Santa Cruz, G. A. (2016) 'Microdosimetry: Principles and applications', *Reports of Practical Oncology and Radiotherapy*, 21(2), pp. 135–139.

Cucinotta, F. A., Nikjoo, H. and Goodhead, D. T. (1999) 'Applications of amorphous track models in radiation biology', *Radiation and Environmental Biophysics*, 38(2), pp. 81–92.

Cunha, M. *et al.* (2017) 'NanOx, a new model to predict cell survival in the context

of particle therapy', *Physics in Medicine and Biology*, 62, pp. 1248–1268.

Dai, T. *et al.* (2020) 'Nanodosimetric quantities and RBE of a clinically relevant carbon-ion beam', *Medical Physics*, 47, pp. 772–780.

Dalrymple, G. V., Lindsay, I. R., Ghidoni, J. J., *et al.* (1966) 'Some effects of 138-Mev protons on primates.', *Radiation research*.

Dalrymple, G. V., Lindsay, I. R., Hall, J. D., *et al.* (1966) 'The relative biological effectiveness of 138-Mev protons as compared to cobalt-60 gamma radiation.', *Radiation research*.

Delaney, Thomas, F. and Kooy, M. H. (2007) *Proton and charged particle radiotherapy*. 1st editio. Edited by F. Delaney, Thomas and H. M. Kooy. LWW.

Delaney, G. P. and Barton, M. B. (2015) 'Evidence-based Estimates of the Demand for Radiotherapy', *Clinical Oncology*.

DeLuca, P. M., Wambersie, A. and Whitmore, G. (2007) 'Prescribing, recording, and reporting proton-beam therapy', *Journal of the ICRU*.

Elsasser, T. and Scholz, M. (2006) 'Improvement of the local effect model (LEM) - Implications of clustered DNA damage', *Radiation Protection Dosimetry*, 122(1–4), pp. 475–477.

Elsässer, T. and Scholz, M. (2007) 'Cluster effects within the local effect model', *Radiation Research*, 167, pp. 319–329.

Faiz M. Khan, J. P. G. (2014) *The Physics of Radiation Therapy*. Fifth Edit.

Fiorino, C. *et al.* (2020) 'Technology-driven research for radiotherapy innovation', *Molecular Oncology*, 14(7), pp. 1500–1513.

Francis, Z. *et al.* (2011) 'Molecular scale track structure simulations in liquid water using the Geant4-DNA Monte-Carlo processes', *Applied Radiation and Isotopes*, 69(1), pp. 220–226.

Friedland, W. *et al.* (1999) ‘Simulation of DNA fragment distributions after irradiation with photons’, *Radiation and Environmental Biophysics*, 38(1), pp. 39–47.

Friedland, W. and Kundrát, P. (2013) ‘Track structure based modelling of chromosome aberrations after photon and alpha-particle irradiation’, *Mutation Research - Genetic Toxicology and Environmental Mutagenesis*, 756(1–2), pp. 213–223.

Friedrich, T. *et al.* (2018) ‘DNA damage interactions on both nanometer and micrometer scale determine overall cellular damage’, *Scientific Reports*, 8, p. 16063.

Gargioni, E. and Grosswendt, B. (2007) ‘Influence of ionization cross-section data on the Monte Carlo calculation of nanodosimetric quantities’, *Nuclear Instruments and Methods in Physics Research Section A: Accelerators, Spectrometers, Detectors and Associated Equipment*, 580, pp. 81–84.

Garty, G. *et al.* (2002) ‘The performance of a novel ion-counting nanodosimeter’, 492, pp. 212–235.

Garty, G. (2004) *Development of ion-counting nanodosimetry and evaluation of its relevance to radiation biology*. The Weizmann Institute of Science.

Garty, G. *et al.* (2006) ‘First attempts at prediction of DNA strand-break yields using nanodosimetric data’, *Radiation Protection Dosimetry*, 122(1–4), pp. 451–454.

Garty, G. *et al.* (2010) ‘A nanodosimetric model of radiation-induced clustered DNA damage yields’, *Physics in Medicine and Biology*, 55(3), pp. 761–781.

GEANT4 Collaboration Website (2020).

Giovannini, G. *et al.* (2016) ‘Variable RBE in proton therapy: Comparison of different model predictions and their influence on clinical-like scenarios’, *Radiation Oncology*, 11(1), pp. 1–16.

Girdhani, S., Sachs, R. and Hlatky, L. (2013) 'Biological effects of proton radiation: What we know and don't know', *Radiation Research*, 179(3), pp. 257–272.

Goitein, M. (2007) *Radiation Oncology: A Physicist's-Eye View*, *Springer Science \& Business Media*.

Goodhead, D. T. *et al.* (1977) 'Inactivation and mutation of cultured mammalian cells by aluminium characteristic ultrasoft x-rays: III. Implications for theory of dual radiation action', *International Journal of Radiation Biology*, 31, pp. 541–559.

Goodhead, D. T. (1988) 'Spatial and temporal distribution of energy', *Health Physics*, 55(2), pp. 231–240.

Goodhead, D. T. (1994) 'Initial events in the cellular effects of ionizing radiations: Clustered damage in DNA', *International Journal of Radiation Biology*, 65(1), pp. 7–17.

Goodhead, D. T. (2006) 'Energy deposition stochastics and track structure: What about the target?', *Radiation Protection Dosimetry*, 122, pp. 3–15.

Goodhead, D. T. and Thacker, J. (1977) 'Inactivation and mutation of cultured mammalian cells by aluminium characteristic ultrasoft x-rays: I. Properties of aluminium x-rays and preliminary experiments with chinese hamster cells', *International Journal of Radiation Biology*, 31, pp. 541–559.

Grosswendt, B. (2002) 'Formation of ionization clusters in nanometric structures of propane-based tissue-equivalent gas or liquid water by electrons and α - particles', pp. 103–112.

Grosswendt, B. *et al.* (2004) 'Experimental equivalent cluster-size distributions in nanometric volumes of liquid water', *Radiation Protection Dosimetry*, 110(1–4), pp. 789–799.

Grosswendt, B. (2004) 'Recent advances of nanodosimetry', *Radiation Protection Dosimetry*, pp. 789–799.

Grosswendt, B. (2005) ‘Nanodosimetry, from radiation physics to radiation biology.’, 115(1), pp. 1–9.

Grosswendt, B. (2013) ‘Introduction To Nanodosimetry’, in *Preceeding of the EURADOS winter school: Status and Future Perspectives of Computational Micro- and Nanodosimetry*. Barcelona: EURADOS.

Grün, R. *et al.* (2017) ‘Systematics of relative biological effectiveness measurements for proton radiation along the spread out Bragg peak: Experimental validation of the local effect model’, *Physics in Medicine and Biology*, 62(3), pp. 890–908.

Heimbach, F. *et al.* (2017) ‘Measurement of changes in impedance of DNA nanowires due to radiation induced structural damage: A novel approach for a DNA-based radiosensitive device’, *European Physical Journal D*, 71, p. 211.

Hilgers, G. (2010) ‘Check of the scaling procedure of track structures of ionizing radiation in nanometric volumes’, *Radiation Measurements*, 45(10), pp. 1228–1232.

Hilgers, G. *et al.* (2015) ‘Secondary ionisations in a wall-less ion-counting nanodosimeter: quantitative analysis and the effect on the comparison of measured and simulated track structure parameters in nanometric volumes’, *The European Physical Journal D*, 69(10), p. 239.

Hilgers, G., Bug, M. U. and Rabus, H. (2017) ‘Measurement of track structure parameters of low and medium energy helium and carbon ions in nanometric volumes’, *Physics in Medicine and Biology*, 62, pp. 7569–7597.

Hilgers, G. and Rabus, H. (2020) ‘Correlated ionisations in two spatially separated nanometric volumes in the track structure of 241Am alpha particles: Measurements with the PTB ion counter’, *Radiation Physics and Chemistry*, p. 109025.

Hoffmann, T., Bennett, S. and Del Mar, C. (2013) *Evidence-based practice across the health professions*. 2nd edn. Sydney: Elsevier Australia.

Howard, M. E. *et al.* (2017) 'Investigating Dependencies of Relative Biological Effectiveness for Proton Therapy in Cancer Cells', *International Journal of Particle Therapy*, 4(3), pp. 12–22.

Ilicic, K., Combs, S. E. and Schmid, T. E. (2018) 'New insights in the relative radiobiological effectiveness of proton irradiation', *Radiation Oncology*, 13(1), pp. 4–11.

Incerti, S., Ivanchenko, A., *et al.* (2010) 'Comparison of GEANT4 very low energy cross section models with experimental data in water', *Medical Physics*, 37(9), pp. 4692–4708.

Incerti, S., Baldacchino, G., *et al.* (2010) 'THE Geant4-DNA project', *International Journal of Modeling, Simulation, and Scientific Computing*, 1(2), pp. 157–178.

Incerti, S. *et al.* (2018) 'Geant4-DNA example applications for track structure simulations in liquid water: A report from the Geant4-DNA Project', *Medical Physics*, 45(8), pp. e722–e739.

International Atomic Energy Agency (2007) 'Technical Reports Series No. 457 Dosimetry in diagnostic radiology: an internacional code of practice', *IAEA*.

Itoh, A. *et al.* (2013) 'Cross sections for ionization of uracil by MeV-energy-proton impact', *Physical Review A - Atomic, Molecular, and Optical Physics*, 88, p. 052711.

Jacob, S. *et al.* (2005) 'The Role of Radiotherapy in Cancer Treatment Estimating Optimal Utilization from a Review of Evidence-Based Clinical Guidelines', (August), pp. 1129–1137.

Jäkel, O. *et al.* (2001) 'Treatment planning for heavy ion radiotherapy: Clinical implementation and application', *Physics in Medicine and Biology*, 46(4), pp. 1101–1116.

Jenner, T. J. *et al.* (1992) 'Direct comparison of biological effectiveness of protons and alpha-particles of the same LET. III. Initial yield of DNA double-Strand breaks

in v79 cells', *International Journal of Radiation Biology*, 61(5), pp. 631–637.

Jette, David; Chen, W. (2011) 'Creating a spread-out Bragg peak in proton beams', *Physics in Medicine and Biology*, 56, p. N131.

Joiner, M. C. and Kogel, A. J. van der (2018) *Basic Clinical Radiobiology*. Edited by A. van der K. Michael C. Joiner. CRC Press.

Jones, B. (2016) 'Why RBE must be a variable and not a constant in proton therapy', *British Journal of Radiology*, 89(1063), pp. 1–10.

Jones, B. (2017) 'Clinical radiobiology of proton therapy: modeling of RBE', *Acta Oncologica*, 56(11), pp. 1374–1378.

Kase, K. R., Bjarngard, B. E. and Attix, F. H. (1985) *The dosimetry of Ionizing Radiation*. Volume I. Elsevier.

Koehler, A. M. and Preston, W. M. (1972) 'Protons in Radiation Therapy', *Radiology*, 104(1), pp. 191–195.

Krämer, M. and Scholz, M. (2000) 'Treatment planning for heavy-ion radiotherapy: calculation and optimization of biologically effective dose', *Physics in Medicine and Biology*, 45(11), pp. 3319–3330.

Kythe, P. K. and Schäferkotter, M. R. (2004) *Handbook of computational methods for integration*, *Handbook of Computational Methods for Integration*. Taylor & Francis.

Lazarakis, P. *et al.* (2012) 'Comparison of nanodosimetric parameters of track structure calculated by the Monte Carlo codes Geant4-DNA and PTra', *Physics in Medicine and Biology*, 57(5), p. 1231.

Lee, T. F. *et al.* (2014) 'Technical advancement of radiation therapy', *BioMed Research International*.

Leloup, C. *et al.* (2005) 'Evaluation of lesion clustering in irradiated plasmid DNA', *International Journal of Radiation Biology*.

Lindborg, L. and Waker, A. (2017) *Microdosimetry: experimental methods and applications*. CRC Press.

Loeffler, J. S. and Durante, M. (2013) 'Charged particle therapy-optimization, challenges and future directions', *Nature Reviews Clinical Oncology*.

Lühr, A., von Neubeck, C., Pawelke, J., *et al.* (2018) '"Radiobiology of Proton Therapy": Results of an international expert workshop', *Radiotherapy and Oncology*, 128(1), pp. 56–67.

Lühr, A., von Neubeck, C., Krause, M., *et al.* (2018) 'Relative biological effectiveness in proton beam therapy – Current knowledge and future challenges', *Clinical and Translational Radiation Oncology*.

Ma, C.-M. C. and Lomax, To. (2013) *Proton and Carbon Ion Therapy*. Taylor & Francis Group.

Marshall, T. I. *et al.* (2016) 'Investigating the Implications of a Variable RBE on Proton Dose Fractionation Across a Clinical Pencil Beam Scanned Spread-Out Bragg Peak', *International Journal of Radiation Oncology Biology Physics*, 95(1), pp. 70–77.

MathWorks (2019) *MATLAB*, *MATLAB*.

Matsumoto, Y. *et al.* (2014) 'Enhanced radiobiological effects at the distal end of a clinical proton beam: In vitro study', *Journal of Radiation Research*, 55(4), pp. 816–822.

Matsuzaki, Y. *et al.* (2010) 'Nuclear collision processes around the Bragg peak in proton therapy', *Radiological Physics and Technology*, 3(1).

Mohan, G. *et al.* (2019) 'Recent advances in radiotherapy and its associated side effects in cancer—a review', *The Journal of Basic and Applied Zoology*, 80(1), pp. 1–10.

Muhammed, M. (2017) *An Introduction to Medical Physics*, *Spinger International*

Publishing. Edited by M. Maqbool. Cham: Springer International Publishing (Biological and Medical Physics, Biomedical Engineering).

Munro, T. R. (1970) 'The relative radiosensitivity of the nucleus and cytoplasm of Chinese hamster fibroblasts.', *Radiation research*, 42(3), p. 451.

Nahum, A. E. and Uzan, J. (2012) '(Radio)biological optimization of external-beam radiotherapy', *Computational and Mathematical Methods in Medicine*, pp. 1–13.

De Nardo, L. *et al.* (2002) 'Ionization-cluster distributions of α-particles in nanometric volumes of propane: Measurement and calculation', *Radiation and Environmental Biophysics*, 41, p. 235.

Nettelbeck, H. and Rabus, H. (2011) 'Nanodosimetry: The missing link between radiobiology and radiation physics?', in *Radiation Measurements*. Elsevier Ltd, pp. 893–897.

Newhauser, W. D. and Zhang, R. (2015) 'The physics of proton therapy', *Physics in Medicine and Biology*, 60(8), pp. R155–R209.

Newpower, M. *et al.* (2019) 'Using the Proton Energy Spectrum and Microdosimetry to Model Proton Relative Biological Effectiveness', *International Journal of Radiation Oncology Biology Physics*, 104(2), pp. 316–324.

Nikjoo, H. *et al.* (1999) 'Quantitative modelling of DNA damage using Monte Carlo track structure method', *Radiation and Environmental Biophysics*, 38(1), pp. 31–38.

Nikjoo, H. *et al.* (2006) 'Track-structure codes in radiation research', 41, pp. 1052–1074.

Nikjoo, H. and Goodhead, D. T. (1991) 'Track structure analysis illustrating the prominent role of low-energy electrons in radiobiological effects of low-LET radiations', *Physics in Medicine and Biology*, 36(2), p. 229.

Nikjoo, H., Uehara, S. and Emfietzoglou, D. (2012) *Interaction of radiation with*

matter. CRC press.

Paganetti, H. *et al.* (2002) 'Relative biological effectiveness (RBE) values for proton beam therapy', *International Journal of Radiation Oncology Biology Physics*, 53(2), pp. 407–421.

Paganetti, H. (2012) *Proton Therapy Physics*. Taylor & Francis Group.

Paganetti, H. (2014) 'Relative biological effectiveness (RBE) values for proton beam therapy. Variations as a function of biological endpoint, dose, and linear energy transfer', *Physics in Medicine and Biology*, 59(22), pp. R419–R472.

Paganetti, H. *et al.* (2019) 'Report of the AAPM TG-256 on the relative biological effectiveness of proton beams in radiation therapy', *Medical Physics*, 46(3), pp. e53–e78.

Palmans, H. *et al.* (2015) 'Future development of biologically relevant dosimetry', *British Journal of Radiology*, 88(1045), p. 20140392.

Pan, H. Y. *et al.* (2016) 'Supply and Demand for Radiation Oncology in the United States: Updated Projections for 2015 to 2025', *International Journal of Radiation Oncology*Biology*Physics*.

Paretzke, H. G. *et al.* (1991) 'Spatial distributions of inelastic events produced by electrons in gaseous and liquid water', *Radiation Research*.

Particle Therapy Co-Operative Group (2019).

Pietrzak, M., Pszona, S. and Bantsar, A. (2018) 'Measurements of spatial correlations of ionisation clusters in the track of carbon ions-first results', *Radiation Protection Dosimetry*, 180(5), pp. 162–167.

Podgorsak, E. A. (2005) 'Radiation oncology physics', *Vienna: International Atomic Energy Agency*, pp. 123–271.

Podgorsak, E. B. (2016) *Radiation Physics for Medical Physicists*. Cham: Springer International Publishing (Graduate Texts in Physics).

Pszona, S. (1975) ‘A track ion counter’, in *In: EUR 5452 d-e-f, Proceedings Fifth Symposium on Microdosimetry. Luxemburg: Commission of the European Communities*, pp. 1107–1122.

Pszona, S., Kula, J. and Marjanska, S. (2000) ‘A new method for measuring ion clusters produced by charged particles in nanometre track sections of DNA size’, 447, pp. 601–607.

PTCOG (2019) *Particle Therapy Centers*, *Particle Therapy Co-Operative Group (PTCOG)*.

Rabus, H. *et al.* (2014) ‘Biologically weighted quantities in radiotherapy: An EMRP joint research project’, *EPJ Web of Conferences*, 77, p. 00021.

Rabus, H. *et al.* (2019) ‘Considerations on the target size in a wall-less nanodosimeter’, *Radiation protection dosimetry*, 183(6), pp. 182–186.

Rabus, H. *et al.* (2020) ‘“Broadscale” nanodosimetry: Nanodosimetric track structure quantities increase at distal edge of spread-out proton Bragg peaks’, *Radiation Physics and Chemistry*, 166, p. 108515.

Rabus, H. (2020) ‘Nanodosimetry – on the “‘tracks’” of biological radiation effectiveness’, *Zeitschrift fur Medizinische Physik*, 30(2), pp. 91–94.

Rabus, H. and Nettelbeck, H. (2011) ‘Nanodosimetry : Bridging the gap to radiation biophysics’, *Radiation Measurements*, 46(12), pp. 1522–1528.

Raju, M. (1974) ‘Pions and heavy ions in radiotherapy. Presented at the Xlth international cancer congress, Florence; 20–26 Oct 1974. Excerpta medica international congress series, vol 353’, *Surgery, radiotherapy and chemotherapy of cancer*, 5, pp. 161–167.

Ramos-Méndez, J. *et al.* (2018) ‘Fast calculation of nanodosimetric quantities in treatment planning of proton and ion therapy’, *Physics in Medicine & Biology*, 63, p. 235015.

Rath, A. K. and Sahoo, N. (2016) *Particle radiotherapy: Emerging technology for treatment of cancer*, *Particle Radiotherapy: Emerging Technology for Treatment of Cancer*.

Relative Biological Effectiveness in Ion Beam Therapy (2008). Vienna: INTERNATIONAL ATOMIC ENERGY AGENCY (Technical Reports Series).

Robertson, J. B. *et al.* (1975) 'Radiobiological studies of a high-energy modulated proton beam utilizing cultured mammalian cells', *Cancer*, 35, pp. 1664–1677.

Rodrigues, P. *et al.* (2004) 'Geant4 applications and developments for medical physics experiments', *IEEE Transactions on Nuclear Science*, 51(4), pp. 1412–1419.

Rossi, H. H. (1959) 'Specification of radiation quality.', *Radiation research*, 10(5), pp. 522–531.

Rossi, H. H. (1960) 'Spatial Distribution of Energy Deposition by Ionizing Radiation', *Radiation research Supplement*, 2, pp. 290–299.

Rossi, H. H., Biavati, M. H. and Gross, W. (1961) 'Local energy density in irradiated tissues. 1. Radiobiological significance.', *Radiation Research*, 15(4), pp. 431–439.

Rossi, H. H. H. and Zaider, M. (1996) *Microdosimetry and Its Applications*, *Microdosimetry and Its Applications*. Berlin: Springer.

Rossi, H. H. and Rosenzweig, W. (1955) 'A device for the measurement of dose as a function of specific ionization.', *Radiology*, 64(3), pp. 404–411.

Salminen, E., Izewska, J. and Andreo, P. (2005) 'IAEA's role in the global management of cancer-focus on upgrading radiotherapy services', *Acta Oncologica*, 44(8), pp. 816–824.

Santin, G. *et al.* (2003) 'New Geant4 based simulation tools for space radiation shielding and effects analysis', *Nuclear Physics B - Proceedings Supplements*.

Sato, T. *et al.* (2011) 'Applications of the microdosimetric function implemented in the macroscopic particle transport simulation code PHITS', *International Journal of Radiation Biology*, 88(1–2), pp. 143–150.

Scharf, W. H. and Wieszczycka, W. (2001) *Proton Radiotherapy Accelerators*. Singapore: World Scientific Publishing Co. Pte. Ltd.

Schmidt, B. and Roncossek, M. (1992) 'Drift Velocity, Longitudinal and Transverse Diffusion in Hydrocarbons derived from Distributions of Single Electrons', *Australian Journal of Physics*, 45(3), p. 351.

Scholz, M. and Kraft, G. (1994) 'Calculation of heavy ion inactivation probabilities based on track structure, X ray sensitivity and target size', *Radiation Protection Dosimetry*, 52(1–4), pp. 29–33.

Scholz, M. and Kraft, G. (1996) 'Track structure and the calculation of biological effects of heavy charged particles', *Advances in Space Research*.

Schuemann, J. *et al.* (2019) 'TOPAS-nBio: An Extension to the TOPAS Simulation Toolkit for Cellular and Sub-cellular Radiobiology', *Radiation Research*, 191(2), pp. 125–138.

Schulte, R. *et al.* (2006) 'Mapping the Sensitive Volume of an Ion-Counting Nanodosimeter', *Journal of Instrumentation*, 1, pp. 1–13.

Schulte, R. (2011) 'Nanodosimetry: principle and current status', *In AIP Conference Proceedings*, 1345(1), pp. 249–261.

Schulte, R. W. *et al.* (2005) 'Density resolution of proton computed tomography', *Medical Physics*, 32(4), pp. 1035–1046.

Schulte, R. W. *et al.* (2008) 'Nanodosimetry-based quality factors for radiation protection in space', *Zeitschrift für Medizinische Physik*, 18, pp. 286–296.

Seltzer, S. M. *et al.* (2011) 'Fundamental quantities and units for ionizing radiation', *Journal of the ICRU*, 11(1), pp. 1–41.

Selva, A., Conte, V. and Colautti, P. (2018) 'A Monte Carlo tool for multi-target nanodosimetry', *Radiation Protection Dosimetry*, 180, pp. 182–186.

Sibtain, A., Morgan, A. and MacDougall, N. (2012) *Physics for clinical oncology*. OUP Oxford.

SIMION (2018) *http://www.simion.com/*.

Słonina, D. *et al.* (2014) 'Relative biological effectiveness of the 60-MeV therapeutic proton beam at the Institute of Nuclear Physics (IFJ PAN) in Kraków, Poland', *Radiation and Environmental Biophysics*.

Smith, B. D. *et al.* (2010) 'The future of radiation oncology in the United States from 2010 to 2020: Will supply keep pace with demand?', *Journal of Clinical Oncology*.

Sørensen, B. S., Overgaard, J. and Bassler, N. (2011) 'In vitro RBE-LET dependence for multiple particle types', *Acta Oncologica*, 56(11), pp. 1387–1391.

Tabakov, S., Franco, M. and Sprawls, P. (2012) 'Encyclopaedia of Medical Physics', in *CRC Press*.

Thomas, D. J. (2012) 'ICRU report 85: fundamental quantities and units for ionizing radiation', *Radiation Protection Dosimetry*, 150(4), pp. 550–552.

Tobias, J. S. (1996) 'The role of radiotherapy in the management of cancer - An overview', *Annals of the Academy of Medicine Singapore*.

Tommasino, F. and Durante, M. (2015) 'Proton radiobiology', *Cancers*, 7(1), pp. 353–381.

Tung, C. J. (2015) 'Microdosimetric relative biological effectiveness of therapeutic proton beams', *Biomedical Journal*, 38(5), pp. 399–407.

Uehara, S. and Nikjoo, H. (2006) 'Monte Carlo simulation of water radiolysis for low-energy charged particles', *Journal of Radiation Research*, 47(1), pp. 69–81.

Villagrasa, C. *et al.* (2019) 'Assessing the contribution of cross-sections to the uncertainty of Monte Carlo calculations in micro- and nanodosimetry', *Radiation Protection Dosimetry*, 183(12), pp. 11–16.

Villegas, F. *et al.* (2016) 'Energy deposition clustering as a functional radiation quality descriptor for modeling relative biological effectiveness', *Medical Physics*, 43, pp. 6322–6335.

Wang, H. and Vassiliev, O. N. (2014) 'Radial dose distributions from protons of therapeutic energies calculated with Geant4-DNA', *Physics in Medicine and Biology*, 59(14), pp. 3657–3668.

Willers, H. *et al.* (2018) 'Toward A variable RBE for proton beam therapy', *Radiotherapy and Oncology*, 128(1), pp. 68–75.

Wilson, R. R. (1946) 'Radiological use of fast protons.', *Radiology*, 47(5), pp. 487–491.

Wroe, A. J. (2007) *Developments in Microdosimetry and Nanodosimetry for Space and Therapeutic Applications*. PhD thesis, University of Wollongong.

CHAPTER 8: APPENDIX

8.1 **Plagiarism Form: Turnitin Report**

0200932r:SonwabileFinal.docx

ORIGINALITY REPORT

2%	2%	3%	0%
SIMILARITY INDEX	INTERNET SOURCES	PUBLICATIONS	STUDENT PAPERS

PRIMARY SOURCES

1	Particle Radiotherapy, 2016. Publication	1%
2	phyusdb.files.wordpress.com Internet Source	1%
3	link.springer.com Internet Source	1%

Exclude quotes	On	Exclude matches	< 1%
Exclude bibliography	On		

Nukri Komin
School of Physics
PG coordinator

8.2 **Ethics Clearance Form**

The current research did not involve any animal experimentation, use of human subjects, or involve any genetically modified organisms or substances. Therefore, ethic clearance was not necessary.

8.3 Supplementary Technical Information

8.3.1 Pre-processing of simulation data

Analysis of the simulation results was performed by post-processing the simulation output files using ad-hoc developed scripts under ROOT (Brun & Rademakers, 1997) and programs are written in FORTRAN-77 (Lamprecht, 1986). The explicit mention of these programming environments is just to give a comprehensive account of the tools used. It is not meant as an endorsement or an implicit statement that they are best suited for the purpose of these investigations.

In order to facilitate a more efficient further analysis, the simulation results were written by ROOT scripts to data files in ASCII format. These ASCII data files were processed using a self-written FORTRAN program which calculated for each ionisation point the radial and azimuth coordinates in a cylindrical coordinate system with the proton trajectory as the *z*-axis. After sorting the data ascending first in primary particle number and then in position along the proton trajectory, the data were written to an output file. These pre-processed track data files were then used for the detailed track analysis (see sections 3.2.3 and 8.3.2)

A modification of the pre-processing code was used to first calculate the coordinates of the interaction points of secondary electrons relative to the interaction position of the primary particle that produced the first-generation secondary electron. The resulting tracks consisting of the interactions of the first-generation secondary electron and its daughter electrons were then pre-processed in the same way as described in the previous paragraph.

8.3.2 Implementation of the track data analysis

Three FORTRAN codes named AnalTC, AnalTP, and AnalCP were written to sample the relative frequencies of targets receiving a certain ionisation cluster size, according to their radial distance from the primary particle trajectory.

In programs AnalTC and AnalCP, targets were placed at different radial distances from and positions along the proton trajectory, such that the target centre positions

in a cylindrical coordinate system with the proton trajectory as the z-axis were given by

$$z_i = s + (i - (n_z + 1)/2)\Delta z \qquad i = 1, \ldots, n_z \qquad (77)$$

$$r_j = (j - 1)\Delta r \qquad j = 1, \ldots, n_r \qquad (78)$$

$$\varphi_k = (k - 1)\, 2\pi/n_{\varphi,j} \qquad k = 1, \ldots, n_{\varphi,j} \qquad (79)$$

In Eqs. (77) to (79), s is the centre of the region of interest (ROI) between two planes perpendicular to the proton trajectory used for scoring the ionisations in the tracks. Δz is the user-defined step width along the z-axis. The upper index n_z is the largest integer for which $(n_z - 1)\Delta z$ is smaller or equal to the ROI thickness, Δs (cf. Eq. 31). Δr is the increment in the radial distance and n_r and $n_{\varphi,j}$ are the maximum numbers of radial and azimuthal positions. As indicated, the choice of $n_{\varphi,j}$ may depend on the radial distance from the proton trajectory.

The probability $P_\nu(r_j, s)$ that a proton track produces an ionisation cluster size ν in a target located at a radial distance r_j from the proton trajectory in the ROI (centred at $z = s$) was estimated by

$$P_\nu(r_j, s) = \frac{1}{n_t n_z n_{\varphi,j}} \sum_{l=1}^{n_t} \sum_{i=1}^{n_z} \sum_{k=1}^{n_{\varphi,j}} \Theta_\nu(i, j, k, l) \qquad (80)$$

where $\Theta_\nu(i, j, k, l)$ is 1 if in the l-th simulated proton track an ionisation cluster of size ν is formed in the target located at position (z_i, r_j, φ_k) and 0 otherwise. The triple sum in Eq.(80) is the total number of considered targets at radial distance r_j where a cluster of size ν is found for the n_t tracks analysed.

In program **AnalTC**, that was used for analysing the track core region of the simulated proton tracks (as illustrated in Fig. 44), the targets were cylinders of adjustable diameter d_c and height h_c. The number of radial positions was hardcoded to $n_r = 100$. The increment in radial position Δr was calculated from the respective input parameters according to:

$$\Delta r = \left(d_c{}^2 h_c/2\right)^{1/3} \tag{81}$$

Such that at least 10 off-axis radial positions are obtained where the primary particle trajectory intersects the target cylinders. For a cylinder diameter of 2.3 nm and height 3.4 nm, the resulting increment Δr is about 0.1 nm. The increment in z-direction was used as an input parameter. In the analysis presented in this study, a value of $\Delta z = 0.904$ nm was used, such that (for the chosen region of interest thickness of 400 nm) $n_z = 441$. Furthermore, a fixed value of $n_{\varphi,j} = 16$ was used for the number of azimuthal positions.

In program **AnalTP**, the targets were segments of cylinder shells that covered the region of interest without overlap between different target volumes located in the same plane perpendicular to the primary particle trajectory, as indicated in Fig. 46. The planes defining the bottom and top of the cylinder were perpendicular to the proton trajectory which coincided with the cylinder symmetry axis. The innermost target was cylindrical with a radius equal to half the radial target centre increment Δr, and the increment of the further concentric cylinder radii was equal to Δr. The height of the cylinder shells was equal to the increment in the z-direction, Δz, which was chosen such that the volume of the targets was equal to the volume of a cylinder of diameter 2.3 nm and height 3.4 nm.

Different the work presented in section 3.1.2, the program allowed one to set both the parameter Δr and the number of azimuths independent on the radius. Furthermore, the scoring was not performed in fixed targets. Instead, the cylindrical coordinates (z,r,φ) of the ionisation points were converted to the respective integers specifying the target position in the following way:

$$i = \left[\frac{z - s}{\Delta z}\right]; \quad j = \left[\frac{r - s}{\Delta r}\right]; \quad k = 1 + \left[\frac{\varphi \times n_{\varphi,j}}{2\pi}\right] \tag{82}$$

As the pre-processed data were sorted ascending in z position, the data for targets with the same value of i were appearing consecutively in the data files. For each value of i, the integers j and k belonging to the different ionisation points in the respective plane-parallel slab were sorted ascending first in j and then in k. The

occurrence of each combination of integers j and k was then scored to obtain the corresponding cluster size. Proceeding this way allowed efficient scoring and ensured that all ionisations in the slab were considered.

In practice, for larger radial distances there was an increasing number of radial shells where no ionisations were found. Consequently, prior to writing output files, the track analysis results for $j \geq 12$ were resampled in such a way that the average over several radial shells was obtained, where the number of averaged shells was approximately increasing exponentially.

The purpose of program **AnalCP** was to obtain reference data for assessing the equivalence between the different scoring target geometries. This program was a hybrid of the other two: the targets were cylinders of adjustable diameter and height whose radial and azimuth centre positions were the same as for the cylinder shell-segment targets used in program AnalTP. The number of radial distances was limited to $n_r = 24$. The increment in the z-direction was chosen as half the thickness of the slabs used in program AnalTP. The resulting overlapping of the targets in the z-direction was intended to assure that most of the ionisations in the ROI were scored.

The track simulations were analysed with both programs, AnalTP and AnalCP, using a cylinder diameter of 2.3 nm and height 3.4 nm in AnalCP and three different choices of target positions in both programs. In option 1, the parameters defining the target positions were the same as those used in (Rabus *et al.*, 2020), i.e. $\Delta r = 2.80$ nm, $\Delta s = 2.30$ nm, and $n_{\varphi,j} = 8\ (j\text{-}1)$ for $j > 1$ and $n_{\varphi,j} = 1$ for $j = 1$. The same values of $n_{\varphi,j}$ were also used in option 2 with the values $\Delta r = 3.16$ nm and $\Delta s = 1.80$ nm. In this option, the value of Δs was chosen, such as to correspond to the mean chord length of the primary particle track through the cylinder rather than to the cylinder diameter as in option 1.

For option 3, $n_{\varphi,j} = 4\ (j\text{-}1)$ was used for $j > 1$ and $\Delta r = \Delta s = 2.08$ nm. The rationale behind this was to have an 'aspect ratio' of the target 'height' (along the azimuth) to the 'diameter' (the radial size) as well as the shape of the 'cross section' (for fixed azimuth) similar to that of cylindrical targets. Despite the target for $j = 1$ in

the AnalTP program having only half the volume of the target cylinders in the AnalTC and AnalCP programs, this is not expected to cause a problem as only the AnalTP results in the penumbra region are needed.

In all three programs, the mean ionisation cluster size M_1 was scored along with the frequencies for cluster sizes up to 9 and the cumulative frequency of cluster sizes 10 and higher. From these data, the complementary cumulative frequencies F_k for a minimum number of k ionisations in a target between 1 and 10 were calculated and saved to the respective output files.

8.3.3 **Calculation of the radial integrals**

If y_k denotes any of the nanodosimetric quantities F_k (k = 1, 2, …), the respective radial total integral $y_k^{\#}$ is given by:

$$y_k^{\#}(s) = 2\pi \int_0^{\infty} y_k(r,s)\, r\, dr \tag{83}$$

As the results for the core and the outer penumbra regions were obtained separately as outputs of the programs AnalTC and AnalTP, respectively, it is possible to split the integrals in Eq. (83) into two parts:

$$y_k^{(\mathrm{c})}(s) = 2\pi \int_0^{r_n} y_k(r,s)\, r\, dr \tag{84}$$

$$y_k^{(\mathrm{p})}(s) = 2\pi \int_{r^n}^{\infty} y_k(r,s)\, r\, dr \tag{85}$$

For the numerical integration, it is beneficial to consider the function $w_k(r) = 2\pi r y_k(r)$ and to choose the radial support points such that Newton-Cotes integration methods can be applied, such as the so-called 3/8 rule (Kythe and Schäferkotter, 2004). For the application of the 3/8 rule, the radial steps must be chosen such that there are subsequent triplets of intervals with the same length. That is

$$r_{i+j} = r_i + j \times \Delta r_k \quad \text{for} \quad i = 3(k-1) \tag{86}$$

with $j \in \{1,2,3\}$ and $k \in \{1,2,\dots\}$. The interface point, r_n, must be chosen such that $n = 3K$, i.e. $r_n = r_{3K}$. Then, Eqs. (84) and (85) transform into

$$y_k^{(c)}(r_n, s) = \sum_{i=0}^{n} a_i y_k(r_i, s) \tag{87}$$

$$y_k^{(p)}(r_n, s) = \sum_{i=n}^{\infty} a_i y_k(r_i, s) \tag{88}$$

with the following coefficients:

$$a_i = \begin{cases} 0 & \text{if } i = 0 \\ \frac{\pi}{4} r_i (r_{i+1} - r_{i-1}) & \text{if } i = 3k \text{ and } i \neq n \\ \frac{\pi}{4} r_n (r_n - r_{n-1}) & \text{if } i = n \\ \frac{3\pi}{8} r_i (r_{i+1} - r_{i-1}) & \text{else} \end{cases} \tag{89}$$

Eqs. (87) through (89) have been implemented in program AnalTP to not only calculate integrals on the fly but also to investigate correlations of the two integrals for the purpose of uncertainty estimation. Eqs. (87) and (88) were also used to calculate the cumulative radial distributions of frequencies of targets receiving a given minimum number of ionisations.